

2.13 Oxide Fuel Performance Modeling and Simulation[☆]

Paul Van Uffelen, European Commission, Joint Research Centre, Karlsruhe, Germany

Giovanni Pastore, Idaho National Laboratory, Idaho Falls, ID, United States

© 2020 Elsevier Ltd. All rights reserved.

2.13.1	Introduction	364
2.13.1.1	Importance of Fuel Performance Modeling	364
2.13.1.2	Geometrical Idealization and Size of the Problem	365
2.13.1.3	Uncertainties and Limitations	366
2.13.2	Basic Equations and State-of-the-Art	366
2.13.2.1	Heat Transfer	366
2.13.2.1.1	Axial heat transfer in the coolant	367
2.13.2.1.2	Heat transport through the cladding	367
2.13.2.1.3	Heat transport from the cladding to the fuel pellet	368
2.13.2.1.4	Heat transport in the fuel pellets	369
2.13.2.1.5	The structure of the thermal analysis	370
2.13.2.2	Mechanical Analysis	370
2.13.2.2.1	Main assumptions and equations	371
2.13.2.2.2	Calculation of strains	371
2.13.2.2.2.1	Elastic strain	371
2.13.2.2.2.2	Non-elastic strain	371
2.13.2.2.2.2.1	Thermal strain	371
2.13.2.2.2.2.2	Swelling	372
2.13.2.2.2.2.3	Plasticity and creep	373
2.13.2.2.2.2.4	Pellet cracking	374
2.13.2.2.3	Boundary conditions	376
2.13.2.2.3.1	Radial boundary conditions	376
2.13.2.2.3.2	Axial boundary conditions	376
2.13.2.2.4	Pellet-cladding interaction	376
2.13.2.2.4.1	Pellet-cladding mechanical interaction	376
2.13.2.2.4.2	Irradiation induced stress corrosion cracking	378
2.13.2.2.4.3	Outside-in cracking caused by power ramps	380
2.13.2.3	Fission Gas Behavior	380
2.13.2.3.1	Basic mechanisms	381
2.13.2.3.1.1	Recoil, knockout and sputtering	381
2.13.2.3.1.2	Lattice diffusion of single gas atoms	381
2.13.2.3.1.3	Trapping	382
2.13.2.3.1.4	Intra-granular bubble evolution	382
2.13.2.3.1.5	Grain growth and grain boundary sweeping	383
2.13.2.3.1.6	Grain boundary diffusion	383
2.13.2.3.1.7	Grain-face bubble evolution	383
2.13.2.3.1.8	Grain-edge tunnel formation and thermal fission gas release	384
2.13.2.3.2	Modeling fission gas behavior in engineering fuel analysis	385
2.13.2.3.2.1	Intra-granular behavior	386
2.13.2.3.2.2	Inter-granular behavior	387
2.13.2.3.2.3	Coupling intra- and inter-granular behavior	389
2.13.3	Design Basis Accident Modeling	390
2.13.3.1	Loss of Coolant Accidents	390
2.13.3.1.1	Specific LOCA features	390
2.13.3.1.2	Specific LOCA modeling requirements	391
2.13.3.1.2.1	Phase transition model	391

[☆]*Change History:* March 2019. Paul Van Uffelen and Giovanni Pastore updated the section on heat transfer, with particular focus on temperature distribution across the gap between the fuel pellets and the cladding surface, as well as the pellet cracking in the mechanical analysis. Also, the section on fission gas behavior has been revised and extended. Furthermore, the section dealing with the advanced topics has been updated. In particular, the development and application of uncertainty and sensitivity analysis, the inclusion of high burnup features in fuel performance codes, as well as the developments of multi-scale analysis tools has been revised.

This is an update of Van Uffelen, P., Suzuki, M., 2012. Chapter 3.19 – Oxide Fuel Performance Modeling and Simulations. In: Konings, R.J.M. (Ed.), *Comprehensive Nuclear Materials*, Elsevier, pp. 535–577.

2.13.3.1.2.2	High temperature oxidation	392
2.13.3.1.2.3	High temperature deformation model	393
2.13.3.1.2.4	Rupture criteria for ballooning cladding	394
2.13.3.1.2.5	Axial fuel relocation	394
2.13.3.1.2.6	Modeling benchmark for LOCA	395
2.13.3.1.2.7	Multi-rod behavior prediction model	395
2.13.3.2	Reactivity Initiated Accidents	395
2.13.3.2.1	Specific RIA features	395
2.13.3.2.2	Specific RIA modeling requirements	396
2.13.3.2.2.1	Thermal and mechanical calculations for fast transients	396
2.13.3.2.2.2	FGR during RIA	396
2.13.3.2.2.3	Cladding failure	396
2.13.3.2.2.4	Modeling benchmark for RIA	398
2.13.4	Advanced Issues and Future Needs	398
2.13.4.1	Deterministic Versus Probabilistic Analyses	398
2.13.4.2	High Burnup	401
2.13.4.3	Mixed Oxide Fuels	404
2.13.4.4	Multi-Scale Modeling	405
2.13.5	Summary and Conclusions	407
References		408

Abbreviations

(C)SED	(critical) strain energy density	LEFM	linear elastic fracture mechanics
2D/3D	two-dimensional/three-dimensional	LHR	linear heating rate
BCC	body centered cubic	LOCA	loss of coolant accident
BOL	beginning of life	LWR	light water reactor
BWR	Boiling Water Reactor	MC	Monte Carlo
CANDU	Canada Deuterium Uranium	MD	molecular dynamics
CSR	volatile fission product release	MIMAS	micronized master blend
CZP	cold zero power	MOX	mixed oxide
DFT	density functional theory	NEA	Nuclear Energy Agency
DNB	departure from nucleate boiling	O/M	oxygen-to-metal ratio
ECCS	emergency core cooling systems	OECD	Organization for Economic Cooperation and Development
ECR	equivalent cladding reacted	PAS	positron annihilation spectroscopy
EOL	end of life	PCI	pellet-cladding interaction
EPMA	electron probe micro-analysis	PCMI	pellet cladding mechanical interaction
FCC	face centered cubic	PWR	Pressurised Water Reactor
FDM	finite difference method	RIA	reactivity initiated accident
FEM	finite element method	S/V	surface-to-volume ratio
FGR	fission gas release	SANS	small angle neutron scattering
HBS	high burnup structure	SCC	stress corrosion cracking
HCP	hexagonal closed packed	SM	shell model
HZP	hot zero power	TAD	temperature accelerated dynamics
IAEA	International Atomic Energy Agency	TEM	transmission electron microscopy
IFA	Instrumented fuel assembly		

2.13.1 Introduction

2.13.1.1 Importance of Fuel Performance Modeling

The current article focuses on the simulation of nuclear fuel in commercial nuclear power plants, i.e., on LWR fuel, and complements the article on fast breeder reactor fuels in this book. In order to ensure the safe and economic operation of nuclear fuel rods, it is necessary to be able to predict their behavior and life-time. The accurate description of the fuel rod's behavior, however, involves various disciplines ranging from chemistry, nuclear and solid state physics, metallurgy, ceramics, and applied mechanics. The strong interrelationship between these disciplines, as well as the non-linearity of many processes involved, call for the

Table 1 List of main fuel rod performance codes developed in different parts of the world for light water reactor fuel

Country	Organization	Code name (precursor codes)
Argentina	CNEA	BACO, ^{2,3} DIONISIO ^{4–6}
Belgium	Belgonucleaire	COMETHE ^{7–9}
	SCK-CEN	MACROS (ASFAD) ¹⁰
China	Xi'an Xiaotong University	FROBA ¹¹
	CIAE	FTPAC ¹²
	NPIC	FUPAC ¹³
	CGNPC	JASMINE ^{14,15}
Czech Republic	UJV	PIN-MICRO (GAPCON-THERMAL2) ^{16,17}
France	CEA	ALCYONE (METEOR-TRANSURANUS), ^{18–20} TOUTATIS ²¹
	Framatome	COPERNIC (TRANSURANUS), ²² GALILEO (COPERNIC/RODEX/CARO) ²³
	EdF	CYRANO ²⁴
	IRSN	SCANAIR ²⁵
Germany	Siemens	CARO ²⁶
	Framatome	GALILEO (COPERNIC/RODEX/CARO) ²³
	GRS	TESPA-ROD (TESPA) ²⁷
	JRC	TRANSURANUS (URANUS) ^{28–31}
Hungary	MTA EK	FUROM (PIN-MICRO) ³²
India	BARC	FAIR, ³³ PROFESS ³⁴
	PNC	FUDA ^{33,35}
Japan	CRIEPI	EIMUS (FEMAXI-III) ³⁶
	JAEA	FEMAXI, ³⁷ RANNS ^{38–40}
	SEPC	IRON (FEMAXI-III) ³⁶
	NFD	TRUST ³⁶
Korea	KAERI	COSMOS, ^{41,42} INFRA ^{43,44}
Russian Federation	VNIINM	START, ^{45–47} RAPTA ⁴⁸
	TRINITI	RTOP ^{49,50}
	IBRAE	SFPR (MFPR) ^{51,52}
Sweden	Westinghouse Sweden Electric	STAV, ⁵³ STAV-T ⁵⁴
United Kingdom	NNL, EDF Energy	ENIGMA (MINIPAT, SLEUTH, HOTROD) ^{55–57}
USA	USNRC, PNNL	FRAPCON, ⁵⁸ FRAPTRAN (FRAP), ⁵⁹ FAST ⁶⁰
	Siemens	RODEX ⁶¹
	EPRI	FALCON (FREY, ESCORE) ^{62–64}
	INL	BISON ⁶⁵
	Framatome	GALILEO (COPERNIC/RODEX/CARO) ²³
	Westinghouse	PAD ⁶⁶

Note: Van Uffelen, P., Hales, J., Li, W., Rossiter, G., Williamson, R., 2019. A review of fuel performance modeling. J. Nucl. Mater. 516, 373.

development of computer codes describing the general fuel behavior. Fuel designers and safety authorities rely heavily on these types of codes since they require minimal costs in comparison with the costs of an experiment or an unexpected fuel rod failure. The codes are being used for R&D purposes, for the design of fuel rods, new products or modified fuel cycles and to support loading of fuel into a power reactor, i.e., to verify compliance with safety criteria in safety case submissions. A list of commonly used fuel performance codes was included in the recent review paper¹ and is included in [Table 1](#).

2.13.1.2 Geometrical Idealization and Size of the Problem

In principle, our spatial problem is three-dimensional (3D). However, the geometry of a cylindrical fuel rod in a commercial nuclear power plant (a very long, very thin rod) suggests that any section of a fuel rod may be considered as part of an infinite body, i.e., neglecting axial variations. By further assuming axial-symmetric conditions because of the cylindrical geometry, the original 3D problem is commonly reduced to a one-dimensional one. Analysing the fuel rod at several axial sections with a (radially) one-dimensional description is sometimes referred to as quasi 2D or 1.5D. Most fuel rod performance codes fall into this category.¹ Real 2D codes such as for instance the FALCON code⁶⁴ offer the possibility to analyse r-z problems (no azimuthal variation) and r- ϕ problems (no variation in axial direction). Examples of codes with 3D analysis capabilities are ALCYONE^{19,20} and BISON⁶⁵. In practice and generally speaking, 2D or 3D codes are used for the analysis of local effects, whereas the other codes have the capability to analyse the whole fuel rod during a complicated, long power history as discussed in the state-of-the-art report of the NEA.⁶⁷

In order to estimate the “size” of the problem at hand, the number of time steps must also be specified. For a normal irradiation under base load operation, i.e., under no load-follow operation, approximately 100–500 time steps are sufficient. However, for an irradiation in a research reactor like the OECD Heavy-water BWR in Halden many more variations of the linear rating with time are recorded. In such a situation, one must either simplify the complicated power history or increase the number

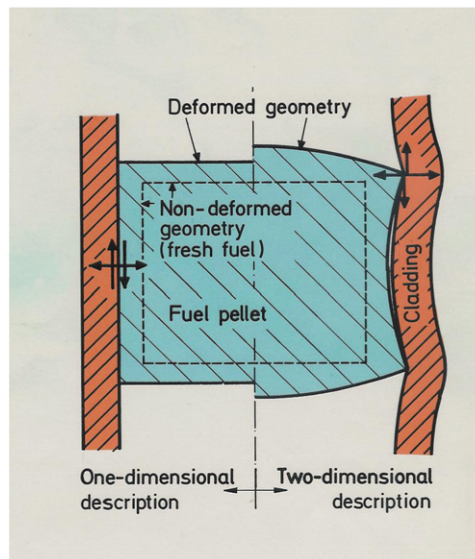


Fig. 1 Schematic view of a deformed fuel pellet; comparison between a one-dimensional and a two-dimensional description.

of time steps to the order of several thousand.⁶⁸ The simplest geometrical idealization needs approximately 20 radial and 20 axial nodes; a 2D representation of a single pellet would approximately need several hundred nodes. Therefore, local models, which are in almost all cases nonlinear, must be very carefully constructed, since even for the simplest geometrical idealization the number of calls may easily reach the order of millions:

$$15 \text{ radial} \times 15 \text{ axial nodes} \times 5000 \text{ time steps} \times 3 \text{ iterations} = 3.4 \times 10^6 \text{ calls.}$$

Even with the computer power of today, a full 3D analysis of, for instance, a complex fuel rod irradiation history in an experimental reactor is very challenging with deterministic models. It should be kept in mind that such an analysis is limited by the fact that the fuel fragments shape and positions are determined by a stochastic process. Nevertheless, 3D analysis tools exist (e.g., ALCYONE,⁶⁹ BISON,⁷⁰ etc.) and are complementary to the conventional fuel performance codes.^{65,67}

2.13.1.3 Uncertainties and Limitations

In general, the uncertainties to be considered may be grouped into four categories. The first category deals with the prescribed or input quantities for the fuel rod performance code: fuel fabrication parameters (rod geometry, composition, etc.), which are often available with an acceptable precision and are subject to specification limits. The second category covers irradiation parameters (reactor type, coolant conditions, irradiation history, etc.). Although they contain a certain level of uncertainty, they can be properly managed in actual analyses. The third category of uncertainties is related to the material properties, such as the fuel thermal conductivity or the fission gas diffusion coefficients. The fourth and last category of uncertainties is the so-called model uncertainties. A good example of such an uncertainty is the plain strain assumption in the axial direction as illustrated in **Fig. 1**, representing the interaction of the deformed and cracked fuel with the cladding. Intuitively, it is clear that for a detailed analysis of such problems 2D or even 3D models are indispensable.

One of the most important consequences of all uncertainties is that one must implement models of “adequate” complexity, i.e., the level of detail of submodels implemented in a fuel performance code has to be consistent with the uncertainties involved in the overall fuel rod analysis approach.

2.13.2 Basic Equations and State-of-the-Art

2.13.2.1 Heat Transfer

The objective of this section is to describe how the temperature distribution in a nuclear fuel rod is calculated in a fuel rod performance code. The scope is limited to a description of the important physical phenomena, along with the basic equations and the main assumptions. Detailed numerical aspects as well as mathematical derivations are provided in some reference works.^{71–73}

The temperature distribution in a fuel rod is of primary importance for several reasons. First of all, the commercial oxide fuels have poor thermal conductivities, resulting in high temperatures even at modest power ratings. Secondly, the codes are used for safety cases where one has to demonstrate the fulfillment of criteria, such as no fuel melting occurring, or the rod internal pressure remaining below a certain limit. Finally, many other properties and mechanisms are strongly dependent on temperature.

The most important quantity is of course the local power density q''' , i.e., the produced energy per unit volume and time. It is usually assumed that q''' depends only on the radius and the time. The linear rating is then simply given by

$$q' = \int_{r_{f,i}}^{r_{cl,o}} q'''(r) 2\pi r dr = \int_{r_{f,i}}^{r_{f,o}} \bar{q}_f'' f(r) 2\pi r dr + \int_{r_{cl,i}}^{r_{cl,o}} \bar{q}_{cl}'' 2\pi r dr \quad (1)$$

where $r_{f,i}/r_{cl,i}$ is the inner fuel/cladding radius, $r_{f,o}/r_{cl,o}$ is the outer fuel/cladding radius, \bar{q}_f'' and \bar{q}_{cl}'' are the average power density in the fuel and cladding, respectively, and $f(r)$ is a radial distribution (form) function (cf. Section 2.13.2.1.4 below). Generally, the linear rating is a prescribed quantity and is a function of the axial coordinate z and the time t . For some phenomena (e.g., cladding creep), the fast neutron flux is also needed. It can be prescribed as well but may also be calculated from the local power density.

2.13.2.1.1 Axial heat transfer in the coolant

In general three regimes must be covered in a LWR:

- (1) The sub-cooled regime, where only surface boiling occurs. This regime is typical for PWR's under normal operating conditions.
- (2) The saturated, two phase regime. This regime is typical for BWR's under normal operating conditions.
- (3) The saturated or overheated regime. This regime may be reached in off-normal situations. A typical example is a LOCA.

The fuel rod performance codes use one-dimensional (axial) fluid dynamic equations that can only cope with the first two regimes. For simulating the third type of regime, the whole reactor coolant system needs to be analysed by means of thermo-hydraulic system codes like RELAP, TRACE or ATHLET in order to provide adequate boundary conditions (coolant pressure and temperature, heat transfer coefficient) to the fuel rod performance code.

The temperature calculation in the coolant serves two purposes. First of all, the axial coolant temperature in the basic (fictional) channel provides the (Dirichlet) boundary condition for the radial temperature distribution in the fuel rod. It results from the combined solution of the mass, momentum and energy balance equations. The simplified equation used in fuel performance codes reads

$$c\rho \frac{\partial T}{\partial t} + c\rho w \frac{\partial T}{\partial z} = q_{cl,c}'' \frac{2\pi r_{cl,o}}{A} + q_c'' \quad (2)$$

where c represents the coolant heat capacity, ρ its density, w its velocity, T its temperature, $q_{cl,c}''$ the heat flux from the cladding to the coolant, A the channel cross-sectional area, $r_{cl,o}$ the cladding outer radius and q_c'' the power density in the coolant. In general, the heat flux from cladding to coolant $q_{cl,c}''$ should be computed by means of a thermo-hydraulic code. Mathematically, the boundary condition is of the convective (Neumann) type:

$$q_{cl,c}'' = -\lambda \left. \frac{\partial T(r,t)}{\partial r} \right|_{r_{cl,o}} = \alpha \{T(r=r_{cl,o}) - T_c\}$$

where α is the heat transfer coefficient between cladding and coolant and $T_c = T_c(z,t)$ is the (bulk) coolant temperature. Only for a steady-state condition the heat flux from the cladding to the coolant is known and is given by

$$c\rho w \frac{dT}{dz} = \frac{q'}{A} + q_c'' \quad (3)$$

Under normal operational conditions, the mass flow rate $\dot{m} = A\rho w$, the coolant inlet temperature and pressure are prescribed. In an off-normal or accidental situation the normal operational condition is the initial condition, but the boundary conditions must be provided by the thermo-hydraulic system codes.

The second objective of the heat flow calculation in the coolant is the derivation of the radial temperature drop between the coolant and the cladding $T_{cl}-T_c$, resulting from convection:

$$q'' = \alpha_{film}(T_{cl} - T_c) = \frac{q_c''}{2\pi r_{cl,o}}$$

The heat transfer coefficient in the film depends on the type of convection (forced or natural) and the type of coolant (gas, liquid, liquid metal). In the sub-cooled regime of a PWR, the Dittus-Boelter correlation is largely applied, whereas in the saturated regime of a BWR the Jens-Lottes correlation is applied.

2.13.2.1.2 Heat transport through the cladding

The heat transport through the cladding occurs through conduction, which is described by the Fourier equation in cylindrical coordinates:

$$\frac{1}{r} \frac{\partial}{\partial r} \left(r \lambda_c \frac{\partial T}{\partial r} \right) + q_{cl}'' = 0$$

where λ_c is the cladding conductivity ($\sim 20 \text{ W m}^{-1} \text{ K}^{-1}$ for Zircaloy), and the heat generation in the cladding is generally neglected (the gamma-heating, as well as the exothermic clad oxidation process are generally disregarded). In order to account for the

presence of an outside oxide layer with a thermal conductivity on the order of $2 \text{ W m}^{-1} \text{ K}^{-1}$ for ZrO_2 (thickness $< 100 \text{ }\mu\text{m}$), the total equivalent cladding conductivity can be obtained by applying the formula for serial thermal resistances. In a similar manner, the appearance of crud on the outer cladding surface is sometimes accounted for through an additional heat transfer coefficient.

2.13.2.1.3 Heat transport from the cladding to the fuel pellet

The temperature difference in the pellet-cladding gap, ΔT_{gap} , is calculated as follows^{74,75}:

$$\Delta T_{\text{gap}} = \frac{q''}{h_{\text{gap}}}$$

where q'' is the heat flux in W per unit area, and h_{gap} is the heat transfer coefficient between fuel and cladding (gap conductance). Heat transfer by convection can be neglected. In general, the heat transfer coefficient h_{gap} depends on

- (1) Gap width or contact pressure between fuel and cladding;
- (2) Gas pressure and composition;
- (3) Surface characteristics of cladding and fuel.

In fact, there are three parallel conduction routes:

$$h_{\text{gap}} = h_{\text{rad}} + h_{\text{con}} + h_{\text{gas}}$$

The contribution of the radiative component is given by

$$h_{\text{rad}} = \left(\frac{C_s}{1/\varepsilon_f + 1/\varepsilon_{cl} - 1} \right) \frac{T_f^4 - T_{cl}^4}{T_f - T_{cl}}$$

where C_s is the Stefan-Boltzmann constant, ε the emissivity and T the temperature. The radiative component is less than 1% during normal operating conditions, because of the moderate temperatures and the limited difference between the two surface temperatures. However, during accident conditions such as loss of coolant accidents, the temperatures in the gap can become higher.

The component h_{con} reproduces the improvement in heat transfer due to pellet-cladding contact pressure, for which typically an empirical correlation is applied instead of elaborate models (e.g., Centikale⁷⁶). Correlations usually depend on the mean value (λ_m) of the thermal conductivities of fuel (λ_f) and cladding (λ_{cl}), the Meyer Hardness (H) of the softer material (cladding) along with the contact pressure (P):

$$h_{\text{con}} = C \frac{\lambda_m}{\sqrt{\delta_{am}}} \left(\frac{P_{\text{con}}}{H} \right)^n$$

where

$$\delta_{am} = \sqrt{(\delta_f^2 + \delta_{cl}^2)}$$

represents the arithmetic mean of the surface roughnesses of fuel (δ_f) and cladding (δ_{cl}) as suggested by Ross and Stoute,⁷⁷ and C is a numerical constant. The exponent n takes a value between 0.5 and 1, as reviewed by Herranz *et al.*⁷⁸ more recently.

It should be mentioned that in some cases a contribution to the gap conductance associated with pellet-cladding contact has been considered regardless of the gap size being positive.^{79,80} This is ascribed to the eccentricity of the pellet fragments after cracking, leading to localized pellet-cladding contact. In order to account for the resulting contact points, there are various approaches that were summarized by White.⁸¹ Some authors define an empirical relation for the fraction of the cladding surface being in contact with pellet fragments (f_{con}), applying this as a weighting factor for the gap conductance:

$$h_{\text{gap}} = (1 - f_{\text{con}})h_{\text{gas}} + f_{\text{con}}h_{\text{con}} + h_{\text{rad}}$$

where f_{con} is typically an empirical function of the gap size (s) and the pellet diameter (R_{pellet}), as proposed for example by Kjaerheim *et al.*⁸²:

$$f_{\text{con}} = c_1 + (1 - c_1)c_2^{100s/R_{\text{pellet}}}$$

Others adopted (also) a correction term for the contact pressure applied in h_{con} . More specifically, a constant value to P_{con} was added to ensure a contact contribution at all times. This additional term was occasionally also multiplied by a factor f_{con} .

Most models also consider a reduction in the effective gap size (s) for application in h_{gas} , which is therefore sometimes referred to as the thermal gap as opposed to the mechanical gap.

The heat transfer through conduction in the gas is often based on the model of Ross and Stoute⁷⁷:

$$h_{\text{gas}} = \frac{\lambda_{\text{gas}}}{s + \delta_f + \delta_{cl} + g_f + g_{cl}}$$

where the gas extrapolation lengths g_f and g_{cl} (or temperature jump distance) account for the imperfect heat transport across the solid-gas interface, which is material and gas-pressure dependent (see Refs. 74,75 for more details) and the thermal conductivity of

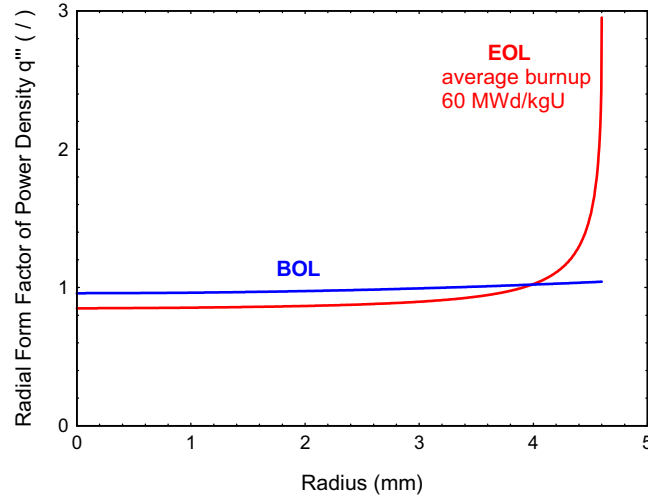


Fig. 2 Radial form factor of the power density q''' at beginning and end of life for “typical” LWR conditions according to the TUBRNP model. The radial distribution of the power density depends on enrichment, rod diameter, neutron spectrum and other parameters. Reproduced from Lassmann, K., Walker, C.T., van de Laar, J., 1998. Extension of the TRANSURANUS burnup model to heavy water reactor conditions. J. Nucl. Mater. 255, 222.

a multi-component gas is only composition dependent and calculated as:

$$\lambda_{gas} = \sum_{j=1}^n \left[\frac{\lambda_j}{\left(1 + \sum_{\substack{k=1 \\ j \neq k}}^n w_{jk} \frac{c_k}{c_j} \right)} \right]$$

with c and w being molar concentrations and weighting factors respectively.

It is important to note that, despite very detailed formulations for the gap conductance, there is an unavoidable uncertainty in the gap size s due to input uncertainties, but also because of uncertainties in the mechanical computation (e.g., cracking, radial relocation of cracked fragments and fuel swelling, see Section 2.13.2.2).

2.13.2.1.4 Heat transport in the fuel pellets

The heat produced by the slowing down of the fission fragments in the fuel pellets is removed through conduction in the pellets, hence it can be described by means of a similar equation as for the cladding:

$$\rho c \frac{\partial T}{\partial t} = \frac{1}{r} \frac{\partial}{\partial r} \left(\lambda r \frac{\partial T}{\partial r} \right) + q''' \quad (4)$$

where c is the specific heat at constant pressure for fuel. The boundary conditions are, however, different:

Inner boundary: $\frac{\partial T(r=r_i, t)}{\partial r} = 0$ (radial symmetry)

Outer boundary: $\Delta T_{gap} = \frac{q''}{h_{gap}}$ (pellet surface temperature is known)

The temperature distribution in the pellets is therefore affected by two terms: the heat source and the fuel thermal conductivity. At beginning of life (BOL), the heat production in LWRs is subject to a slight (typically in the range of 10%) depression, i.e., $q'''_{BOL} \cong I_0(r)$, where $I_0(r)$ is the modified Bessel function. During the irradiation of the fuel, epithermal neutrons are captured preferentially near the surface of the fuel by U^{238} . This leads to an enrichment of Pu^{239} at the outer periphery of the fuel. At end of life (EOL), $q'''_{f,o} \approx (2-3) q'''_{f,i}$, i.e., the power density distribution is a steep function of the radius (see Fig. 2). This effect needs therefore to be considered and a specific model for the radial power density like RADAR,⁸³ TUBRNP,^{30,84} PRODHEL,¹⁹ RTOP,⁵⁰ RAPID⁸⁵ or PLUTON⁸⁶ is a prerequisite for any temperature analysis at high burn-up.

Conduction of heat in the pellets occurs by phonons or by the kinetic energy of electrons (for more details see for example⁸⁷): $\lambda = \lambda_{ph} + \lambda_{el}$. At temperatures below 1500K the phonon contribution predominates. Above this temperature the electronic contribution becomes important. When applying the kinetic gas theory to the propagation of atomic vibrations (phonons) or quasi-particles, it appears that the phonon conductivity in the temperature range of interest can be expressed as

$$\lambda_{ph} = \frac{1}{A + B \cdot T}$$

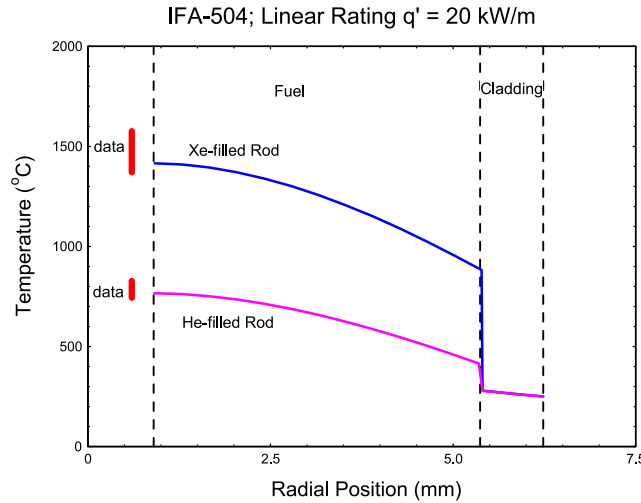


Fig. 3 Radial temperature distribution in a BWR-rod at begin of life. Comparison between the range of experimental results and predictions of the TRANSURANUS code for two different fill gases (He, Xe). The data refer to a thermocouple measurement in the central hole of the fuel pellet, indicated by the dashed line.

where A corresponds to the scattering of phonons by imperfections such as point defects, line and planar defects, fission gas bubbles, etc. The parameter B corresponds to the scattering by phonon-phonon (Umklapp) interactions. When the burnup in the pellets increases, the accumulation of point defects and fission products will increase the phonon scattering (A -term). The same happens if the fuel (e.g., UO_2) is doped with a neutron absorber like Gd_2O_3 , or if a deviation from stoichiometry occurs ($x \neq 0$, where $x = |2 - \text{O/M}|$ and O/M is the oxygen-to-metal ratio in UO_2), i.e., in general $A = A(\text{bu}, \text{Gd}, \text{Pu}, x)$, where bu denotes the local burnup.

The temperature dependent creation of electronic carriers, i.e., excitation of free electrons, leading to λ_{el} is typically expressed as:

$$\lambda_{el} = \frac{C}{T^2} \exp\left(-\frac{W}{kT}\right)$$

Besides the temperature and composition, the phonon contribution is also strongly dependent on the fuel density. Several different formulations exist to account for the reduction of the thermal conductivity of theoretically dense fuel (λ_{TD}) with the porosity level (P) in the pellets^{87,88}:

Maxwell-Eucken: $\lambda = \lambda_{TD} \frac{1-P}{1+\alpha P}$ where α is a function of pore shape

Loeb: $\lambda = \lambda_{TD}(1 - \alpha P)$ where $\alpha = 1.7 - 3$

Brandt and Neuer: $\lambda = \lambda_{TD}(1 - \alpha P)$ where $\alpha = 2.6 - 0.5 T(\text{K})/1000$

2.13.2.1.5 The structure of the thermal analysis

The structure of the thermal analysis in a fuel performance code can best be summarized as follows: The material properties λ , ρ , and c are organized in an independent database whereas the power density q''' , the gap conductance h_{gap} and the heat transfer coefficient between cladding and coolant α are formulated in a model. A numerical algorithm provides the solution of the heat conduction equation in the pellets and the convection problem in the coolant. A typical resulting temperature distribution calculated by means of the TRANSURANUS code is shown in [Fig. 3](#).

2.13.2.2 Mechanical Analysis

The first barrier against release of radioactive fission products to the environment is the cladding of the nuclear fuel rod. The stress and associated deformation assessment of the cladding are therefore essential in fuel performance calculations. Furthermore, the deformation of both the pellets and the cladding affect the gap width, which in turn affects the conductance of the gap, hence the temperature distribution in the pellets. The thermal and mechanical analyses are then equally important and closely coupled. In principle, both problems should therefore be solved simultaneously. In practice, however, many fuel performance codes solve them separately but provide coupling through an iterative scheme. This important numerical aspect will not be dealt with in this article. The interested reader is referred to a general discussion on this issue in Refs. [29,89,90](#).

The next sections summarize how stress and strains are calculated in both the ceramic pellets and the metallic cladding, while underlining the main assumptions and limitations.

2.13.2.2.1 Main assumptions and equations

The main assumptions generally made in 1.5D fuel performance codes are

- (1) The system is axisymmetric, i.e., variables don't vary azimuthally.
- (2) Although the fuel and cladding move axially (not necessarily at the same rate), planes perpendicular to the z-axis remain plane during deformation (generalized plain strain condition), i.e., the rod remains cylindrical as illustrated in Fig. 1.
- (3) Dynamic forces (inertia) are in general not treated, and the time dependence inherent in the analysis (creep) is handled incrementally (quasi-steady).
- (4) Elastic constants are often isotropic and constant within a cylindrical ring, but can be anisotropic in some codes (e.g., FEMAXI⁹¹).
- (5) The total strain can be written as the sum of elastic and non-elastic components.

The first two assumptions reduce the problem to one dimension. For specific studies of local effects such as azimuthal variations in corner rods or pins adjacent to a control rod, as well as local stress build-up around a missing pellet chip, either 2D or 3D analysis tools provide an excellent complement.

The third assumption indicates that the stresses are related through a local equilibrium condition for the radial force in the following form:

$$\frac{d\sigma_r}{dR} = \frac{\sigma_t - \sigma_r}{R}$$

where σ_r and σ_t represent the normal radial and tangential stresses, respectively, and R corresponds to the radius of the deformed geometry.

Since the fuel stack and cladding are treated as a continuous, uncracked medium, no discontinuities are allowed in their displacements. This is translated by the compatibility relations for the strains:

$$\begin{aligned} \epsilon_r &= \frac{du}{dR} \\ \epsilon_t &= \frac{u}{R} \\ \epsilon_a &= C_3 \end{aligned} \quad (5)$$

where u represents the radial deformation and ϵ_i ($i = r, t, a$) are the normal strains.

Finally, the last equation relates the stresses to the strains. Based on the fifth assumption, the constitutive relations read:

$$\underline{\epsilon}^{total} = \underline{\epsilon}^{elastic} + \sum \underline{\epsilon}^{non-elastic} \quad (6)$$

where

$$\underline{\epsilon} = \begin{Bmatrix} \epsilon_r \\ \epsilon_t \\ \epsilon_a \end{Bmatrix} \quad (7)$$

In 1.5D fuel performance codes, the mechanical modeling must necessarily be performed at a certain elevation within the pellet. This is universally chosen to be at pellet mid-height, where a plane axial-strain condition applies. The complications of pellet end effects, including the impact of any dishes or chamfers, are ignored in the mechanical simulation. In contrast, dishes and chamfers are usually modeled explicitly in 2D (e.g., FALCON⁹²⁻⁹⁴) or 3D codes (e.g., ALCYONE^{69,95,96} and BISON^{65,97} which can be applied to either 2D or 3D simulations) via a suitable finite element mesh. More details are provided in the recent review of multidimensional developments for fuel performance modeling.¹

2.13.2.2.2 Calculation of strains

2.13.2.2.2.1 Elastic strain

The elastic strains for an isotropic material are reversible and given by

$$\begin{aligned} \epsilon_r^{elastic} &= \frac{1}{E} [\sigma_r - \nu(\sigma_t + \sigma_a)] \\ \epsilon_t^{elastic} &= \frac{1}{E} [\sigma_t - \nu(\sigma_r + \sigma_a)] \\ \epsilon_a^{elastic} &= \frac{1}{E} [\sigma_a - \nu(\sigma_r + \sigma_t)] \end{aligned}$$

2.13.2.2.2.2 Non-elastic strain

2.13.2.2.2.2.1 Thermal strain

The non-elastic strains consist of various contributions. First of all, there is the thermal strain resulting from temperature differences, which is assumed to be isotropic and reversible:

$$\epsilon_i^t = \alpha \cdot (T - T_0) \quad i \in \{r, t, a\}$$

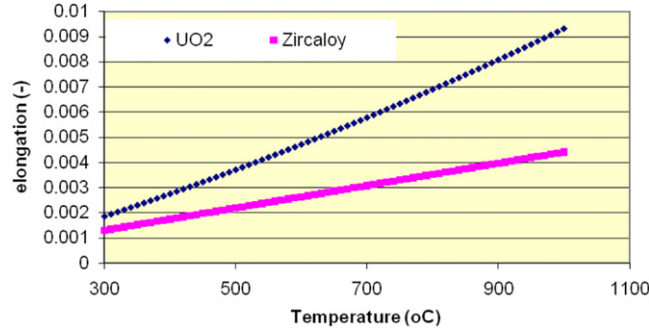


Fig. 4 Elongation of UO₂ fuel and Zircaloy cladding due to thermal expansion (–), as a function of the temperature (°C).

The thermal expansion coefficients depend on the material and the temperature itself, as shown in Fig. 4.

The larger temperature and thermal expansion of UO₂ with respect to that of Zircaloy explains why thermal expansion is one of the largest contributions to the gap closure in a nuclear fuel rod at beginning-of-life in a commercial reactor. Even in a fast breeder reactor fuel pin, containing mixed oxide pellets surrounded by stainless steel cladding with a larger thermal expansion coefficient, the much higher pellet temperature contributes to closure of the initial gap size.

2.13.2.2.2.2 Swelling

The second contribution to the non-elastic strain in the fuel pellets comes from swelling, and is also assumed to be isotropic. The fuel swelling in turn has four contributions:

$$\epsilon_{fuel}^s = \frac{1}{3} \left[\left(\frac{\Delta V}{V} \right)_{solid FP} + \left(\frac{\Delta V}{V} \right)_{gaseous FP} - \left(\frac{\Delta V}{V} \right)_{densification} - \left(\frac{\Delta V}{V} \right)_{hot pressing} \right]$$

where the first term is attributed to the inexorable swelling of solid fission products:

$$\left(\frac{\Delta V}{V} \right)_{solid FP} = bu \cdot \left(\sum_{solid FP} Y_i \frac{v_i}{v_U} - 1 \right)$$

which is linearly dependent on burnup, the fission product yield (Y_i) and on the partial volume of the species (v_i).^{98–100} The second term comes from gaseous fission product swelling

$$\left(\frac{\Delta V}{V} \right)_{gaseous FP} = \frac{4\pi}{3} \int_0^{R_{max}} R^3 N(R) dR$$

and requires a model to predict the gaseous fission product behavior, more precisely, the gas bubble formation due to the low solubility of rare gases in UO₂ (cf. Section 2.13.2.3). In general, estimates for the total fission product swelling rate under normal operating conditions based on the available experimental data range between approximately 0.6%–1% per 10 GWd/t_{HIM}, for rod average burnups below ~60 GWd/t_{HIM}. The swelling rate can decrease with burnup, which has been attributed to the removal of fission gas from the fuel matrix.⁹⁸ During the initial stages of the irradiation ($bu < 10$ MWd/kgHM), the density increases as some fabrication porosity disappears as a result of the impact of fission fragments on the (small) pores. In general, the shrinkage process depends on the temperature, burnup, fission rate as well as combination of the initial density, the pore size-distribution and the grain size. The ideal situation is thus to have a fundamental model for densification, like those proposed by Assmann *et al.*¹⁰¹ and Suk *et al.*¹⁰² However, values for the parameters involved are not always well known. Therefore many code developers have implemented empirical correlations for the fraction of the original porosity which has annealed out as a function of the local burnup, the temperature and the grain size, for example^{55,103}:

$$\frac{\Delta P}{P_0} = \alpha [1 - \beta \exp(-a_1 \cdot bu) - (1 - \beta) \exp(-a_2 \cdot bu)]$$

where $\alpha = (T^\circ C - 83)/(288 D_{gr})$, $\alpha\beta = 5.12 \exp(-5100/T^\circ K)$, $a_2 = 0.0016 t_{UO_2}/MWd$, $a_1 = 100 a_2$. The densification, together with the solid fission product swelling is illustrated in Fig. 5.

Under the influence of large temperatures, stress levels and defect production rates during irradiation, a fraction of the fabrication porosity will disappear. This fourth contribution to fuel swelling is referred to as hot pressing and is similar to creep (see below). Therefore, either vacancy diffusion

$$\frac{dP}{dt} = -K \left(\frac{\Omega D_{vol}}{kT} \right) \frac{P}{R_{gr}^2} \sigma$$

or plastic flow (i.e., dislocation climb or other model of creep)

$$\frac{dP}{dt} = -\frac{9}{4} \alpha \sigma P$$

are considered.⁷¹

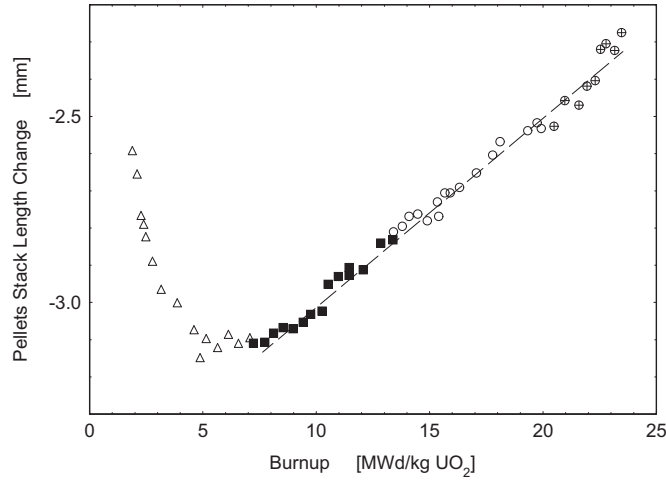


Fig. 5 Change of the fuel pellet stack length (mm) at beginning-of-life as a function of the burnup (MWd/kg UO₂), showing the combined effect of densification and solid fission product swelling. Reproduced from White, R.J., 2001. Measurements of Pellet and Clad Dimensional Changes in the Halden Reactor, HWR-678. Halden: OECD Halden Reactor Project.

The isotropic swelling strain in the cladding is due solely to void formation; hence it requires a model for the evolution of voids in the metal.

2.13.2.2.2.3 Plasticity and creep

The third contribution to the non-elastic strain in the fuel is visco-plastic in nature. It consists of instantaneous plastic deformation when the yield stress is exceeded and of time-dependent creep. For the fuel and cladding a simple isotropic plastic flow model can be applied. Nevertheless, as creep is the main contributor to stress relaxation after cracking (see below) in the oxide pellets, plastic deformation is often only considered in the cladding.

In a multi-axial state of stress, a method of relating the onset of plastic deformation to the results of a uniaxial test is required. Furthermore, when plastic deformation takes place one needs to determine (1) how much plastic deformation has occurred and (2) how that deformation is distributed among the individual components of strain in the principal directions. For the first requirement a so-called yield-function is needed. This may be one-dimensional like the Von Mises criterion, assuming that the shear stress is neglected and the material is isotropic^{91,105}:

$$\sigma_{eff} = \frac{1}{\sqrt{2}} [(\sigma_r - \sigma_t)^2 + (\sigma_r - \sigma_a)^2 + (\sigma_t - \sigma_a)^2]^{1/2}$$

so that yielding only occurs when the effective or equivalent stress (σ_{eff}) exceeds the yield stress determined from a uniaxial tensile test. Others have introduced the anisotropic factors according to Hill's methodology.⁷³ Finally, a multidimensional yield surface^{106,107} has also been proposed. In order to account for work hardening, one generally assumes that the yield stress changes with the total permanent deformation. The plastic strain is therefore computed incrementally.

In order to answer the second question, each increment of effective plastic strain is related to the individual plastic strain components by a flow rule:

$$\Delta \epsilon_i = \Delta \epsilon_{eff} \frac{\partial \sigma_{eff}}{\partial \sigma_i} \quad i \in \{r, t, a\}$$

When using the above mentioned definition of the equivalent stress, one obtains the Prandtl-Reuss flow rule¹⁰⁸:

$$\Delta \epsilon_i^p = \frac{3 \Delta \epsilon_{eff}^p}{2 \sigma_{eff}} S_i \quad i \in \{r, t, a\}$$

indicating that the plastic strain increment is proportional to the deviatoric stress $S_i = \sigma_i - \sigma_h$ where $\sigma_h = (\sigma_r + \sigma_t + \sigma_a)/3$, is the hydrostatic stress.

For the time-dependent creep one needs strain rate equations, although the total creep strain is also computed incrementally by multiplying the strain rate with the time step length. For primary creep, typically an empirical expression is applied:

$$\dot{\epsilon}_{eff} = K \sigma_{eff}^n t^m$$

where K , n , m are constants.

For the secondary or steady-state creep, there are three parallel processes. The vacancy diffusion or Nabarro-Herring creep and the dislocation climb are dominating at high temperature and high stresses, respectively:

$$\begin{aligned} (\dot{\epsilon}_{eff}^c) &= \frac{B q^m \sigma_{eff}}{R_g^2} \exp\left(-\frac{E_d}{kT}\right) \text{ vacancy diffusion} \\ (\dot{\epsilon}_{eff}^c) &= B' q^m \sigma_{eff}^{4.5} \exp\left(-\frac{E_d}{kT}\right) \text{ dislocation climb} \end{aligned}$$

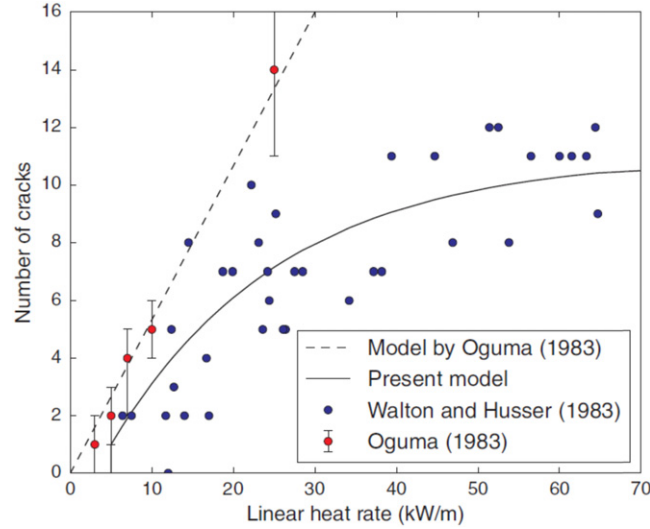


Fig. 6 Number of radial cracks as a function of the linear heat rate obtained from measurements on fuel cross sections and models of Oguma and Barani *et al.* Reproduced from Walton, L.A., Husser, D.L., 1982. Fuel pellet fracture and relocation. In: Proceedings of the Specialists Meeting on Water Reactor Fuel Element Performance Computer Modeling, IWGFPT/13, March 15–19, 1982, p. 147. Preston, UK: IAEA. Oguma, M., 1983. Cracking and relocation behavior of nuclear fuel pellets during rise to power. Nucl. Eng. Des. 76, 35. Barani, T., Pizzocri, D., Pastore, G., Luzzi, L., Hales, J., 2019. Isotropic softening model for fuel cracking in BISON. Nucl. Eng. Des. 342, 257.

The third process is irradiation induced creep, dominating at low temperatures and assumed to be proportional to the effective stress and the local fission rate density or q''' .

2.13.2.2.2.4 Pellet cracking

The fourth and last non-elastic strain component stems from the pellet cracking. Pellet cracking already occurs at startup with fresh fuels due to the differential thermal expansion since the hot pellet center expands more than the cold periphery. In order to assess the linear heat generation rate at which cracking in cylindrical pellet occurs, the maximum thermal stress ($= \sigma_{t,max} = \sigma_{a,max}$ at pellet periphery) in an uncracked pellet submitted to a parabolic temperature gradient

$$\sigma_{t,max} = -\frac{\alpha E q'}{8\pi(1-\nu)\bar{\lambda}},$$

must be compared with the (uniaxial) fracture stress, which is approximately 130 MPa. When using $E = 200$ GPa, $\nu = 0.31$, the thermal diffusivity $\alpha = 10^{-5} \text{K}^{-1}$, and an average thermal conductivity of $\bar{\lambda} = 3 \text{ W m}^{-1} \text{K}^{-1}$, radial cracks are predicted to be initiated in the pellet periphery at a linear heat rate q' of the order of 5 kW m^{-1} . The number of cracks (N_{cr}) is dependent on the linear heat rate. Oguma¹⁰⁹ proposed a linear model for the number of radial cracks, while Barani *et al.*¹¹⁰ suggested a more elaborate correlation leading to a saturation of the number of cracks as a function of the linear heat rate as illustrated in Fig. 6. In addition to radial, also axial or transverse and (especially under ramping conditions or in high burnup fuel following pellet-clad bonding) circumferential cracks are formed.

The consequences of cracking are very important in fuel performance modeling. Owing to the larger thermal expansion of the fuel fragments in comparison with that of a monolithic cylinder, and due to vibration induced motion, fragments move outwards. This is called pellet-fragment “relocation” and has a strong impact on the thermal behavior. Relocation reduces the pellet-cladding gap size (Fig. 7), thereby reducing the temperature levels in the fuel at beginning-of-life (Fig. 8). This constitutes the largest contribution to the gap closure (approximately 30%–50%, depending on q') but is also the one which is subject to the largest uncertainty, because of the stochastic nature of the cracking process. This also raises questions about the usefulness of applying 3D stress calculations because uncertainties about the precise knowledge of every crack location and orientation, as well as the corresponding friction coefficients and relocation of every pellet fragment practically prevent an accurate assessment of the 3D stresses and strains. Nevertheless, 3D models provide a deeper understanding of the phenomena at hand.

The contribution from relocation is generally accounted for in the tangential strain component as a (linear) function of the linear heat rate: $\epsilon_t = u/r$, where $u = s\delta_g$, s being the initial radial gap size and δ_g the fraction of the gap size closing as a result of relocation. An example based on the relocation model in the FRAPCON3 code¹¹¹ is illustrated in Fig. 7.¹¹²

When the pellets swell large enough so that they come into contact with the cladding, which creeps down under influence of the pressure difference between the coolant pressure and the fill gas pressure, then relocation may be (partly) reversed. If both pellet swelling and cladding creep-down continue, the gap is closed and the pellet fragments are pushed inwards, so that the relocation is approaching total elimination.

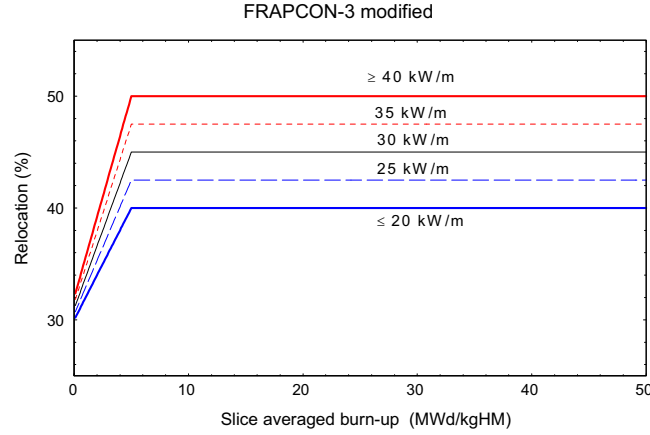


Fig. 7 Fraction of gap closure due to pellet fragment relocation (δ_g), derived from the relocation model in the FRAPCON3 code.

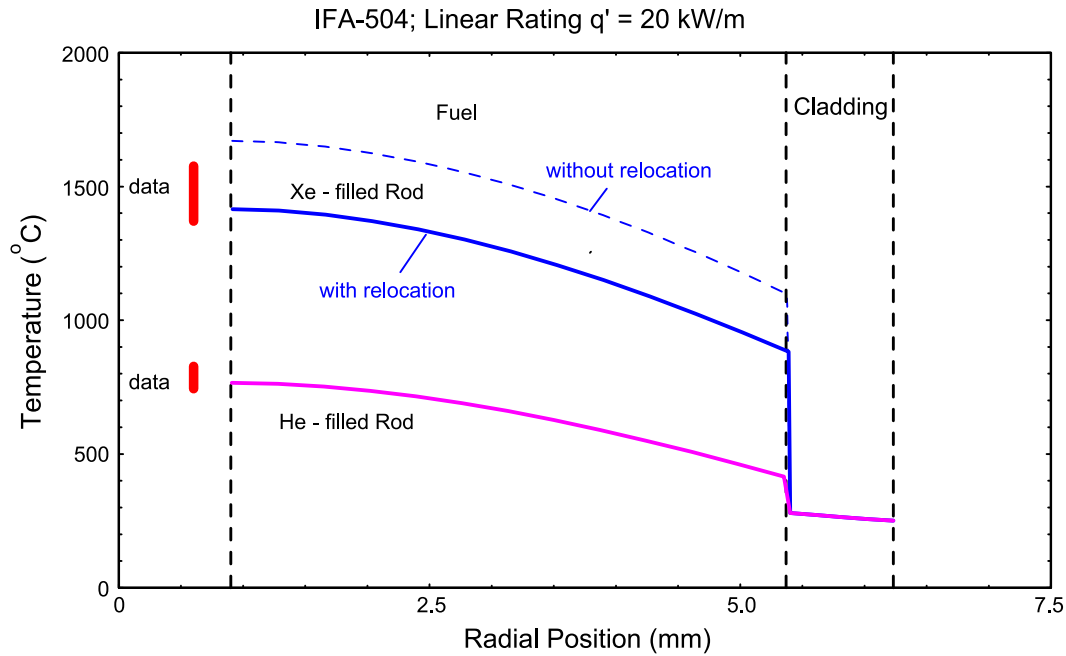


Fig. 8 Radial temperature distribution in a BWR-rod (IFA-504) at beginning of life calculated by the TRANSURANUS code. Comparison between the analysis of a Xe-filled rod with (full line) and without (dashed line) taking relocation into account, and comparison with a He-filled rod considering relocation as well.

The effect of relocation on the mechanical behavior is also of primary importance since it reduces the overall thermal stress in the pellets and may even change the sign of the stress in the pellet center from compression (in a cylinder) to traction (in fragments).¹¹³ To account for the cracks rigorously would require considering the exact location and size of every crack and solving a 3D stress-strain problem in each block. Instead, in most cases, one simply modifies either the material constants^{91,112} or modifies the constitutive equations. An example of the former approach is that of Jankus and Weeks,¹¹⁴ where a reduction of the elastic constants is proposed:

$$E' = \left(\frac{2}{3}\right)^{N_{cr}} E$$

$$\nu' = \left(\frac{1}{2}\right)^{N_{cr}} \nu$$

which means that an equivalent continuous and homogeneous solid body with directionally dependent (anisotropic) properties is considered. The scaling factors for the elastic constants as a function of the number of cracks according to the Jankus-Weeks model are plotted in **Fig. 9**. As the pellet-clad gap closes during irradiation the contact pressure can press the fragments inward, thereby reducing

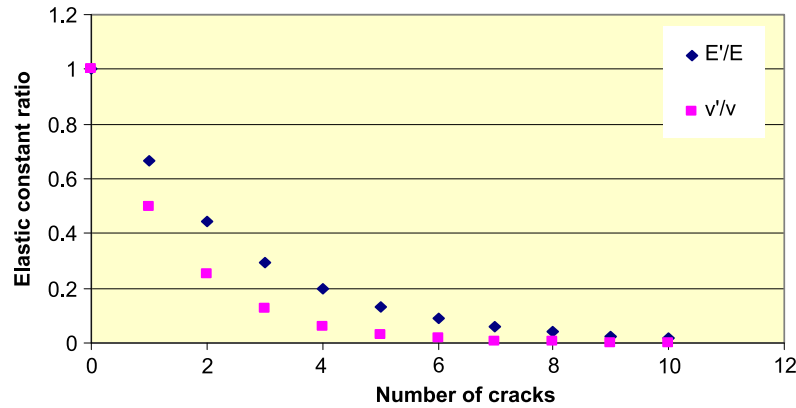


Fig. 9 Effect of the number of cracks on the elastic modulus and the Poisson ratio according to Jankus *et al.* Reproduced from Jankus, V.Z., Weeks, R.W., 1972. LIFE-II – A computer analysis of fast-reactor-fuel-element behaviour as a function of reactor operating history. Nucl. Eng. Des. 18, 83.

the relocated radius to a minimum value. Some codes also account for the restoration of the elastic constants as the relocation is reversed (partially).⁹¹

In order to modify the constitutive equations, a plane stress condition has been proposed¹⁰⁶, i.e., the tangential stress is set equal to the fill gas pressure once the radial crack appears. Both types of approaches, however, do not account for crack healing that could occur at high temperatures and under compression.

2.13.2.2.3 Boundary conditions

In order to solve the main equations summarized in Section 2.13.2.2.1, boundary conditions are required.

2.13.2.2.3.1 Radial boundary conditions

In general, continuity of the radial stress and displacement at each radial zone is imposed and the radial stress at the outer cladding surface is determined by the coolant pressure: $\sigma_r(r_{cl,o}) = -p_{cool}$.

The boundary condition in the rod depends on the configuration. When pellet-cladding mechanical interaction is not established, the radial stress at the pellet periphery is determined by the fill gas pressure in the fuel rod (p_{gas}): $\sigma_r(r_{f,o}) = -p_{gas}$. For the boundary condition in the pellet center, two possibilities exist. In hollow pellets, the radial stress at the pellet center is equal to fill gas pressure as well: $\sigma_r(r_{f,i}) = -p_{gas}$, whereas in the event of full cylindrical pellets the radial and tangential stresses are equal in the pellet center.

When the fuel and cladding are in contact, a fuel pellet interfacial pressure exists (p_{fc}) and determines the boundary condition at the pellet surface: $\sigma_r(r_{f,o}) = \sigma_r(r_{cl,i}) = -p_{fc}$. The other radial boundary conditions remain unchanged.

2.13.2.2.3.2 Axial boundary conditions

The plane strain assumption entails that the axial strain is constant in the plane perpendicular to the axial axis. The axial strain is therefore determined by an axial force balance equation including the fill gas pressure, the plenum spring pressure, the fuel column weight, the friction forces and the coolant pressure imposed on both end plugs of the cladding. The friction forces depend on the fuel-cladding interaction and can only be taken into account iteratively. Indeed, when one of the axial sections i is analysed it is not known whether friction forces between fuel and cladding originating from a section above/below i need to be considered in the axial balance of forces. This is schematically shown in Fig. 10. In the case of a radial contact between fuel and cladding both bodies may stick to each other, but some sliding may be possible in specific conditions (sticking or static versus sliding friction). Part of the fuel rod may be “trapped”, which means that rather high axial forces may act on cladding and fuel.

2.13.2.2.4 Pellet-cladding interaction

2.13.2.2.4.1 Pellet-cladding mechanical interaction

Pellet-cladding mechanical interaction (PCMI) is one of the important analytical targets in predicting fuel behavior, since it can be a cause of fuel failure. The mechanical interaction of the fuel with the cladding is mainly caused by the different thermal expansion of the two components, fuel relocation and swelling, and cladding creep-down (see Section 2.13.2.2.2). However, the poor thermal conductivity of the fuel entails a strong temperature gradient across the pellet. The resulting thermal stresses exceed the fracture stress of UO_2 (around 100 MPa) causing pellet fracture. Once the pellet has fractured, it is able to deform much more readily under the effects of the temperature field, and the differential thermal expansion causes the pellet ends to bow outwards leading to the so-called hour-glass shape of pellets. This leads to earlier gap closure and PCMI at the locations corresponding to the pellet ends (see Fig. 11).

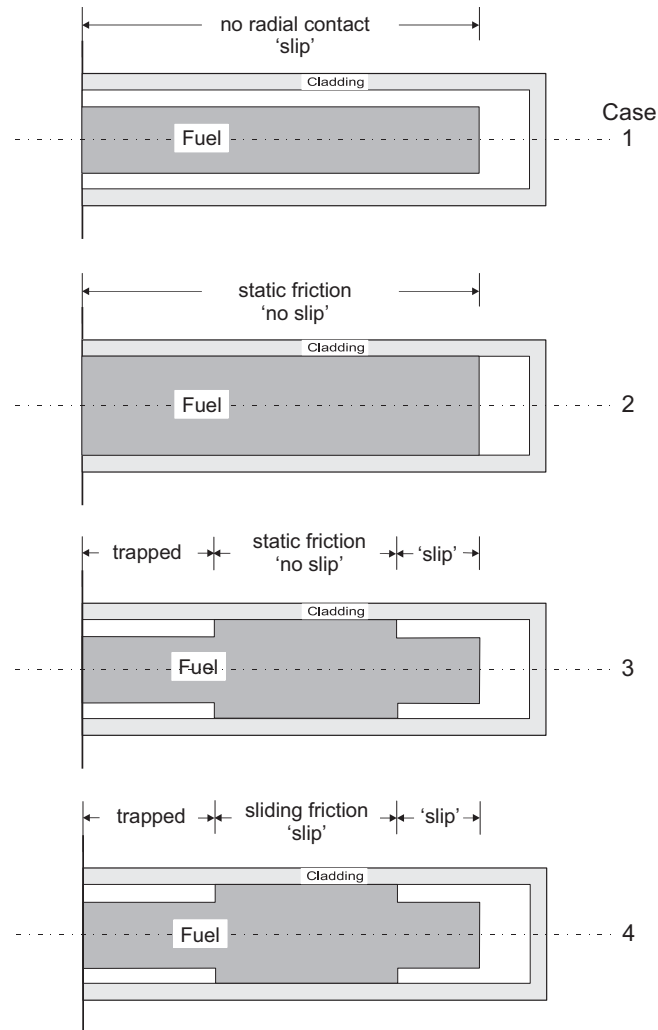


Fig. 10 Four possible modes of an interaction between fuel and cladding.

PCMI in the early stage of irradiation is therefore caused by the differential thermal expansion of the pellets, leading to a bamboo or ridging deformation of the cladding. The ridges in the cladding, whose height can reach 20 μm at high powers, coincide with the pellet ends and during PCMI can cause hoop stresses of around 400 MPa in the cladding, which are close to the cladding yield stress. When chemically aggressive fission products such as iodine are in their vicinity, these local concentrations of stress and strain have led to the so-called Stress Corrosion Cracking (SCC) in LWR fuel systems. The likelihood of PCI-SCC failure can increase significantly in cases where undetected manufacturing defects, in particular, missing pellet surfaces (MPS), are present in the fuel pellets.

The onset of PCMI is affected by a number of design and fabrication parameters. First of all, the pellet geometry is adapted to extend the onset and to mitigate PCMI. In particular, the pellet height has been reduced with respect to its diameter while chamfers were applied for delaying PCMI and reducing the probability of fuel chipping. Secondly, the rod geometry is important. More precisely, the width of the original clearance between the pellets and the cladding should be large enough. Nevertheless, the gap size is subject to many uncertainties, the largest being the pellet fragment relocation. In addition, it is generally assumed in fuel performance modeling that the pellets are located concentrically within the cladding, although this is seldom the case. Any eccentricity in the stacking arrangement, resulting from fabrication or fuel rod handling, is likely to lead to premature onset of PCMI even though its effect will diminish as gap closure occurs.

Once PCMI has started, both the pellet geometry and the material properties of the interacting components influence the maximum stresses and strains as well as their evolution. Flat-ended pellet stacks will generate larger axial expansion in comparison with dished stacks, especially in fresh fuel. This is due to the fact that in flat-ended pellets the hot central part determines the maximum length change, whereas for dished pellets there is no contact between pellets along the central axis (when the power is not too high), hence the axial expansion will be controlled by outer (cooler) regions of the pellet. In practice, the ratio of axial to tangential strain can vary between 0.2 for large dishes and 2 for undished pellets.¹¹⁵ Nevertheless, the axial expansion from

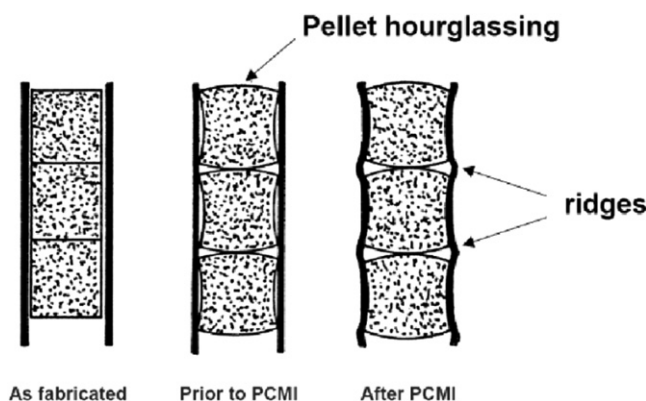


Fig. 11 Schematic presentation of pellet-cladding mechanical interaction.

flat-ended pellets can diminish with burnup because of in-pile dishing, for instance caused by densification and creep in the hot central parts of the pellets during PCMI (e.g., in Ref. 104).

In addition to the difficulties to reproduce two-dimensional (local) pellet deformations during PCMI by means of one-dimensional fuel performance codes, there are other challenges to be dealt with. Apart from pellet and cladding eccentricity and slanting, which mostly affect the onset of PCMI, there are uncertainties related to the assessment of the stress in cracked pellets, to pinching by assembly grids, as well as to the (static and dynamic) friction coefficient between pellets and cladding. In particular the slipping is severely restricted by the interaction layer that establishes between both components after gap closure at higher burnups.

Therefore, for these PCMI evaluations, the (local 2D) finite-element method (FEM) is in principle a more advantageous method than the finite difference method (FDM). FEM considers the reaction forces exerting among all the ring elements of pellet and cladding into one single matrix to obtain a numerical solution,⁹¹ while in FDM displacements of each ring elements of pellet and cladding are summed up independently to determine the diameter change, implying that FDM is actually modified to some extent to cope with mechanical interactions among the ring elements. Currently, 3D fuel performance codes are being developed.^{95,116–120}

2.13.2.2.4.2 Irradiation induced stress corrosion cracking

Failures during power variations are not only attributed to stress. Stresses increase at the intersection of radial crack planes, the inter-pellet planes and the inner surface of the cladding. The brittle nature of the failure site, however, has led to the general consensus that although stress is the primary initiator, propagation of the crack is chemically assisted, thus the process is termed Stress Corrosion Cracking (SCC), as mentioned above. The chemical assistance for brittle cracking in all probability arises from the environment established by fission products release into the fuel-to-clad interspace with isotopes of iodine as main candidates as the principal corroding species. There is some discussion as to whether or not the corrodent must be freshly released from the fuel or whether it is sufficient for it to have accumulated in the fuel-to-clad gap throughout the irradiation period prior to the over-power transient.

Since its discovery in CANDU and BWR in the 1970s, four factors affect the incidence of PCI-SCC failures and were reviewed by Cox in 1990¹²¹ and more recently by Piro¹²²: stress, time, material and chemical environment. Understanding the important variables for PCI-SCC enables fuel designers to propose solutions. They have adapted the fuel geometry (reducing the height to diameter ratio, introducing dishes and chamfers), imposed restrictions on the power variations, modified the fuel assembly design and applied coatings on the inner cladding surface in order to reduce the friction coefficient and to accommodate in a ductile manner the biting of pellet ends. More precisely, in BWRs Cu and Zr barriers were applied in the form of thin metallic layers as an integral part of the tube fabrication process. The pure zirconium (of either crystal bar or sponge origin^{123,124}) has been adopted as the standard barrier, because irradiation experience showed that copper offered less protection after high irradiation doses. However, pure zirconium oxidizes more rapidly in comparison with Zircaloy while the terminal solubility of hydrogen is lower in the liner.¹²⁵ Accordingly, when a primary defect occurs in the cladding for instance due to debris fretting, water ingress will oxidize both the fuel and the liner. This occurs typically in the lower (cooler) part of the fuel rod. The hydride formation near the cladding inner diameter can lead to a sunburst hydride and would, due to the volume increase, set up tangential stress in the Zircaloy part of the cladding, which can promote crack formation. The local hydrogen absorption can cause more severe hydriding and therefore secondary defects in the form of long axial splits and circumferential cracks. Secondary cladding defects in LWR fuel can cause large releases of uranium and fission products to the primary coolant,¹²⁶ and seem to be correlated with PCI cause for instance by control blade movements in BWRs. Mitigation of these secondary failures has been achieved by increasing the number of rods per assembly¹²⁷ (e.g., from 6×6 to 10×10 in BWR assemblies) in order to reduce the linear heat generation rate per rod, and by alloying the liner with either Fe¹²⁸ or Sn.¹²⁹

A more recent component of PCI resistant fuel designs is the use of softer fuel pellets obtained by means of large grained doped UO_2 for both BWR and PWR applications. Since the early 1990s AREVA has developed an optimized chromia-doped UO_2 fuel that exhibits significantly higher performance compared to standard UO_2 .¹³⁰ The grain sizes are on the order of 60 μm compared to 10 μm in standard UO_2 . As a result the fuel releases less fission gas and is less prone to PCI failures during ramp tests thanks to a larger creep rate.¹³¹ Post irradiation examinations after ramp tests revealed a larger number of radial cracks on the pellet periphery. Recent two-dimensional finite element simulations of PCI have shown that this can be attributed to the larger friction due to fuel-clad bonding in high burnup fuel and the reduced fracture stress of the doped fuel.¹³² The simulations also indicate that, unlike the hoop stress, the shear stress distribution in the cladding is smoother thanks to the reduced fracture stress of the doped fuel, i.e., thanks to the larger number of radial cracks in the periphery of the pellets.

Modeling PCI has evolved since the first attempts aiming at the fitting of the time to failure (or failure probability), maximum power and power increase to experimental data, although the uncertainty could reach a factor of 5.¹³³

The initial step is either assumed to occur at pre-existing flaws¹³⁴ according to a frequency distribution, or to occur spontaneously when a threshold such as the iodine concentration is exceeded.¹³⁵ More recently, Park *et al.*¹³⁶ postulated that pits would generate preferentially around grain boundaries and coalesce to form a microcrack, referred to as grain boundary pitting coalescence. The micro-crack is assumed to develop into an incipient crack, initiating and propagating along the grain boundary.

For the simulation of crack propagation, most authors apply linear elastic fracture mechanics (LEFM), in line with Kreyns *et al.*¹³⁷ By fitting the experimental data of Wood,¹³⁸ they advocated that the crack velocities could be related to the fourth power on the stress intensity factor K_I :

$$\frac{da}{dt} = C \cdot K_I^4$$

where a is the crack length and C is a constant. The crack intensity factor was shown to be controlled by the elastic stress field at a flaw tip as described by K_{Iv} , rather than the nominal applied stress:

$$K_{Iv} = \sigma \sqrt{aY}$$

where σ represents the nominal hoop stress and the factor Y incorporates a correction factor to account for the finite width of a defect-bearing component. Nevertheless, Kreyns *et al.*¹³⁷ pointed out that small scale plasticity will occur near the crack tip, in a cone with radius r_p :

$$r_p = \frac{1}{\sqrt{6\pi}} \left(\frac{K_{Iv}}{\sigma_y} \right)^2$$

where σ_y corresponds to the yield stress, and $K_{Iv} = \sigma \sqrt{a_{eff}Y}$, which results in an effective crack length:

$$a_{eff} = a + r_p$$

and the effective correction factor $Y_{eff} = Y \sqrt{\frac{a_{eff}}{a}}$ becomes

$$Y_{eff} = \frac{Y}{\sqrt{1 - \left(\frac{a}{\sigma_y} \right)^2 \left(\frac{Y^2}{6\pi} \right)}}$$

Anderson¹³⁹ provided a general correction factor so that K_I can be expressed more generally:

$$K_{Iv} = \frac{pR}{t} \sqrt{\frac{\pi a}{Q}} F \left(\frac{a}{2c}, \frac{a}{t}, \frac{R}{t} \right)$$

where p is the internal pressure on the tube (MPa), R the mean tube radius, t the tube wall thickness, Q the shape factor for an elliptic crack

$$Q = 1 + 1.464 \left(\frac{a}{c} \right)^{1.65}$$

c is the half length of the crack and F is a boundary correction factor that depends on the shape of the initial crack formed at the inner cladding surface. Park *et al.*¹³⁶ applied an expression for F within the range of $5 \leq R/t \leq 20$, $2c/a \leq 12$ and $a/t \leq 0.8$:

$$F = 1.12 + 0.053\xi + 0.0055\xi^2 + (1 + 0.02\xi + 0.0191\xi^2) \frac{(20 - \frac{R}{t})^2}{1400}$$

where $\xi = \frac{a}{t} \frac{a}{2c}$

The K_{Isc} value provided by Park *et al.* was 3.3 MPa $\text{m}^{0.5}$ and 4.8 MPa $\text{m}^{0.5}$ for stress relieved and recrystallized Zircaloy-4, respectively.

Zhou *et al.*¹³⁴ replaced the constant C in the equation for the crack velocity by a function of the iodine concentration and an Arrhenius-type temperature dependency. More importantly, however, they also involved the pellet cladding contact pressure in the estimation of the stress intensity factor. The local effect of the frictional shear forces is accounted for by adopting the Coulomb friction model, according to which the friction force is proportional to the contact pressure. The extension of Zhou *et al.* is in line with recent findings of Michel *et al.*¹⁴⁰ Based on two-dimensional and three-dimensional finite element computations, they showed that the tangential stress concentration in the cladding is proportional to the shear loading transmitted at the pellet-clad interface. As a result, the peak hoop stress at the inner surface of the cladding depends on the interfacial shear stress and the

uniform loading in the hoop direction. Nevertheless, the simulations did not account for cladding anisotropy, nor for stress relaxation due to crack growth.

Stress relaxation was accounted for in an empirical manner by Mattas *et al.*¹⁴¹ They assumed the chemical (intergranular) crack-growth rate to have an initial value and to decrease exponentially as the crack depth increases. Chemical crack growth was postulated to continue until a critical stress intensity for cleavage and fluting was achieved, at which point intra-granular cleavage initiated until failure.

As pointed out by Rousselier *et al.*¹⁴² stress relaxation and the ensuing crack arrest is necessary to explain a so-called discontinuity observed during ramp experiments: depending on the maximum power of the fuel rod, either a through crack is obtained within a maximum of ten minutes or the SCC damage is limited to a few microns, even after hours at the maximum power. This discontinuous behavior was observed above the SCC initiation threshold of about 300 MPa in Zircaloy-4.¹⁴³ Rousselier *et al.* attributed this to the stress relaxation and to the fact that the intergranular crack could leave the stress concentration zone at the crack tip. Crack arrest was postulated to occur when at the same time the stress intensity factor would be below a certain threshold ($K_I \leq K_{IA}$) and the stress intensity factor would decrease. However, quantitative information cannot be directly inferred from their analysis, since the critical stress corresponding to K_{IA} should depend on the material (stress relieved versus recrystallized), the irradiation as well as the loading history. Furthermore, the LEFM should not be applied without corrections for the visco-plastic behavior and finally, because of the local inhomogeneities of the material at the scale of the crack one should apply local rather than global criteria such as $K_I \leq K_{IA}$.

With the advent of improved hard- and software on one hand, and more detailed experimental data on the other hand, more detailed models are being developed at various scales. At the electronic and atomic scale, first principle computations should enable analysing the individual effect of impurities such as iodine on the binding energies, in much the same way as Xin *et al.*¹⁴⁴ have studied the point defects properties and their interactions with Nb in Zr or Kaji *et al.*¹⁴⁵ analysed the clustering of Ni in Fe. By means of finite element computations on the level of crystallographic grains, Rousselier *et al.* suggest avoiding the limitations associated with LEFM for crack initiation and propagation. Because of the excessive computation time and the lack of precise data of some model parameters, their model is not applicable in fuel performance codes but should enable analysing the effect of corrosive fission products on the intergranular damage by coupling the mechanical problem with a diffusion problem. A similar tool has already been developed by Musienko *et al.*¹⁴⁶ although the corrosive environment parameters are accounted for by a phenomenological approach, i.e., via an effective diffusion coefficient. At the meso-scopic scale, Kaji *et al.* developed a two-dimensional model for SCC growth, in order to analyse qualitatively the effect of load (normal versus shear stress) and grain boundary corrosion on the branching aspect of crack growth. The macroscopic models are mostly based on finite element simulations.^{132,140} These tools provide deeper insight and qualitative information about the various parameters affecting PCI as explained above. Nevertheless, these models are not yet capable of replacing the simplified one-dimensional models implemented in fuel performance codes, despite the improvements of hard- and software. Marchal *et al.*¹³² are trying to develop analytical “enrichments” for one-dimensional models in fuel performance codes based on the two-dimensional models (see for example 147). The stochastic nature of cracking along with the complex evolution of material properties and boundary conditions during irradiation remain the most important difficulties to be tackled.

2.13.2.2.4.3 Outside-in cracking caused by power ramps

High burnup fuel rods in LWRs are characterized by the absence of a clearance between the pellets and their metallic containment. As a direct result, PCMI in the power ramp of high burnup fuel is characterized by a direct stretching of cladding by the pellet, in which cladding is subjected to both hoop tensile stress and axial stress, i.e., to a bi-axial stress state.¹⁴⁸ During power ramp tests with high burnup BWR rods, a failure mechanism therefore occurred from the cladding outside towards the inner surface of the Zircaloy¹⁴⁹ as opposed to the standard PCI-SCC as discussed above. Post irradiation examination revealed that the process started with an axial split with cracking of radial hydrides that had formed during the power ramp test, followed by a step-by-step cracking of hydrides at the crack tip. The process bears similarities with secondary hydride failures discussed above. The radial temperature gradient in the cladding wall and the hoop tensile stress due to the ramp test facilitate the hydrogen diffusion and precipitation of radial hydrides on the outer surface of the tube. These hydrides can crack under the influence of stress caused by PCMI and progressing towards the inner tube surface. The main difference with secondary hydride failures that start on the inner surface is that hydrogen is already absorbed and accumulated at the outer surface due to clad oxidation during normal operation.

2.13.2.3 Fission Gas Behavior

On average, each fission event produces approximately 0.3 Xe and Kr atoms. These inert fission gas atoms are virtually insoluble in the fuel and thus tend to migrate out of the matrix, form bubbles inside and on the boundaries of fuel grains, and ultimately escape to the exterior of the fuel pellet. Consequently, fission gas behavior is associated with two important life-limiting phenomena in the fuel rod, i.e., swelling due to gas retained in the fuel and fission gas release (FGR) to the fuel-to-cladding gap and plenum. Gaseous fuel swelling promotes PCMI, which may lead to cladding failure, in particular under extended burnup and/or transient conditions such as postulated reactivity-initiated accidents (RIA). FGR increases the rod internal gas pressure and degrades the heat transfer across the gap. Through the increase in rod pressure, FGR tends to accelerate cladding ballooning and

burst during a postulated loss-of-coolant accident (LOCA). Through the gap heat transfer degradation, it results in higher fuel temperatures, which in turn may lead to higher FGR (thermal feedback).

In this section, first, the basic mechanisms of fission gas release and gaseous swelling in LWR fuel are summarized. Then, modeling of these phenomena for application to engineering fuel analysis is discussed. The interested reader will find more details in Refs. 150–152.

2.13.2.3.1 Basic mechanisms

The fundamental physical processes that govern fission gas behavior in irradiated UO_2 may be outlined as follows. Fission gas atoms generated in the fuel grains diffuse towards the grain boundaries through repeated trapping in and irradiation-induced resolution from intra-granular bubbles. Gas transport to grain boundaries results in nucleation and progressive growth and coalescence of inter-granular bubbles. Inter-granular bubble evolution brings about fuel swelling and eventually leads to the formation of a tunnel network at grain edges, through which a fraction of the gas is released to the fuel rod free volume. The individual mechanisms are briefly overviewed below.

2.13.2.3.1.1 Recoil, knockout and sputtering

In general, a fission event entails – among others – two fission fragments that convey their kinetic energy to the fuel lattice. A fission fragment, close enough to a free surface ($< 6\text{--}7\ \mu\text{m}$), can escape from the fuel due to its high kinetic energy (60–100 MeV). This is called recoil release. When fission fragments make elastic collisions with the nuclei of lattice atoms, a collision cascade appears. The interaction of a fission fragment, a collision cascade or a fission spike with a stationary gas atom near the surface can also cause the latter to be ejected if it happens within a distance close enough to the surface. This process is called release by knockout. Finally, a fission fragment traveling through the fuel matrix loses energy, causing a high local heat pulse. When this happens close to the fuel surface, a heated zone will evaporate or sputter, thereby releasing any fission product contained in the evaporated zone (sputtering).

Recoil, knockout and sputtering can only be observed at low enough temperatures for thermally activated processes (cf. below) not to dominate fission gas release. These processes are almost temperature independent and therefore called athermal release mechanisms. Athermal release generally contributes less than 1% to the release of the generated gas.^{153,154}

2.13.2.3.1.2 Lattice diffusion of single gas atoms

The first and basic step in thermal fission gas release is transport of gas atoms from within the grains to grain boundaries. This process is governed by lattice diffusion of single gas atoms and the concomitant interaction with the fuel microstructure, in particular, gas atom trapping by intra-granular bubbles and irradiation-induced resolution from bubbles back into the lattice. In this paragraph, unperturbed diffusion in the bulk lattice is referred to; interaction with fission gas bubbles or other sinks is discussed later.

The mechanisms by which the inert gas atoms migrate through the fuel have been studied by Grimes¹⁵⁵ by considering low-energy migration pathways between solution sites, as well as the stability of gas atoms at a variety of solution sites within a defective $\text{UO}_{2\pm x}$ lattice (where $x=|\text{O}/\text{M}-2|$ is the deviation from stoichiometry). According to Grimes' calculations, Xe is trapped at a single uranium vacancy in UO_{2+x} , at a tri-vacancy cluster (i.e., a Schottky defect) in UO_{2-x} and at a di- or tri-vacancy in UO_2 . This conclusion on the preferred trap sites for Xe is confirmed by many studies employing density functional theory (DFT) and molecular dynamics (MD) techniques, as reviewed in Ref. 151. The possible solution sites for fission products in $\text{UO}_{2\pm x}$ are represented in Fig. 12. Since the local environment of the migrating Xe atoms is assumed to be the charged tetra-vacancy for all stoichiometries, the mechanism for diffusion involves the association of a cation vacancy to the trap sites. (Uranium vacancies, as the slower moving species, are rate-controlling for most diffusion-related processes in UO_2).

The lattice diffusion coefficient is influenced by the temperature, deviations from stoichiometry and additives (e.g., Cr, Nb), phase changes and therefore also indirectly by the burnup. Moreover, the passing fission fragments contribute to the diffusion process, which is referred to as irradiation-induced (or athermal) diffusion. This is due to the interaction of the fission fragments and the associated irradiation damage cascades with the fission gas atoms in the lattice, which result in a displacement of the gas atoms. This effect dominates the diffusion process at temperatures below about 800°C and is independent of temperature. At temperatures between 800°C and 1400°C, approximately, vacancies necessary for gas atom diffusion are assumed to be created both thermally and by the damage cascades induced by fission fragments (irradiation-enhanced diffusion). Above 1400°C, intrinsic diffusion via thermally created vacancies is predominant.¹⁵⁶

Results from atomistic modeling of the mechanisms for fission gas atom diffusion in these different regimes were reviewed in Refs. 151,152. Atomistic modeling efforts have shed light on the underlying atomic processes of intrinsic diffusion. Regardless of the number of bound oxygen vacancies, a second uranium vacancy strongly binds at the first nearest neighbor site creating a Xe-2V_U cluster.¹⁵⁷ The barrier for the Xe (Kr) to move between the two U sites is low and in some cases the atom even occupies the central position of the cluster, i.e., in between the two constituent U vacancies. The rate-limiting step for Xe diffusion is migration of one of the vacancies to another next-nearest neighbor position, which can either occur by a direct migration jump or by traversing over a second nearest neighbor position.^{155,157} A similar mechanism has been identified for Kr.¹⁵⁸ In the intermediate temperature range, the annealing of radiation damage is not complete, and the increased concentration of point defects results in irradiation-enhanced diffusion. In the lower temperature range, gas atom diffusion is athermal and driven directly by irradiation damage processes.

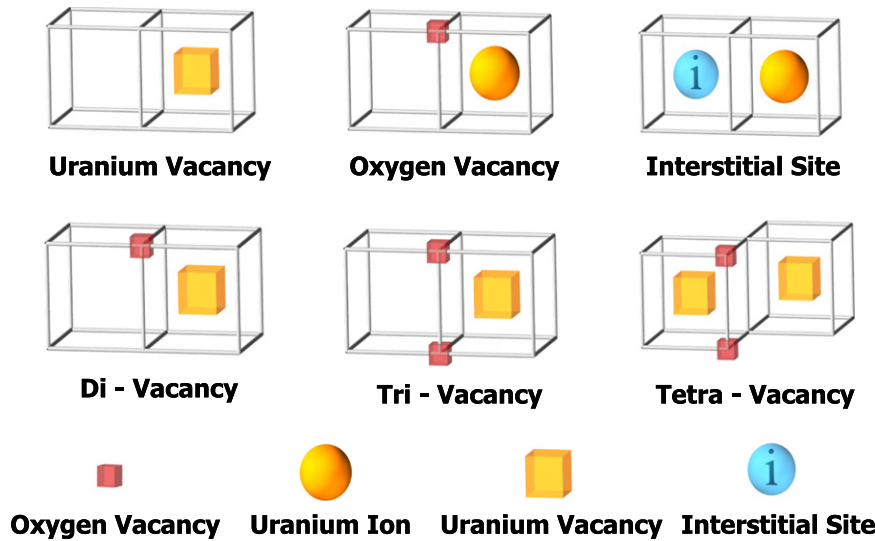


Fig. 12 Possible solution sites for fission products in UO_{2+x} according to Grimes. Reproduced from Grimes, R.W., 1991. Simulating the behaviour of inert gases in UO_2 . In: *Fundamental Aspects of Inert Gases in Solids*, 279. Plenum Press. p. 415.

The three temperature regimes defined above are reflected in the three components of the single gas atom diffusion coefficient often applied in fission gas behavior models^{159,160}

$$D = D_1 + D_2 + D_3$$

where

$$D_1 = 7.6 \cdot 10^{-6} \exp\left(-\frac{35000}{T}\right)$$

$$D_2 = 5.6 \cdot 10^{-25} \cdot \sqrt{\dot{F}} \exp\left(-\frac{13800}{T}\right)$$

$$D_3 = 8 \cdot 10^{-40} \cdot \dot{F}$$

where D is the diffusion coefficient (m^2/s), \dot{F} the fission rate density (fissions/ m^3s) and T is the absolute temperature (K). The scatter in the available experimental data for the diffusion coefficient is significant and correspondingly, a large uncertainty is associated with this parameter in fission gas behavior models.¹⁵⁶

2.13.2.3.1.3 Trapping

In nuclear fuels, either natural (e.g., impurities, dislocation lines, closed pores, etc.) or irradiation-induced imperfections in the solid (e.g., vacancy clusters along fission fragment tracks, fission gas bubbles, solid fission product precipitates) depress the amount of fission products available for diffusion by temporarily or permanently trapping the migrating atoms. Experiments show that for burnup levels characteristic of power reactors, fission gas atom trapping due to (intra-granular) fission gas bubbles is predominant relative to trapping due to other defects. The trapping rate depends on the number density and size of the intra-granular bubbles, hence, on temperature, fission rate and burnup.

2.13.2.3.1.4 Intra-granular bubble evolution

Experimental evidence of intra-granular bubbles, obtained using transmission electron microscopy (TEM), has been reported in numerous references, including the initial works of Turnbull,¹⁶¹ Cornell,¹⁶² and Baker¹⁶³ and the more recent work of Kashibe *et al.*¹⁶⁴ Typically, for fuel irradiated under LWR normal operating conditions, intra-granular bubbles have diameters of one to a few nm, with a narrow size distribution, and number densities of 10^{23} – 10^{24} m^{-3} . With increasing temperature and burnup, the average bubble size increases and the bubble number density decreases slightly. Three fundamental processes control the evolution of intra-granular bubbles: bubble nucleation, gas atom trapping at the bubbles, and irradiation-induced gas atom resolution from the bubbles back into the lattice.

Following the terminology of Olander and Wongsawaeng,¹⁶⁵ one can distinguish between heterogeneous and homogeneous nucleation. The former refers to the nuclei of the new bubbles being created as a direct consequence of the interaction of fission fragments with the lattice,¹⁶¹ whereas the homogeneous mechanism corresponds to diffusion-controlled interactions of individual gas atoms leading to the formation of dimers.^{98,166,167} Based on the evidence from TEM observations showing intra-granular bubbles lying in straight lines, Turnbull¹⁶¹ proposed that bubbles are nucleated heterogeneously in the wake of fission fragments. Indeed, not all TEM images show aligned bubbles. Nevertheless, it should be considered that the typical thickness of TEM samples is lower than the fission fragment range, therefore, only portions of actual fission tracks are observed. There is no obvious reason to

exclude the activation of either mechanism, but it is generally considered that the heterogeneous mechanism dominates in pile in oxide fuel.^{161,163,168}

Under irradiation, a fraction of the gas atoms trapped in bubbles is continually re-dissolved in the surrounding matrix through the interaction of fission fragments with the bubbles. Two different types of mechanisms have been proposed for resolution. As defined in Ref. 165, heterogeneous resolution refers to en-bloc destruction of the entire intra-granular bubble by the thermal spike induced by the fission fragment passing through or near the bubble, while the homogeneous mechanism consists of resolution of one gas atom at a time when interacting with a fission fragment or an energetic atom from the collision cascade. Macroscopic models generally adopt expressions for the resolution rate based on the assumption of complete bubble destruction, but there is still discussion about the dominating mechanism. Recent molecular dynamics studies^{169,170} supported the notion that the thermal spike induced by the fission fragment is the rate-controlling process for resolution, which corresponds to the heterogeneous mechanism. However, these studies also indicated that an upper limit to the number of atoms brought in resolution exists, implying that from a certain size up, bubbles are not fully destroyed.

As mentioned above, intra-granular bubbles affect the rate of gas transport to grain boundaries, as they act as traps for diffusing individual fission gas atoms. Also, intra-granular bubbles and dissolved fission gas contribute to fuel swelling, although intra-granular gaseous swelling becomes significant compared to inter-granular swelling only at high burnup or during transients to high temperatures. In particular, at higher burnup and/or temperature, a second bubble population is created, which is characterized by bubble sizes up to hundreds of nm and number densities around or below 10^{21} m^{-3} . This phenomenon is referred to as intra-granular bubble coarsening and can result in significant fuel gaseous swelling.^{164,171} Coarsened bubbles appear to be associated with dislocations.¹⁷¹ However, the underlying mechanisms for bubble coarsening have not been fully clarified yet.

Migration of intra-granular fission gas bubbles provides an additional mechanism to the sequence “bubble formation-resolution-gas atom diffusion” to interpret fission product release from nuclear fuels. Under normal operating conditions, however, intra-granular fission gas bubbles show a small mobility at least up to 1500–1800°C.^{172–174} This is partly explained by the pinning by dislocations and other crystal defects. Bubble motion is expected to play a role in gas diffusion only under power transient and high temperature conditions. The mechanism by which migration occurs depends on the bubble size, and changes from surface diffusion to volume diffusion and to evaporation/condensation with increasing bubble size.

2.13.2.3.1.5 Grain growth and grain boundary sweeping

In LWR fuel, temperature-dependent grain growth is observed, i.e., large grains grow at the expense of smaller ones. Grain growth affects fission gas release in two ways. First, grain boundary sweeping provides an additional mechanism for the collection of gas at grain boundaries, from which release to the exterior of the fuel pellet can occur. The collection results from the low solubility of the fission gas, hence the moving grain boundary does not redeposit any gas in the newly formed crystal behind it, acting as a fission gas-collecting filter. At the same time, grain boundary bubbles hinder grain growth to some extent. Second, grain growth corresponds to an increase of the average diffusion distance for the fission products created in the grain. Unlike the first consequence, this tends to reduce the release rate.

2.13.2.3.1.6 Grain boundary diffusion

Grain boundary diffusion is the most commonly observed route for solute migration in polycrystalline materials. It is generally accepted that diffusion in crystalline solids proceeds more rapidly along grain boundaries than through the lattice. This is due to the atomic jump frequency in these planar defects, which is about 10^6 times greater than the jump frequency of regular lattice atoms in stoichiometric materials at 0.6 times the absolute melting temperature. Nevertheless, it is generally recognized that the dominant FGR mechanism in oxide nuclear fuel is grain boundary bubble network evolution as opposed to grain boundary diffusion. Olander and Van Uffelen¹⁷⁵ assessed the migration distance of a Xe atom in a grain boundary containing a population of traps with characteristics that roughly encompass the grain boundary bubble populations observed in irradiated UO_2 fuel. Their finding that gas atoms will be trapped after a migration distance equal to the size of a grain or less provided a theoretical justification to consider grain boundary diffusion to only contribute to the precipitation of fission gas atoms in grain boundary bubbles, rather than to the long-range transport to the free surface of the pellets.¹⁷⁵

2.13.2.3.1.7 Grain-face bubble evolution

Fission gas that reaches the grain boundaries tends to precipitate into lenticular bubbles at the grain faces. Grain-face bubbles in irradiated oxide fuel have been observed using scanning electron microscopy (SEM), e.g., 171,176,177. The evolution of grain-face bubbles results in fuel gaseous swelling and in the release of gas to grain edges, which ultimately leads to fission gas release through grain edge tunnels (cf. below). The processes that govern grain-face bubble evolution were discussed in Ref. 176 and include (a) nucleation, (b) growth through collection of gas atoms and vacancies, (c) bubble coalescence and adjustment of bubble morphology by capillarity forces, and (d) bubble connection with grain edges. In Fig. 13, SEM images of grain-face bubbles in UO_2 fuel at different irradiation times and conditions are shown.¹⁷⁶ Grain-face bubbles formed as isolated progressively interlink to create elongated bubbles in the advanced state of development, connecting most of the grain face with the grain edge bubbles that mediate the final venting of fission gases. SEM micrographs in Fig. 14 also show grain-face bubbles in ramp-tested UO_2 fuel.¹⁷⁷ In this case, it can be seen that in spite of the high grain-face bubble coverage, a significant fraction of the bubbles still appear isolated.

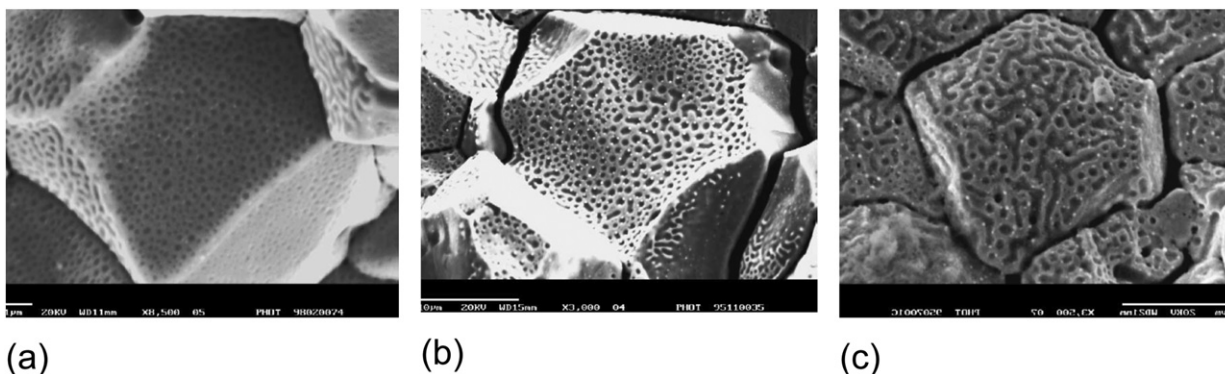


Fig. 13 SEM micrographs showing the evolution of grain-face bubbles in irradiated UO_2 . (a) Early stage at a burnup of 13 GWd/tU. The fuel was fast ramped and held at 1700°C for 2 min. The mean projected bubble radius is 85 nm, there are approximately 9 bubbles μm^{-2} of boundary and the fractional bubble coverage is 24%. (b) Intermediate stage evolution at 21 GWd/tU. The fuel was fast-ramped and held at 1800°C for 2 min. The mean projected radius is 220 nm, there are 1.3 bubbles μm^{-2} and the fractional coverage is 29%. (c) Advanced stage evolution. The fuel was ramped under similar conditions but maintained at 1800°C for 30 min. The mean projected radius is 260 nm, the mean projected length is 1340 nm, there are 0.43 bubbles μm^{-2} and the fractional coverage is 44%. Approximately 40% of the bubbles are connected to the grain edges. Reproduced from White, R.J., 2004. The development of grain-face porosity in irradiated oxide fuel. *J. Nucl. Mater.* 325, 61.

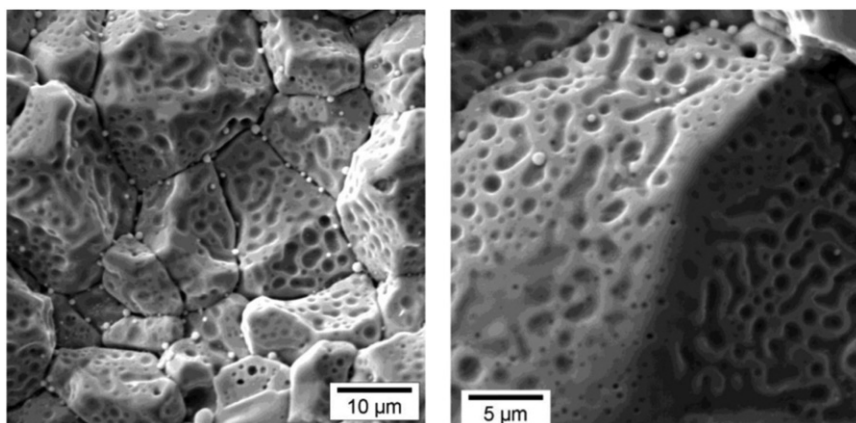


Fig. 14 SEM micrographs showing grain-face bubbles in ramp-tested UO_2 fuel. Fuel was irradiated to a burnup of 38.8 MWd/kg UO_2 and ramp tested to a ramp terminal power of 52 kW/m, with a hold time of 90 s. The fractional bubble coverage is higher than 45%. Reproduced from Noirot, J., Gonner, C., Desgranges, L., Pontillon, Y., Lamontagne, J., 2006. LWR fuel gas characterization at CEA Cadarache LECA-STAR hot laboratory. In: *Proceedings of the Technical Committee Meeting on Post-Irradiation Examination and In-Pile Measurement Techniques for Water Reactor Fuels*, TECDOC-1635, Part I, p. 129. Buenos Aires, Argentina: IAEA.

Note that these examples refer to fuel that was subject to significantly higher temperatures than typical fuel temperatures during normal operating LWR conditions, and such levels of grain-face bubble growth and coverage are not expected in fuel irradiated under normal operating conditions, at least up to moderate burnups.

2.13.2.3.1.8 Grain-edge tunnel formation and thermal fission gas release

The third and last stage of thermal FGR in oxide fuel refers to the development of gas bubbles along grain boundary triple junctions (grain edges), which eventually form a continuous network of porosity extending to the fuel outer surface and providing a route for gas venting to the fuel rod free volume. This interpretation relies on experimental observations of irradiated fuel showing populations of lenticular gas bubbles occupying the grain faces and tunnel-like, interconnected pores along the grain edges, often open to the exterior of the fuel sample, e.g., Ref. 178.

The behavior of grain-edge bubbles is important both because when they eventually interlink, they provide a path for fission gas atoms to be released from the fuel and because they can account for a significant portion of fuel gaseous swelling. Experiments showed that at low burnup the contributions of grain-face and grain-edge bubbles to the overall swelling are about equal, but as irradiation proceeds, the contribution due to grain-edge bubbles exceeds that due to grain-face bubbles.¹⁷⁸ In contrast with lenticular bubbles at grain faces, bubbles at grain edges take an energetically more favorable cigar shape with a center axis along the grain edge. Grain-edge tunnels are formed through the coalescence of multiple cigar shaped grain-edge bubbles. Bubble interconnection is a reversible process, for the tunnel network can close again under the influence of the surface tension when the

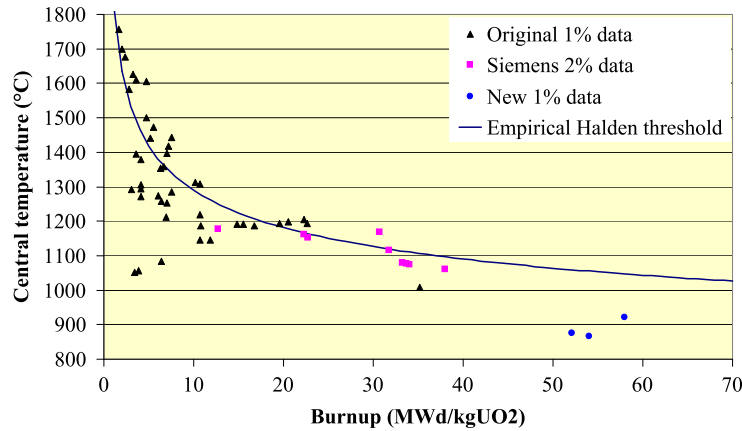


Fig. 15 Original Halden (or Vitanza) criterion for the onset of fission gas release and supporting data. Reproduced from Vitanza, C., Graziani, U., Fordestrommen, N.T., Vilpponen, K.O., 1978. Fission gas release from in-pile measurements. In: Proceedings of the Enlarged Halden Programme Group Meeting, HPR-221.10, November, 1978, Paper 38. Loen, Norway: OECD Halden Reactor Project. Vitanza, C., Kolstad, E., Graziani, C. Fission gas release from UO_2 pellet at high burnup. In: Proceedings of the Topical Meeting on Light Water Reactor Fuel Performance, May. Portland, OR: American Nuclear Society.

outgoing flux of gas atoms associated with FGR outweighs their supply. However, when the volume swelling caused by the tunnels is sufficiently large, the tunnel network becomes stable and remains open. Note that it has been pointed out¹⁵⁰ that, due to the more favorable bubble nucleation conditions at edges in comparison with faces,¹⁷⁹ the sequence of events may differ.

Based on a wide range of data gathered at the Halden Reactor, Vitanza *et al.*^{180,181} determined an empirical relationship between the average fuel rod burnup and the fuel centreline temperature, which separates rods characterized by FGR lower and higher than 1%. The study showed that significant FGR occurs only after an incubation burnup has been attained. Physically, this incubation period is associated with the onset of interconnected grain-edge tunnels open to the fuel free surface. The relationship defines the so-called Halden or Vitanza threshold for 1% integral fuel rod FGR^{180,181}:

$$T_c(^{\circ}\text{C}) = \frac{9800}{\ln\left(\frac{bu}{0.005}\right)}$$

where T_c represents the fuel central temperature in degrees Celsius, and bu the burnup in MWd/kgUO_2 . The Vitanza threshold is illustrated in Fig. 15.

In addition to the behavior reviewed above, enhanced FGR has been observed during transients and at high burnup, which indicates that additional mechanisms may be operational in such specific situations. In particular, during transients, both rapid increases and decreases in temperature have resulted in substantial fission gas release occurring on a small time scale (burst release). The rapid kinetics of the process suggests a non-diffusional mechanism of gas release from the grain boundaries through grain-boundary separation due to micro-cracking. Specifically, grain-boundary separation has been observed following experiments simulating RIA conditions.^{182,183} Additional discussion on transient FGR is found in Refs. 184,185. At high burnup above 50 MWd/kgHM , an acceleration of fission gas release has been observed. A definitive interpretation for the underlying mechanism of this acceleration has not been given yet, and it is unclear whether the role of the high-burnup structure (Section 2.13.4.2) in fission gas behavior and in affecting the fuel thermal conductivity can explain the observations. An extensive discussion on this issue is found in Ref. 152.

2.13.2.3.2 Modeling fission gas behavior in engineering fuel analysis

In order to compute the amount of gaseous swelling and FGR in fuel rod thermo-mechanics calculations, models of fission gas behavior need to be incorporated in engineering fuel performance codes. Various approaches to modeling fission gas release and swelling exist, which can be classified in two broad categories. On one hand, there are purely empirical models, including those based on soft computing techniques such as neural networks. These models are inexpensive to use and provide efficient tools for the design of fuel rods within the range of conditions covered by the data used to derive the correlations. However, empirical models are not suitable for gaining knowledge about the underlying mechanisms, nor can they be extrapolated beyond their range of application. On the other hand, there are mechanistic models which aim at the physical description of the underlying phenomena. Despite the need for substantial validation, such models provide an excellent basis, both for the improved understanding of the mechanisms, as well as for the application to an extended range of conditions relative to empirical models. The tendency for fuel performance codes nowadays is to increasingly adopt mechanistic models.^{150,186,187}

Models generally consider fission gas behavior as comprised of two stages. The first stage corresponds to the gas behavior in the grains (intra-granular part), while the second stage corresponds to the gas behavior at the grain boundaries (intergranular part).

2.13.2.3.2.1 Intra-granular behavior

For the behavior in the fuel grains, the following scenario is generally adopted. The gas atoms are created by fission in the fuel matrix. They then diffuse towards the grain boundaries by diffusion mediated by interactions with intra-granular bubbles. The bubbles act as sinks for gas atoms, thereby reducing the amount of gas available for release.

This scenario leads to solving a diffusion equation in a sphere with a source term proportional to the local fission rate density ($S = Y_{fp}\dot{F}$). In the pioneering work of Booth,¹⁸⁸ the equivalent sphere model was proposed. This theory considers a polycrystalline sinter as a collection of uniform spheres with an equivalent radius in order to simplify the mathematical problem. The hypothetical sphere radius (R_B) is defined so that the effective surface-to-volume ratio of the fuel (S/V) is preserved:

$$R_B = 3 \left(\frac{V}{S} \right)_t$$

where $(S/V)_t$ accounts for the sum of the geometric surface of the pellets as well as the surface due to open porosity. As irradiation proceeds, fission gases are generated within the Booth sphere and migrate to the surface, where the concentration is taken to be zero. The corresponding diffusion equation is

$$\frac{\partial c}{\partial t} = D \nabla^2 c + S$$

where c is the concentration of gas in the sphere, t the time and D the diffusion coefficient of gas atoms. Booth proposed that the fractions of stable gas release can be approximated by

$$f_{ann}(t) \cong 6 \sqrt{\frac{Dt}{\pi R_{gr}^2}} - 3 \frac{Dt}{R_{gr}^2}$$

for so-called annealing conditions (i.e., without source term, but with an initial non-zero concentration of gas atoms), and

$$f_{irr}(t) \cong 4 \sqrt{\frac{Dt}{\pi R_{gr}^2}} - \frac{3}{2} \frac{Dt}{R_{gr}^2}$$

for irradiation conditions (non-zero source term and zero initial concentration). In a second model he proposed the approximation for the release-to-birth ratio for unstable gas release under steady-state conditions¹⁸⁹:

$$\frac{R}{B} = \frac{3}{R_{grain}} \sqrt{\frac{D}{\lambda}} \left[\coth \left(R_{grain} \sqrt{\frac{\lambda}{D}} \right) - \frac{1}{R_{grain}} \sqrt{\frac{D}{\lambda}} \right]$$

where λ represents the decay constant of the species under consideration. It should be noted that the diffusion coefficient to be used is subject to a large uncertainty of up to 2 orders of magnitude.¹⁵⁶ The expression in Section 2.13.2.3.1 is often used.

Regardless of the uncertainty on the diffusion coefficient, the Booth model itself suffers several limitations as it

- (1) Does not allow for considering the inter-granular stage of FGR explicitly
- (2) Considers constant temperature and fission rate density
- (3) Does not account for resolution and trapping at intra-granular bubbles
- (4) Does not account for grain growth and grain boundary sweeping
- (5) Cannot reproduce an incubation period of FGR
- (6) Does not account for resolution from inter-granular bubbles

All of these limitations have been alleviated over time. First, the diffusion problem is solved locally considering a sphere of radius equal to the local average grain radius, rather than for the equivalent sphere. This allows for considering the inter-granular stage of FGR explicitly (see below). As regards the second limitation, several numerical techniques have been proposed to solve the diffusion equation in time-varying conditions, which have been compared in Refs. 190,191. In order to account for the effect of intra-granular bubbles, one should solve an equation for the single gas atoms diffusing towards the sphere boundary, as in Booth's model, plus a second equation that governs the balance of gas atoms trapped in bubbles, i.e., Ref. 192,

$$\begin{aligned} \frac{\partial c}{\partial t} &= D \nabla^2 c - gc + bm + S \\ \frac{\partial m}{\partial t} &= +gc - bm \end{aligned}$$

where m is the concentration of gas atoms residing in intra-granular bubbles, $g = 4\pi R_{bubble}D$ the trapping rate of gas atoms at bubbles, and b the rate of irradiation-induced gas atom resolution from bubbles back into the lattice. Speight¹⁹² derived the analytic modal solution of this system of equations in spherical geometry for constant conditions and with zero initial conditions for c and m . He then simplified the solution assuming that trapping and resolution are in equilibrium, based on the observation that the number density and size of the intra-granular bubbles saturate early in the irradiation. He showed that the fractional gas release to the grain boundaries under these assumptions is analogous to the expression derived

previously by Booth for diffusion in the absence of trapping/resolution, but with the gas atom diffusion coefficient, D , substituted by an effective diffusion coefficient,

$$D_{eff} = D \frac{b}{b+g}$$

As a result, the numerical techniques developed to solve the diffusion in a sphere with varying conditions can still be used in fuel performance codes, albeit with a modified diffusion coefficient. Currently, new numerical methods are being developed to facilitate the solution of the general system of coupled differential equations and overcome the concept of an effective diffusion coefficient. This is especially important for the analysis of rapid transients to relatively high temperatures such as postulated reactivity-initiated accidents (RIA), where the assumption of equilibrium between trapping and resolution may be inadequate.¹⁹³

Models generally introduce a simple resolution rate coefficient that is proportional to the local fission rate density and depends on the bubble size, based on the heterogeneous resolution mechanism, i.e., Ref. 194

$$b = 2\pi(R_{bl} + \delta)^2 \mu_{ff} \dot{F}$$

where it is assumed that a bubble can be destroyed if its center lies within a distance δ from the fission fragment track of length μ_{ff} .¹⁹⁵

To evaluate the trapping and resolution parameters, and the intra-granular gaseous swelling, the bubble number density and average bubble size need to be calculated using dedicated models. The traditional approach adopted in engineering fuel performance codes describes the evolution of intra-granular fission gas bubbles using empirical correlations for the mean bubble size and number density as a function of macroscopic parameters, e.g., the local temperature.^{195,196} On the opposite side, a complete and rigorous description of bubble evolution, including the evolution of the size distribution, can be accomplished by employing cluster dynamics models, e.g., Ref. 197. However, these advanced modeling approaches are computationally intensive and cannot be used directly for fuel performance code applications. Physically based models that represent the bubble size distribution as only the mean size and the total number density (single-size models¹⁶⁵) represent a suitable compromise and have been applied in engineering fuel performance codes.^{198,199}

In order to account for the effect of grain growth, the intra-granular diffusion problem is generally solved in a sphere whose radius evolves over time (e.g. Refs. 91,200). However, it must be pointed out that various grain growth models exist, even though the Ainscough²⁰¹ model is often applied:

$$\frac{dR_{gr}}{dt} = k \left(\frac{1}{R_{gr}} - \frac{1}{R_{max}} \right)$$

where k is a temperature-dependent rate constant, R_{gr} the grain radius and $R_{max} = R_{max}(bu)$ a limiting grain size. This burnup-dependent quantity is introduced in order to account for the retarding effect of fission products on grain growth as burnup proceeds.

The grain boundary sweeping effect is generally accounted for by assuming that the fraction of intra-granular gas transferred to the grain boundaries through grain boundary sweeping equals the fraction of grain volume swept by the moving boundaries during grain growth.

For alleviating the other limitations of the Booth models, an inter-granular module has to be introduced.

2.13.2.3.2.2 Inter-granular behavior

One generally observes a period of time at the beginning of irradiation during which the integral release in a fuel rod is negligible. This incubation period has been related to the burnup required to saturate the grain boundaries with inter-granular bubbles. To this end, while grain boundary saturation has been observed following ramp tests (e.g., Fig. 13), experimental evidence of grain boundary saturation during base irradiation is less conclusive. Clearly, the concept of saturation represents an approximation, as the actual behavior involves a continuous increase of the fraction of inter-granular bubbles connected to the fuel exterior as the irradiation proceeds, rather than a discrete saturation threshold. Irrespective of this, it is commonly accepted that the rate of FGR is related not only to the intra-granular diffusion rate of gas, but also to the inter-granular processes. As a result, it becomes necessary to model the inter-granular behavior of the fission gas atoms in conjunction with the Booth model.

There are various approaches to describe the behavior of fission gas on the grain boundaries. Traditional models applied in fuel performance codes do not describe the kinetics of bubbles at the grain boundaries directly. Rather, in order to represent the establishment of an open tunnel network along the grain boundaries as the condition for the onset of FGR, a saturation value for the inter-granular gas atom concentration is considered. A well-known example of a model in this category is the Forsberg-Massih model.²⁰² In order to derive the saturation gas atom concentration, the following assumption have been made

- (1) All inter-granular bubbles have, at any instant, equal size and equal lenticular shape of circular projection, with θ being the semi-dihedral angle between the grain boundary and the bubble surface (cf. Fig. 16).
- (2) A mechanical equilibrium exists between the gas pressure in the bubble (p), the surface tension force and the hydrostatic stress in the surrounding matrix, i.e., $p = p_{eq} = \frac{2\gamma}{r} + \sigma_h$, where p_{eq} is the equilibrium pressure, γ the UO_2 /gas specific surface energy, r the radius of curvature of the bubble and σ_h the hydrostatic stress (positive if the solid medium is under compression).
- (3) The perfect gas law can be applied as equation of state for the gas in the bubbles.

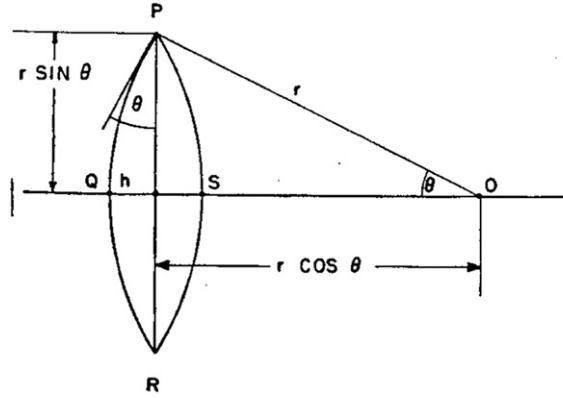


Fig. 16 Schematic representation of a lenticular grain face bubble with radius of curvature r .

Under these assumptions, the following expression is obtained for the inter-granular gas atom concentration at saturation²⁰²:

$$N_{sat} = \frac{4rf(\theta)}{3kT\sin^2\theta} F_{sat} \left(\frac{2\gamma}{r} + \sigma_h \right)$$

where N_{sat} is the saturation concentration per unit grain-boundary surface, k is the Boltzmann constant, $f(\theta) = 1 - 1.5\cos\theta + 0.5\cos^3\theta$ a geometric factor and F_{sat} the fraction of the grain face surface occupied by the bubbles (fractional coverage) at saturation. As soon as N_{sat} is achieved, any excess gas atoms arriving at the grain boundaries are deemed released. The Forsberg-Massih model for inter-granular fission gas behavior has been applied in several fuel performance codes, including FRAPCON,⁵⁸ FALCON,⁶² and BISON.⁶⁵ A similar concept has been applied in the TRANSURANUS code,¹¹² however, in this case the saturation concentration was derived based on the Vitanza threshold (cf. Section 2.13.2.3.1).

In reference to the above hypotheses, it is noted that in general inter-granular bubbles are not at mechanical equilibrium and in particular, they tend to be over-pressurised.^{176,203} Also, the density of the gas in the bubbles is in general higher than that for which the perfect gas law can be applied.²⁰⁴ In addition to this, historically, in the majority of models the hydrostatic stress has been neglected, or a constant and uniform value has been used, or the external pressure of the fuel pellet has been considered rather than the local stress.¹¹³ However, exceptions exist, including the FEMAXI fission gas model,⁹¹ the MARGARET model implemented in the ALCYONE code,¹⁸⁸ and the mechanistic fission gas model available in the TRANSURANUS code.¹⁹⁷

Furthermore, in the modeling approach described above, consideration of inter-granular fission gas behavior is limited to estimating the saturation concentration of gas atoms for the calculation of FGR, and fuel swelling associated with gas bubbles (both intra- and inter-granular) is left to separate models. In particular, semi-empirical relations are being used for the gaseous swelling as a function of the temperature and burnup (e.g., MATPRO correlation²⁰⁵), or as an empirical function of the released fraction, for instance²⁰⁶:

$$\left(\frac{\Delta V}{V} \right)_{gaseousFP} = A(1 - \alpha_{FG} FGR - \alpha_{Cs} CSR)bu$$

where A is a constant for solid swelling, FGR the local fractional fission gas release from the fuel, CSR the fractional release of the volatile fission products (Cs, I) from the fuel, bu the local fuel burnup, $\alpha_{FG} = 0.37$ and $\alpha_{Cs} = 0.45$.

Because gaseous swelling and FGR are inherently coupled, in a more physically sound approach the kinetics of inter-granular bubbles is considered explicitly. This feature is included in a second category of models. The first model mentioned in this respect was proposed by White and Tucker.¹⁹⁶ They considered two parallel processes for release from the Booth sphere: intra-granular diffusion and diffusion through tunnels along grain boundaries. To this end they solved two different diffusion equations in the equivalent Booth sphere. More recently, Koo *et al.*²⁰⁷ proposed two different contributions for the S/V used to compute the equivalent Booth sphere radius. One contribution was attributed to macroscopic radial cracks in the pellet periphery, while the second contribution was ascribed to a fraction of the tunnel network along grain boundaries that was in contact with the open grain-edge porosity (based on percolation theory in two dimensions). Several other models have been proposed whereby the gas transport through the open tunnel network is being modeled according to Darcy's or Poiseuille's law in a tube (e.g.,^{150,208}). More recently, White¹⁷⁶ went further with the details and modeled bubble coalescence using a geometrical reasoning for the rate of bubble impingement during growth, as well as bubble morphological relaxation through differential surface-curvature driven absorption/emission of vacancies. Also, White considered non-equilibrium bubbles, with the kinetics of bubble growth being also governed by absorption/emission of vacancies driven by the difference between the gas pressure in the bubbles and the mechanical equilibrium pressure. This is a more general approach relative to consideration of bubbles being always at mechanical equilibrium, and has also been considered by Veshchunov.¹⁶⁶

A model that is currently available in multiple fuel performance codes and considers the kinetics of inter-granular bubbles explicitly is the fission gas swelling and release model developed recently in Refs. 198,209. This model is based on the general approach of White¹⁷⁶ for the kinetics of non-equilibrium lenticular bubbles at the grain faces, although without consideration of

departure from the circular shape and morphological relaxation for the sake of simplicity. In particular, bubble growth (or shrinkage) by inflow of gas atoms from within the grains and concomitant absorption (or emission) of vacancies by non-equilibrium bubbles is considered. The bubble growth/shrinkage rate is calculated as

$$\frac{dV_{bl}}{dt} = \omega \frac{dn_g}{dt} + \Omega \frac{dn_v}{dt}$$

where V_{bl} is the average bubble volume, ω the Van der Waals covolume of a fission gas atom, n_g the number of fission gas atoms per bubble, Ω the vacancy volume in the bubble, and n_v the number of vacancies per bubble (additional to vacancies occupied by gas atoms). The arrival rate of gas atoms at inter-granular bubbles is based on the solution of the intra-granular diffusion equation (see above), with the absorption rate of gas at bubbles being assumed to equal the arrival rate of gas at the grain boundaries. The absorption/emission rate of vacancies at bubbles is based on the Speight and Beere model²¹⁰:

$$\frac{dn_v}{dt} = \frac{2\pi D_{gb} \delta_{gb}}{kTS} (p - p_{eq})$$

where D_{gb} is the vacancy diffusion coefficient along grain boundaries, δ_{gb} the thickness of the diffusion layer in grain boundaries, k the Boltzmann constant, T the temperature, and S a parameter that depends on the fractional coverage as detailed in Ref. 176. The mechanical equilibrium pressure, p_{eq} , is given by the sum of the bubble surface tension force and the hydrostatic stress in the surrounding medium. The pressure of the gas in the bubble, p , is calculated based on the Van der Waals equation of state as

$$p = \frac{kT n_g}{\Omega n_v}$$

Bubble coalescence is accounted for according to a geometrical reasoning for the rate of bubble impingement during growth, as detailed in Refs. 174,197. The volumetric gaseous swelling due to inter-granular bubbles is calculated as

$$\left. \frac{\Delta V}{V} \right|_{gas,inter} = \frac{1}{2} \frac{3}{R_{gr}} N_{bl} V_{bl}$$

where V is the fuel volume and N_{bl} the number density of bubbles per unit grain boundary surface. Fission gas release is modeled representing bubble interconnection through a saturation limit for the fraction of the grain boundary surface occupied by bubbles. More precisely, after the fractional coverage reaches a saturation value, further bubble growth is compensated by gas release in order to maintain the constant coverage condition:

$$\frac{dF_c}{dt} = \frac{d(N_{bl} A_{bl})}{dt} = 0 \text{ if } F_c = F_{sat}$$

where F_c is the fractional coverage and A_{bl} the average bubble projected area on the grain boundary. This representation allows for the incubation behavior of FGR. The above model introduces a consistent coupling between FGR and swelling, as fission gas release counteracts bubble growth and thereby gaseous swelling. This model has been implemented in the TRANSURANUS code.^{198,209} Later, a similar model has been implemented in the BISON code.¹⁵⁶

Note that in all inter-granular gas behavior models mentioned so far, no explicit distinction between gas behavior at grain faces and grain edges is made. Rather, an effective representation for the overall gas behavior at grain boundaries is considered. This simplification is partly related to the commonly adopted assumption of spherical grains, and may be justified in view of the large uncertainties pertaining to many of the important parameters in fission gas behavior models. There are a few exceptions, such as the model of White and Tucker²¹¹ which was implemented in the ENIGMA code,⁵⁵ or the model of Koo *et al.*,^{207,212} who considered grains to be tetradecahedrons and included a description of torus-shaped grain-edge bubbles in this configuration. This model was incorporated in the fuel performance code COSMOS.²¹² The model from,¹⁷⁶ which is implemented in the MFPR code, also includes a specific description of grain-edge bubble evolution.

In a third category of models, a comprehensive set of mechanisms (cf. Section 2.13.2.3.1) is considered in the form of a set of ordinary differential equations, i.e., equations for intra- and inter-granular behavior are solved simultaneously. Examples include the MARGARET model¹⁸⁷ implemented in the fuel performance code ALCYONE, the FASTGRASS model of Rest¹⁶⁷ in the VICTORIA code,²¹³ and the detailed fission gas behavior model coupled to the FALCON code from.²¹⁴

2.13.2.3.2.3 Coupling intra- and inter-granular behavior

In general, the intra-granular and inter-granular modules of a fission gas behavior model are coupled in two directions. On one hand, the intra-granular module provides the source term for the inter-granular module. On the other hand, the inter-granular module provides the boundary condition for the diffusion equation in the spherical grains and/or a supplementary source term associated with resolution of gas from inter-granular bubbles. In fact, most models for intra-granular diffusion assume a boundary condition of zero gas concentration at the grain boundary, meaning that the grain boundary is considered to be a perfect sink. In order to account for the resolution effect from grain boundary bubbles, three different approaches are being utilized. The first approach considers a correction factor for the Booth flux, accounting for the fact that resolution opposes gas diffusion out of the grains. The second approach considers applies a time-varying boundary condition that makes use of a time-dependent flux

balance. In the third approach, a supplementary source term of gas in the grain is defined in a fine layer adjacent to the grain face, either as a uniform source in a fine layer, or as a Dirac distribution at a given distance from the grain boundary.

2.13.3 Design Basis Accident Modeling

Fuel designers and safety authorities rely heavily on fuel performance codes since they require minimal costs in comparison with the costs of an experiment or an unexpected fuel rod failure. Nevertheless, two types of fuel performance codes are generally being applied, corresponding to normal operating and design basis accident conditions, respectively. In order to simplify the code management by limiting the number of programs and in order to take advantage of the hardware improvements, there is a tendency to generate a single fuel performance code that can cope with the different conditions, which requires different types of developments.

On the one hand, extending the application range of a fuel performance code originally developed for steady-state conditions to accident conditions requires modifications to the basic equations in the thermal-mechanical description of the fuel rod behavior,⁷³ stable numerical algorithms and a proper time-step control, in addition to the implementation of specific models dealing with the high temperature behavior of cladding such as observed under LOCA conditions.²¹⁵ For dealing with RIA events, one should check carefully the thermal expansion model because of the edge-peaked power distribution, as well as the other models affecting the effective cold gap width,²¹⁶ and the model for thermal heat transfer in the plenum (e.g., assessing also the effect of gamma heating on the average plenum temperature distribution^{217–219}). On the other hand, for fuel performance codes developed to simulate various aspects of the nuclear fuel behavior under accident conditions, such as TESPA,²²⁰ MFPR,²²¹ FRAPTRAN,²²² SCANAIR,²²³ FALCON⁶³ or RANNS,³⁸ either the thermo-mechanical behavior of the fuel must be incorporated and/or the extension of models to normal operating conditions is necessary to consider burnup dependent phenomena such as thermal conductivity degradation, fission gas release, gap closure and swelling as well as cladding corrosion. Such a posteriori modifications of the fuel performance code may entail difficulties in terms of convergence and calculation time.

2.13.3.1 Loss of Coolant Accidents

2.13.3.1.1 Specific LOCA features

As reviewed by the NEA,²²⁴ a Loss Of Coolant Accident (LOCA) in a water cooled reactor consists of a large break of the coolant primary system and consequent loss of core cooling capacity. A LOCA is a design basis accident, i.e., one that the plant design must account and accommodate for in terms of ensuring that a core coolable configuration is maintained. Post-LOCA coolability is achieved by an immediate reactor scram, i.e., a rapid insertion of control rods in the core which ends the fission power production in the nuclear fuel, and by the activation of an Emergency Core Cooling Systems (ECCS) which enters into function upon depressurisation of the primary system, within relatively short time after the start of the transient.

As schematically shown in Fig. 17, a typical LOCA sequence in a PWR consists of three main phases. During the first phase depressurisation of the primary system occurs, which is accompanied by a reactor scram. In the course of this phase, the fuel

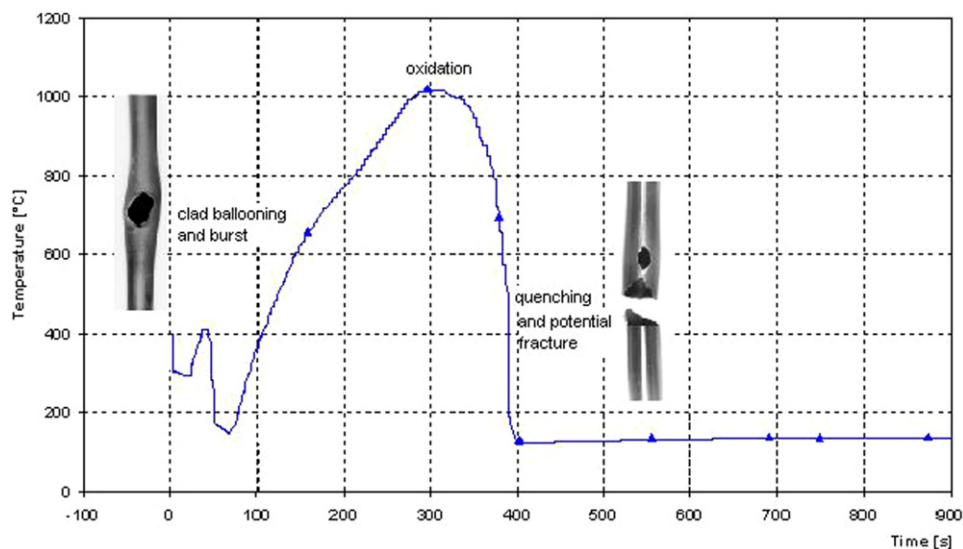


Fig. 17 Schematic evolution of a fuel rod during a loss of coolant accident. Reproduced from Maillat, A., Grandjean, C., Hache, G., 2001. IPSN proposal for high burnup fuel LOCA experimental programs. In: Proceedings of the Technical Committee Meeting on Fuel Behavior Under Transient and LOCA Conditions, TECDOC-1320, September 10–14, 2001, p. 279. Halden, Norway: IAEA.

temperature may oscillate depending on position, timing of the power reduction and timing of the depressurisation. The cladding temperature may even decrease since the water still has enough cooling capacity and because the water temperature is decreasing as pressure decreases.

In the second phase, the core heats up because of the remaining heat generation in the fuel (stored and decay heat) and the inadequate cooling associated with the loss of water. Normally, the fuel cladding temperature increases at a moderate rate, approximately a few degrees per second in the earlier phase of the temperature escalation. The Zircaloy cladding undergoes a crystallographic transition from the α phase to a β phase at temperatures exceeding about 800°C (cf. below), although the transition temperature is affected by the amount of hydrogen contained in the metal cladding as well as the heating rate. Crystallographic phase transition also affects the creep rate of Zircaloy. In fact, when the temperature exceeds about 600°C, the cladding becomes more and more prone to viscoplastic (creep) deformation and under the effect of the rod inner pressure – which is appreciably larger than in the depressurised reactor vessel – it starts deforming and ballooning in the space between the fuel assembly grid spacers. Ballooning may ultimately cause the fuel rod cladding to burst open, breaking the first barrier to radiation containment.

In the third phase, the cladding temperature continues to increase but at gradually lower rate due to the increasing radiant and convective heat transfer, exhibiting a relatively flat temperature trend for some period of time normally lasting for few minutes. Under the emergency core cooling systems (ECCS) effect, the cladding temperature trend is then reversed and after a period of gradual temperature decrease, the cladding is finally quenched by the ECCS water rising in the core.

2.13.3.1.2 Specific LOCA modeling requirements

The major concern from the fuel safety criteria viewpoint is the rapid cladding oxidation taking place when the cladding is heated up to high temperature and exposed to steam environment, as it occurs in a LOCA. In fact the safety criteria for LOCA have been reviewed by the NEA²²⁴ and are stated as 5 requirements (although small variations exist in each country) dealing with the calculated performance of the cooling system under the most severe loss-of-coolant accident conditions:

- (1) In order to preserve cladding ductility, cladding oxidation shall be limited to 17% of the metallic wall thickness (i.e., Equivalent Cladding Reacted or ECR), where the oxidation level is computed by means of the Baker Just correlation (cf. below) assuming conservatively that the inner and outer surfaces of the cladding are oxidized concurrently, i.e., two-side oxidation.
- (2) In order to prevent rapid cladding embrittlement as well as runaway oxidation, the cladding peak temperature shall remain below 1204°C.
- (3) The total amount of hydrogen generation shall not exceed 1% of the hypothetical amount generated by the reaction of all the metal in the surrounding fuel.
- (4) Calculated changes in core geometry shall leave the core amenable to cooling.
- (5) After any operation of the ECCS, the core temperature shall be maintained at an acceptable low value and decay heat removed for the extended period of time required by long-lived radioactivity.

The first two criteria can be assessed by means of fuel performance codes containing some specific models such as high temperature oxidation and deformation, as well as crystallographic phase transition and the rupture criterion. These specific models are dealt with in the next four sections.

2.13.3.1.2.1 Phase transition model

At high temperatures, the cladding undergoes a phase transition from the hexagonal closed packed (HCP) α phase to the face-centered cubic (FCC) β phase. The $\alpha \rightarrow \beta$ crystallographic phase transition of zirconium takes place principally in the temperature range of 800–1000°C, which is typical in a LOCA. The phase transformation is not only temperature dependent, it is also influenced by the composition and the impurities of the alloy, the corrosion level (oxygen and hydrogen contents) of the cladding and the temperature increase rate.²²⁵ Quasi-equilibrium conditions are generally assumed in the static model, where the fraction of the β phase (φ) is a simple function of the temperature: $\varphi = f(T)$. Specific functions are available for each alloy. Fig. 18 illustrates these functions for Zircaloy-4 and for Zr1%Nb,²²⁶ indicating that due to the niobium content the phase transition of zirconium is completed at temperatures about 100°C lower. In the case of a dynamic model, as proposed for example by Forgeron *et al.*²²⁷ the effect of the temperature variation rates on the phase transitions are directly taken into account by means of a differential equation:

$$\frac{d\varphi}{dt} = K(T) \cdot \varphi \cdot (1 - \varphi)$$

where $K(T)$ is an appropriate function of the temperature in the form:

$$K = \pm |T - f^{-1}(\varphi)| \cdot \exp\left(C_1 + C_2 \cdot |T - f^{-1}(\varphi)|\right)$$

t is the time, C_1 and C_2 are empirical constants. During temperature variations, the fraction of the β phase can therefore be calculated through a numerical algorithm:

$$\varphi_i = \varphi_{i-1} + K(T_i, \varphi_{i-1}) \cdot \varphi_{i-1} \cdot (1 - \varphi_{i-1}) \cdot \Delta t$$

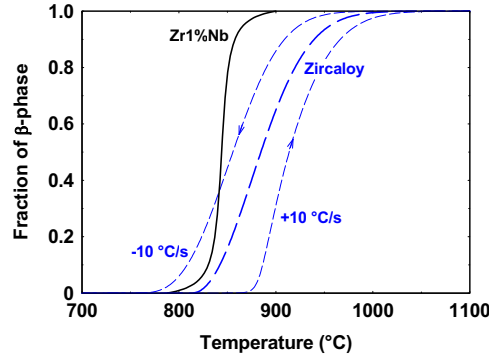


Fig. 18 Fraction of the β phase as a function of temperature calculated by the equilibrium model for Zircaloy-4 and Zr1%Nb and by the dynamic model for Zircaloy-4 at $\pm 10^\circ\text{C/s}$ temperature rates. Reproduced from Györi, C., Van Uffelen, P., Schubert, A., van de Laar, J., Hózer, Z. Implementing experimental data on the accidental behaviour of the WWER cladding obtained at the AEKI in the TRANSURANUS fuel performance code. In: Proceedings of the 6th International Conference on WWER Fuel Performance, Modeling and Experimental Support, September 19–23. Albena, Bulgaria.

where the indexes i and $i - 1$ denote the actual and the previous time steps, respectively. As an example, Fig. 18 also represents a hysteresis loop of the phase transition calculated for Zircaloy-4 by means of the dynamic model at $\pm 10^\circ\text{C/s}$ heating/cooling rates.

A similar dynamic model for the phase transition of zirconium alloys has been later proposed by Massih.²²⁵ In this model, the phase transformation rate is expressed as

$$\frac{d\varphi}{dt} = s(T)[\varphi_e(T) - \varphi]$$

where φ_e is the steady-state or equilibrium value of φ and $s(T)$ a rate parameter. The β -phase equilibrium fraction is a sigmoid function of temperature

$$\varphi_e = \frac{1}{2} \left[1 + \tan h \left(\frac{T - T_{cent}}{T_{span}} \right) \right]$$

where T_{cent} and T_{span} are material specific parameters related to the center and span of the mixed-phase temperature region, respectively, and depend on the hydrogen concentration in the material. The rate parameter is expressed in the form

$$s = s_0 \exp \left(-\frac{E}{k_b T} \right)$$

where s_0 is a kinetic factor, E an effective activation energy and k_b the Boltzmann constant.

2.13.3.1.2.2 High temperature oxidation

The cladding-steam reaction model is often based on parabolic kinetic correlations for both the oxygen mass gain and or the ZrO_2 layer thickness growth. The actual reaction rate constant is defined as a function of the temperature through an Arrhenius relation:

$$K_m = A_m e^{-\frac{Q_m}{T}}$$

where K_m is either the oxide layer thickness or the oxygen mass gain rate, A_m is the pre-exponential factor, Q_m is the activation energy divided by the perfect gas constant and T is the cladding temperature in K. The kinetics of high temperature oxidation of Zircaloy was described by Baker-Just in 1962²²⁸ by the following equation:

$$w = 2029 t^{1/2} e^{\left(\frac{-11450}{T} \right)}$$

where w is the weight of metal zirconium reacted per unit surface in mg/cm^2 , T is the temperature in K and t is the time (at the constant temperature T) in seconds. Although a more precise correlation was derived subsequently by Cathcart *et al.*²²⁹ the Baker-Just (B-J) correlation is quoted here because it is the reference correlation for expressing the cladding zero ductility criterion for LOCA accidents. An improved correlation was developed by Cathcart *et al.* (C-P) in 1977²²⁹:

$$w = 601.8 t^{1/2} e^{\left(\frac{-10050}{T} \right)}$$

The two above correlations are compared in Fig. 19, in terms of temperature and time needed to achieve the same level of oxidation (17% of metal) for a two-side oxidation of a PWR 17×17 cladding. The figure reveals that the B-J correlation is somewhat more conservative in that in the high temperature range the given oxidation level (17%) is predicted for somewhat lower temperature and/or lower time as compared with the C-P correlation. The difference is approximately 50°C in the temperature interval $1100\text{--}1200^\circ\text{C}$, whereas it is practically negligible in the $800\text{--}1000^\circ\text{C}$ range.

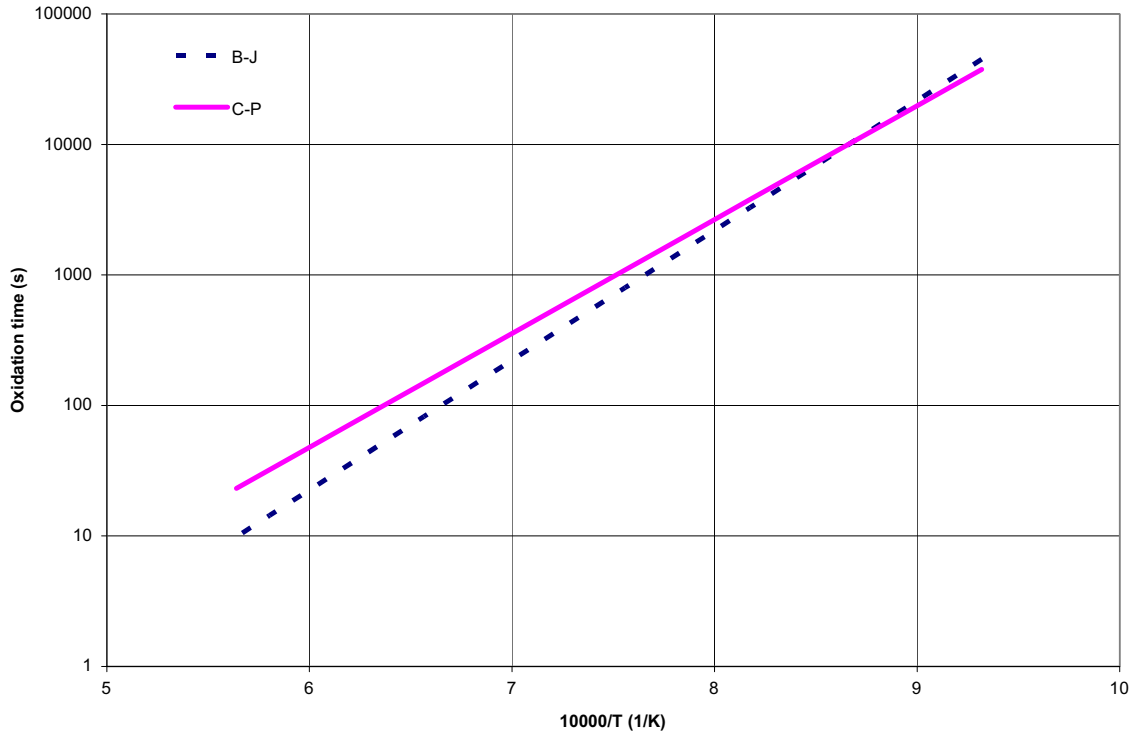


Fig. 19 Comparison of the correlations for high temperature corrosion of Zircaloy proposed by Baker-Just (B-J) and Cathcart-Pawel (C-P). Reproduced from Baker, L., Just, L.C., 1962. Studies of Metal Water Reactions at High Temperature: III. Experimental and Theoretical Studies of Zirconium-Water Reaction, ANL-6548. Chicago: Argonne National Laboratory. Cathcart, J.V., Pawel, R.E., McKee, R.E., *et al.*, 1977. Zirconium Metal-Water Oxidation Kinetics, IV. Reaction Rate Studies, ORNL/NUREG-17. ORNL.

Typical correlations for the Zr1%Nb-specific alloy were published by Solyany *et al.*²³⁰:

$$K_m = 920 e^{\left(-\frac{10410}{T}\right)}$$

and Gyori *et al.*²³¹

$$K_m = 658 e^{\left(-\frac{10200}{T}\right)}$$

At temperatures above 1204°C, data published by Urbanic *et al.*²³² and by Pawel *et al.*²³³ are available for Zircaloy. At 1853K, which is close to the monoclinic to cubic transformation of the oxide, a discontinuity has been observed in the oxidation rate.

During a LOCA, the exothermic oxidation reaction can add a significant amount of heat to a fuel system that has limited cooling. This additional heat contributes to the increase in cladding temperature, thus potentially exacerbating the associated phenomena, including oxidation itself. Oxidation energy deposition in the cladding can be modeled based on the oxidation model and the heat of reaction of zirconium oxide, e.g., Ref. 205.

2.13.3.1.2.3 High temperature deformation model

In fuel performance codes, usually a one-dimensional mechanical model is applied for the radial cladding deformation. For dealing with large high-temperature creep deformation (i.e., ballooning), typically during a LOCA-type accident, generally a strain rate correlation in the form of a Norton power equation is applied:

$$\dot{\bar{\epsilon}} = \frac{d\bar{\epsilon}}{dt} = A \cdot \exp\left(\frac{-Q}{R \cdot T} + B(x)\right) \cdot \bar{\sigma}^n$$

where $\dot{\bar{\epsilon}}$ corresponds to the effective strain rate, $\bar{\sigma}$ is the effective stress, R is the universal gas constant, T is the temperature, A is the strength coefficient, Q is the activation energy for the plastic deformation, n is the stress exponent, and x represents the oxygen weight concentration of the cladding.

The parameters in the above equation depend on the crystallographic phase of the material. In order to define the effective strain rate of the cladding in the mixed phase region there are two different approaches in the literature. According to the first approach, the Norton parameters (A , Q and n) are interpolated in the transition range using the fractions of the α and the β phases

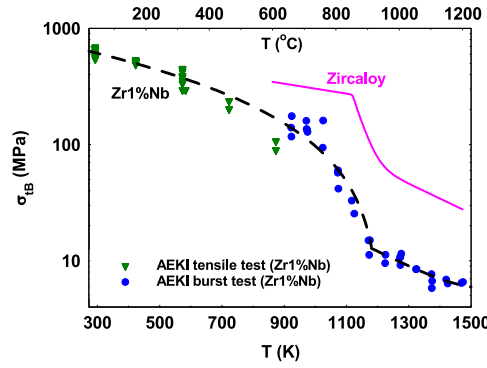


Fig. 20 True tangential stress at burst as a function of temperature applied as failure limit for un-oxidized Zr1%Nb and Zircaloy-4 claddings. The Zr1%Nb-specific function was fitted to experimental data. The failure threshold applied for Zircaloy-4 is derived from the literature. Reproduced from Hózer, Z., Györi, C. Derivation of LOCA ductility limit from AEKI ring compression tests In: Proceedings of the Special Expert Group Fuel Safety Margins (SEGFMS) Topical Meeting in LOCA Issues. Argonne, IL, USA.

as weighting factors:

$$\ln(A_{\alpha\beta}) = (1 - \varphi) \cdot \ln(A_{\alpha}) + \varphi \cdot \ln(A_{\beta})$$

$$Q_{\alpha\beta} = (1 - \varphi) \cdot Q_{\alpha} + \varphi \cdot Q_{\beta}$$

$$n_{\alpha\beta} = (1 - \varphi) \cdot n_{\alpha} + \varphi \cdot n_{\beta}$$

The second approach is based on micro-mechanical considerations for composite materials assuming a statistically homogeneous distribution of α -phase inclusions embedded in the β phase matrix, i.e., each representative volume element has the same α to β volume fraction corresponding to the macroscopic average value. According to the basic relation of self-consistency the overall average strain, and consequently the macroscopic strain rate of the two-phase cladding is expressed as the weighted average of the strain rates of each phases.

$$\dot{\varepsilon}_{\alpha\beta} = (1 - \varphi) \cdot \dot{\varepsilon}_{\alpha} + \varphi \cdot \dot{\varepsilon}_{\beta}$$

2.13.3.1.2.4 Rupture criteria for ballooning cladding

Modeling the cladding ballooning behavior is necessary to calculate the channel flow blockage fraction for ECCS coolant inside a fuel assembly. Predicting the channel flow blockage is a crucial point in evaluating the consequences of LOCA and addresses the fourth safety criterion mentioned on p. 49. In this respect, the rupture criterion for ballooning cladding gives an upper limit of the ballooning. At the attainment of this limit, the cladding is considered to have failed due to burst. For this criterion, Uchida *et al.* adopted a limit in the cladding diametral strain that forms an envelope curve of the rupture strains observed in the ballooning experiments conducted in the temperature regions of the α , $\alpha + \beta$ and β phases.²³⁴

Otherwise, the cladding failure is generally predicted on the basis of a stress assessment, i.e., the comparison of the calculated tangential stress with a distinct failure threshold. Alternatively, a strain-based failure criterion can be adopted. Both of these possibilities have for example been incorporated into the TRANSURANUS code. The first criterion is a typical stress-based evaluation, where cladding failure is indicated when the true tangential stress (σ_{tB}) exceeds the threshold stress defined on the basis of experimental data, as illustrated in Fig. 20. A widely used correlation for the threshold stress for Zircaloy-4 as a function of the temperature, oxygen content, and fraction of β phase was developed by Erbacher *et al.*²³⁵

The second failure principle is a simple plastic instability criterion based on the simultaneous assessment of the effective true strain and the strain rate. When both the strain and the strain rate exceed the threshold values of 0.02 and 100 1/h, respectively, the cladding is assumed to be ruptured.

2.13.3.1.2.5 Axial fuel relocation

In addition to complexities in the behavior of the cladding, LOCA conditions bring about specific phenomena that affect the fuel column. In particular, as the cladding balloons, fragmented and pulverized fuel pellets can fall from upper regions of the rod into the ballooned region.^{236,237} Axial relocation of fuel fragments during a LOCA is a phenomenon that causes redistribution of heat within the rod potentially accelerating cladding failure. The reduced thermal conductivity of the crumbled fuel and plenum gas mixture, in addition to the increased heat load due to a larger mass of fuel in the ballooned region, results in higher cladding temperatures further exacerbating the cladding distention. The ability to model this complex phenomenon using fuel performance codes is of great importance to ensure accurate predictions of cladding temperature, cladding strain, and the mass of fuel available for dispersal. An empirical model was developed by Jernkvist and Massih²³⁸ and coupled to the FRAPTRAN-1.5 transient fuel performance code, whereas Govers *et al.*²³⁹ attempted a more physical description.

2.13.3.1.2.6 Modeling benchmark for LOCA

Modeling fuel rod behavior during LOCA accidents has been the subject of the recent Coordinated Research Project on Fuel Modeling in Accident Conditions (FUMAC) organized by the IAEA.^{240,241} The FUMAC project has involved a benchmark of various fuel performance codes for a set of well-defined LOCA experimental cases, which has resulted in an assessment of the state of the art of fuel modeling in LOCA accidental conditions. Among the main conclusions from the project, it was noted that a significant scatter still exists in the predictions of the time to cladding burst failure from different codes. Among the reasons that could be identified for the discrepancies, besides the uncertainties in the cladding deformation and failure models were the different assumptions adopted for the calculation of the plenum temperature and consequently, the evolution of the rod inner pressure during ballooning. It was also noted that the prediction of cladding strain at burst is subject to large uncertainties. This was ascribed in part to the very high strain rates reached in the cladding as cladding burst is approached, which implies that the maximum strain is highly sensitive to the uncertainties in the cladding deformation models and the specific burst criterion adopted. Finally, the accurate determination of the thermal boundary conditions during the LOCA event was found to be critical. This is related to the exponential dependence of the cladding creep rate on the temperature and correspondingly, the high sensitivity of the cladding mechanical behavior calculation on the thermal boundary conditions.

2.13.3.1.2.7 Multi-rod behavior prediction model

In addition to the assessment of the single fuel rod behavior during a LOCA, the channel flow blockage issue requires that a multi-rod or assembly-wise behavior of rods is addressed as another important aspect of LOCA sequence prediction. Evaluation of fuel thermal and mechanical behavior in the assembly-wise geometry has inevitably to deal with multi-rod calculation, thereby consuming large computing resources. However, only with this type of numerical analysis, the actual thermal and mechanical interactions taking place between the nearest neighbor rods, second-, or third-nearest neighbor rods can be simulated.^{242–245} In the assembly, the cladding azimuthal temperature variation is generated depending on the location of rods and on the radiative heat transfer through steam among the oxidizing cladding. This azimuthal variation is much influential on the rupture strain and rupture orientation of ballooning cladding. To evaluate rod behavior in presence of azimuthal effects, in principle, full 3D analysis is needed, while most fuel performance codes rely on axially-stacked 1D (so-called 1.5D) or 2D approaches. Recently, initial fully 3D calculations of cladding ballooning in presence of azimuthal temperature variations under LOCA conditions have been performed with the BISON code.²⁴⁶ However, the multi-rod codes use a simplified 3D rod model to obtain a well-balanced performance between prediction accuracy and computing time. The channel flow blockage fraction, cladding temperature excursion, and steam oxidation amount are predicted as final results of these calculations and used as reference for a single fuel rod performance code.

2.13.3.2 Reactivity Initiated Accidents

2.13.3.2.1 Specific RIA features

As explained in articles,^{44,247} the reactivity-initiated accident (RIA) is another design basis accident for LWRs. It involves the unexpected removal of a control element from the reactor core, resulting in a prompt criticality of the reactor characterized by a rapid power excursion on a time scale of tens of milliseconds in neighboring fuel elements of a commercial reactor²⁴⁸ or in several milliseconds in a test reactor.^{249–251} Among the various scenarios considered for an RIA, the most penalizing consists of a control rod ejection at hot standby conditions in a PWR, and a control rod drop accident at cold zero power conditions in a BWR. The power increase in the rods adjacent to the ejected control rods is significant but remains limited thanks to the natural occurrence of the Doppler effect caused by the temperature increase in the fuel. Afterwards, the power is reduced to zero by insertion of fault-free control rods triggered by the reactor criticality.

During the pulse, one can distinguish three phases in the fuel rod behavior. The first phase (a few hundreds of a second) of the RIA is characterized by the quasi-adiabatic temperature increase in the fuel, accompanied mainly by solid thermal expansion and in some cases additionally by fission gas swelling. This results in a cladding temperature increase at a rate on the order of 1000°C/s and multi-axial loading on the cladding, driven by the fuel displacement. The hoop strain rate of the cladding is of the order of 1/s,²²³ which is four to five orders of magnitude larger than the strain rate during an operational power ramp of about 10 kW/m per minute.

During the first phase of the RIA, the cladding temperature typically remains below 600°C and the cladding can fail due to PCMI, depending on the specific conditions (irradiation damage, oxide thickness, hydride concentration and orientation, etc.).

During the second phase of the RIA (a few seconds), the cladding temperature continues rising because of the energy generated and transferred from the fuel, which can lead to departure from nucleate boiling (DNB). Under these conditions, the cladding temperature can remain above 1000–1200K for up to 10–15 s.²⁷ During the temperature increase the clad stiffness is strongly impaired, while the inner gas pressure of the rod increases due to gas release and the temperature increase. A local ballooning deformation may occur which may result in clad rupture.

During the third stage of the RIA (after approximately 15–20 s), the cladding is submitted to a re-wetting or quenching, which may cause a fragile rupture, especially when clad oxidation is severe (or when partial clad melting also contributes to thinning).

During the fourth and last stage of an RIA, fuel dispersal through the ruptured cladding can occur. Indeed, when the energy deposition is high enough, fuel melting or substantial fuel swelling may occur and potentially cause clad failure by overheating or overstraining. When dispersed into the coolant upon clad failure, the hot fuel may cause a pressure pulse in the water due to vaporization, potentially damaging neighboring assemblies or other core components.

Papin *et al.*²⁵² summarize the experimental observations and classify the typical sequences of rod behavior during pulse-irradiation on the basis of the results obtained from the CABRI-REP-Na tests, and Fuketa *et al.*²⁵⁰ from the NSRR tests.

2.13.3.2.2 Specific RIA modeling requirements

Among the four failures modes described above, there are two dominant types of fuel rod failures during an RIA. The first deals with a typical PCMI failure and is predominant for fuel rods irradiated to an average burnup beyond 30–40 MWd/kgHM because of gap closure and clad ductility reduction (associated with hydrogen pick-up and brittle hydride formation). The second type of failure is more typical for fuel rods with a lower burnup level and is caused by gaseous pressure at high temperature during the post-DNB phase.

2.13.3.2.2.1 Thermal and mechanical calculations for fast transients

To cope with the speed of the temperature increase and the large radial gradients, an accident analysis code needs an appropriate number of radial ring elements and numerical stability. In addition, the temperature gradient generates a strong thermal stress particularly within a pellet. Therefore, in general FEM is the most versatile and reliable method used in these situations.^{253,254}

The prediction of DNB and recovery to re-wetting after the PCMI phase is difficult to model because of the limited amount of experimental data.²⁵⁵

2.13.3.2.2.2 FGR during RIA

The internal gas pressure during an RIA can be considerably enhanced (5%–25%) by the burst release of fission gas associated with grain-boundary separation,^{182,183,256} and has been generally correlated with the peak fuel enthalpy.²⁵⁷ The fission gas is released mainly from the inter-granular gas bubbles.^{257,258} Although a few models consider the thermal diffusion process of fission gas atoms and bubbles from inside the grains as significant for the enhanced FGR during an RIA (e.g., Refs. 25,259), it is generally accepted that the inter-granular mechanisms are dominant.²⁵⁷ This is mostly ascribed to the short duration of the high temperature period of the pellet, which limits the contribution of diffusional mechanisms to the FGR increase. However, depending on the specific conditions, fission gas diffusion to grain boundaries during the RIA event can be non-negligible.¹⁹³ Although this can be included in the high temperature failure criterion for the cladding during RIA, when expressing the enthalpy limits as a function of the pressure difference that includes the transient fission gas release, more research is required, for Gd-doped fuels and MOX at high burnup^{260,261} for example.

In any case, it is necessary to evaluate the pre-accident gas inventory within the pellet, particularly in the inter-granular gas bubbles. Obviously, this evaluation depends on the performance of all the models that are responsible for fission gas behavior during the base-irradiation period.

Most research is directed towards the PCMI failure type because of the tendency to increase the average discharge burnup levels for economic reasons, and because this is considered to be the most severe criterion for high burnup rods. The prediction of fuel rod failure during an RIA requires the use of a computer code that accounts for the various aspects of the fuel behavior. In order to guarantee acceptable calculation times, however, only simplified models for the clad rupture can be afforded rather than complex mechanistic models. On the basis of the experimental results and main characteristics, several RIA rupture criteria have been proposed and are adopted in fuel performance codes (cf. state-of-the-art report of NEA²⁷ currently being reviewed). The models are either based on the rupture strain, or in terms of a rupture strain energy density (SED), or in terms of an enthalpy limit. In order to compare the rupture hoop strain or critical SED with the safety criteria currently applied (on the basis of the in-pile tests), they must be expressed in terms of (radially averaged) maximum enthalpy (or enthalpy increase) in the fuel versus rod average burnup. Such conversion requires the implementation in a fuel performance code and the selection of a particular irradiation history for a chosen fuel design.

2.13.3.2.2.3 Cladding failure

The models based on rupture strain postulate clad failure when:

$$\begin{aligned}\varepsilon_{\theta}^p &\geq \varepsilon_{\theta}^*(z, t) \\ \dot{\varepsilon}_{\theta}^p(z, t) &> 0\end{aligned}$$

where ε_{θ}^p and $\dot{\varepsilon}_{\theta}^p$ represent the radially averaged clad hoop strain and strain rate, respectively. The uniform hoop elongation is often selected for two reasons. Firstly, the largest strains due to PCMI are in the tangential direction. Secondly, the true failure strain is somewhere between uniform elongation and total elongation (includes both uniform and localized strain) at failure. Geelhood *et al.*²¹⁹ have implemented such a uniform strain based failure model in the FRAPTRAN code. The empirical correlation was derived from biaxial burst tests in addition to uniaxial tension tests on irradiated Zircaloy, and is a function of the temperature and excess hydrogen in the cladding (i.e., the quantity of hydrogen above the solubility limit). Therefore, a correction factor had to be applied because of the non-representative stress conditions. They also implemented a new yield stress correlation, whereby the plastic strain hardening component is dependent on both the temperature and the fast neutron fluence (representing radiation damage) and has been fitted on the basis of the same set of experiments. As a result their failure predictions account for the temperature, the irradiation damage, the strain rate and the hydrogen content. In a similar manner Jernkvist²⁶² proposed

more recently an empirical correlation for ε_{θ}^p for recrystallized Zry-2 and stress-relieved Zry-4 on the basis of more than 200 out-of-pile mechanical property tests:

$$\varepsilon_{\theta}^f = \frac{3 \cdot \varepsilon_{\theta}^0 \cdot S \cdot f_1 \cdot f_2 \cdot f_3}{f_1 \cdot f_2 + f_1 \cdot f_3 + f_2 \cdot f_3}$$

where ε_{θ}^0 is the plastic strain to failure of as-fabricated cladding at low strain rate, S is a ductility reduction factor for clad tubes with spalled oxide layer, responsible for detrimental effects of a non-uniform hydride distribution, and f_1 , f_2 and f_3 are ductility reduction factors accounting for elevated strain rate, hydrogen-induced embrittlement and radiation damage, respectively. The functions have been fitted to the experimental data and are as follows:

$$\begin{aligned} \varepsilon_{\theta}^0(T) &= 2.82 \times 10^{-2} + 1.22 \times 10^{-4} T \\ f_1(\dot{\varepsilon}_{\theta}) &= \begin{cases} 1.0 & \dot{\varepsilon}_{\theta} < 8.37 \times 10^{-4} \text{ s}^{-1} \\ 0.046 - 0.31 \log_{10} \dot{\varepsilon}_{\theta} & 8.37 \times 10^{-4} \text{ s}^{-1} \leq \dot{\varepsilon}_{\theta} \leq 1 \text{ s}^{-1} \\ 0.046 & \dot{\varepsilon}_{\theta} > 1 \text{ s}^{-1} \end{cases} \\ f_2(c_{\text{Hex}}, T, \dot{\varepsilon}_{\theta}) &= 0.01 + 0.99 e^{-\gamma(T, \dot{\varepsilon}_{\theta}) c_{\text{Hex}}} \\ \gamma(T, \dot{\varepsilon}_{\theta}) &= 6.52 \times 10^{-4} + 2.21 \times 10^{-3} (6 + \log_{10} \dot{\varepsilon}_{\theta}) \left[1 - \tan h \left(\frac{T - 298}{8.5} \right) \right] \\ f_3(\phi) &= 0.05 + 0.95 e^{-2.89 \times 10^{24} \phi} \end{aligned}$$

The empirical correlation for the rupture hoop strain is valid for temperatures between 20 and 400°C, deformation rates between 5×10^{-5} and 1 s^{-1} , hydrogen concentrations in the range of 0–1941 ppm, and fluences between 0 and $12 \times 10^{25} \text{ n/m}^2$. Jernkvist²⁶² implemented this rupture threshold in the SCANAIR-3.2 code, which was originally developed at the IRSN in France. The threshold was evaluated on the basis of integral tests in the CABRI and NSRR pulse reactors. The comparison with the experimental data indicated that the strain-based criterion was conservative, and that the standard deviation of the relative differences between calculated and measured failure strain obtained with the modified SCANAIR-3.2 code was 0.57. A part of the scatter has been attributed to the deviation of the loading conditions of the out-of-pile tests from those of the in-pile tests (tangential and axial loading nearly equal), which required the application of a correction factor to the measured hoop strains.

Desquines *et al.*²⁶³ adopted a more physically based modeling for defining the rupture strain. More precisely, they applied the concept of elasto-plastic failure mechanics, in line with Kuroda *et al.*²⁶⁴ and combined this with a probabilistic model for the defect size and the oxide layer thickness (or average hydrogen content) in order to determine the failure probability as a function of the hoop strain at failure, the oxide layer thickness, the temperature and the height of the fuel rod.²⁶⁵ An issue was the lack of experimental validation data at temperatures above 400°C. The rupture criterion was applied in the SCANAIR code.

The strain based failure criterion is conceptually simple, and the correlation can be determined in a rather straightforward manner from total elongation as well as burst strain data. However, for these data attention must be paid to the impact of the specimen geometry and load biaxiality. Furthermore, the strain-based failure criterion depends on the mechanical loading and temperature history prior to failure. As an alternative, a critical strain energy density (CSED) has been proposed by Rashid *et al.*²⁶⁶ and implemented in the FALCON code. The measure for the clad to resist failure is formulated as the total mechanical energy (elastic + plastic) per unit volume that can be absorbed by the material before it can fail. The threshold value for SED is derived from the experimental stress-strain curves and is expressed as a function of the fast neutron fluence, temperature, hydrogen concentration and material type, or alternatively the oxide thickness. A correction factor was applied to account for deviations from the biaxiality of stress during the tests, and it is noted that the tests were limited in terms of strain rate ($7 \times 10^{-5} \text{ s}^{-1}$ instead of $1\text{--}5 \text{ s}^{-1}$ for RIA). A similar approach was adopted by Bernaudat *et al.*²⁶⁷ and Leclercq *et al.*²⁶⁸ for usage in the SCANAIR code applied by EDF. However, in this approach the CSED limit was expressed as a function of the oxide thickness or the average burnup:

$$\begin{aligned} \text{CSED} &= 95.17 - 4.7653 \cdot \text{OX} + 8.759 \cdot \text{OX}^2 - 5.56 \times 10^{-4} \cdot \text{OX}^3 & \text{OX} < 54 \text{ } \mu\text{m} \\ \text{CSED} &= 5.3 & \text{otherwise} \end{aligned}$$

where OX is the oxide thickness in μm and CSED is expressed in mPa. The conversion of the oxide thickness in average fuel burnup depends on the material under consideration, although Bernaudat *et al.*²⁶⁷ concluded that the correlation derived for Zircaloy-4 could be (conservatively) applied to ZIRLOTM and M5TM.

The strain energy density is not as easily measured in mechanical property tests as the plastic strain to failure, and direct measurements of this quantity are seldom made. In addition, the derivation of the SED from the experimental data relies on a constitutive relation for the material, and is also sensitive to the load and temperature history. There is thus no obvious benefit in using the critical SED instead of a critical strain in clad failure criteria for RIA.²⁶²

Furthermore, the plastic strain of cladding at failure is a few to several tenths of percent in calculation, although the actual plastic strain is largely localized around the fracture site. Metallographic cross-sectional observation of PCMI-failed cladding indicates that some incipient cracks are generated in the outer oxide layer or in the dense hydride (embrittled) region under the oxide.^{269,270} The crack then grows and propagates in the reduced ductility region to the inner part, and at a certain depth onset of through-wall fracture occurs. A direct implication of these observations is that the plastic strain around the crack tip is mainly responsible for the onset of through-wall fracture, i.e., final fracture. In other words, fracture toughness is associated

with the small region around the crack tip, and the cladding inner region, which is heated to high temperature, would have a negligible contribution to the fracture toughness. From this point of view, further study is justified to design an alternative failure criterion²⁷¹ to the macroscopically derived quantities such as CSED or plastic strain to failure. Further research has been and continues to be dedicated to include also the effect of absorbed hydrogen (and the associated brittle hydride formation).²⁶⁰

Finally, in order to address molten fuel-induced swelling PCMI cladding failure (post DNB), one should ensure that the peak fuel temperature remains below incipient fuel melting conditions. The effect of burnup on the radial power distribution, the thermal conductivity and the melting temperature should be properly accounted for.

2.13.3.2.2.4 Modeling benchmark for RIA

Recently, a benchmark of fuel performance codes for the fuel behavior simulation during RIAs organized by the OECD/NEA was finalized. The benchmark involved several organizations from different countries and was comprised of a Phase I²⁷² and a Phase II.²⁷³ The main conclusions from the Phase I of the activity included²⁷²:

- While the differences in the evaluation of fuel temperatures from the different codes remained limited, calculated cladding temperatures exhibited considerable scatter, in particular for behavior post-DNB. Large differences in the predictions of cladding hoop strain also were observed for cases where water boiling was predicted to appear.
- For the predictions of fuel stack elongation, the scatter was limited. The cladding elongation was found to be much more difficult to evaluate.
- For FGR, discrepancies of up to a factor of 2 between the codes were observed, which were considered to be relatively moderate given the complexity of the phenomenon.

Subsequently, Phase II of the benchmark exercise was started, which ultimately led to the following main conclusions²⁷³:

- With respect to the fuel thermal behavior, the differences in the estimation of fuel enthalpies and temperatures were rather limited. However, the agreement was worse for BWR thermal-hydraulic conditions than PWR thermal-hydraulic conditions that lead to water boiling. This seemed to be mainly driven by uncertainty in the clad-to-coolant heat transfer.
- Considerable scatter in the calculated cladding temperatures was observed for the cases that involved water boiling. This scatter was associated with differences in modeling the cladding-to-coolant heat transfer. Given the lack of sufficient experimental investigation on boiling in RIA conditions, no clear recommendation could be made as for which correlations are the most suitable ones to use.
- There is a need to enable the fuel performance codes to handle the thermal-hydraulic conditions expected in a BWR RIA with large energy injection at cold, zero-power conditions.
- Significant discrepancies were again observed for cladding hoop strain, fuel and cladding elongation, and cladding hoop stress. The reasons could only be partly attributed to the specific modeling approaches; dependency on key boundary conditions for cladding loading, such as the gap closure/opening, was also heavily involved.

As a result of this benchmark activity, it was recommended to pursue improvements in modeling capabilities for the cladding-to-coolant heat transfer in the case of water boiling during very fast transients. It was also pointed out that models for the evolution of the fuel-to-cladding gap should be improved and validated in RIA conditions as this had been shown to have a significant effect on the simulated fuel rod response.

2.13.4 Advanced Issues and Future Needs

2.13.4.1 Deterministic Versus Probabilistic Analyses

In the introduction, we have enumerated the various sources of uncertainties, and in the second section we have provided more details about the limitations of the models. In order to assess the technological effect of all sources of uncertainties there are various techniques that may be considered.

First of all, there are various so-called sensitivity analysis methodologies. Relative to uncertainty quantification (UQ), which seeks to obtain probability distributions for the outputs given a set of distributions for the inputs, sensitivity analysis (SA) aims to gain an understanding of the output range given a particular input domain, and to assess the importance of the different input parameters.

SA techniques range from multiple runs with input data or model parameters being varied, up to a rigorous mathematical treatment based on perturbation theory. The numerical noise analysis allows for the estimation of the standard deviation of an output quantity (for instance, the fuel centreline temperature) within just one run. For this purpose, selected input parameters of the fuel rod model are varied slightly on a random basis in an interval (numerical noise). By evaluating the resulting changes of the output quantities, one can assess the sensitivity of the code's results to the variations of the input parameters. One example is the numerical noise technique that was included in the TRANSURANUS code.²⁷⁴ While the computational effort for this type of SA is equivalent to a deterministic run, no information is obtained on the interactions between variations of different parameters.

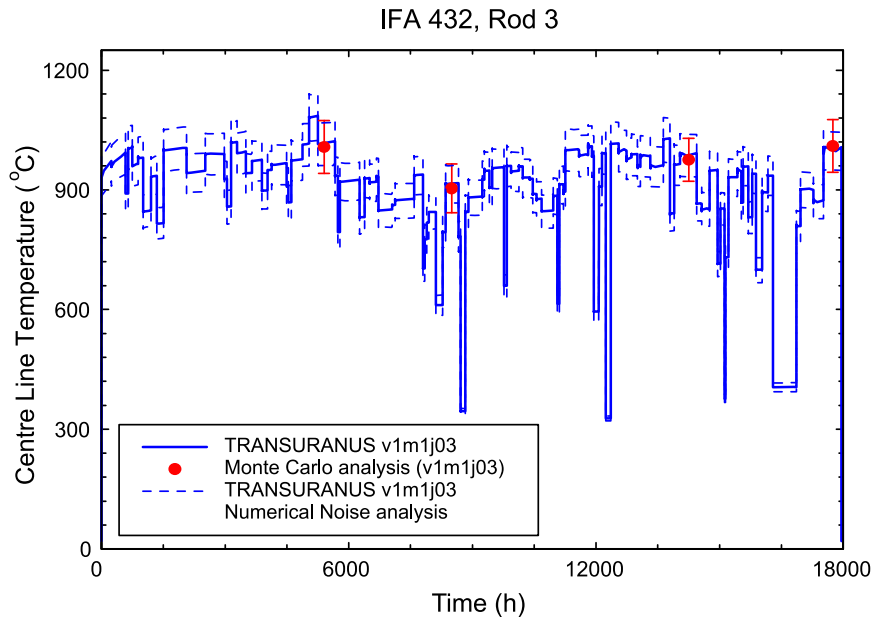


Fig. 21 Comparison between a deterministic and two statistical analyses implemented in the TRANSURANUS code.

A second category of probabilistic approaches is the response surface technique. Examples include the Latin Hypercube Sampling (LHS) and the Taguchi design. Peck²⁷⁵ tested this with the FRAP code. A disadvantage of this approach is the need to identify in advance the selection for the input parameters and the corresponding variation ranges. Also, this approach requires a definition of the interactions between the perturbed parameters.

The Monte Carlo method is used relatively often in the nuclear fuel modeling area. It is based on random sampling of all variables that are considered and is straightforward. Disadvantages of this method include the large number of cases involved that may result in a high computational cost, and the implicit requirement for the knowledge of the distributions of the input parameters. Furthermore, the outcome usually does not allow for disentangling the individual contribution of each uncertain input parameter. In order to reduce the computational burden, quasi-Monte Carlo methods have been considered. These combine the variations of parameters in response surface techniques with the standard Monte Carlo method. As a result, the quasi-random sampling sequences fill the variable space more uniformly compared to random numbers. For example, quasi-Monte Carlo methods have been applied, to probabilistic nuclear fuel analysis using the STAV6 code.²⁷⁶

In Fig. 21, a comparison is made between a deterministic and the two statistical analyses in the TRANSURANUS code. The symbols with the error bars indicate the mean value and the standard deviation of the fuel centreline temperature at four distinct times according to a Monte Carlo analysis, whereas the dashed line indicates the standard deviation according to the numerical noise analysis. The comparison shows that the latter method, even though it is computationally equivalent to a single deterministic run, provides a similar approximation for the standard error of the centerline temperature as the Monte Carlo technique in the case under consideration.

In Fig. 22, a potential problem of a Monte Carlo calculation is illustrated. More precisely, depending on the standard deviations chosen for the input variable's distributions, the resulting distribution of the output (fuel centreline temperature) covered a range as wide as 400°C. While results below a specific frequency may be neglected for the analysis, the choice of the cut frequency is not obvious.

Despite the restrictions, applying a limited variation of some fabrication variable parameters in fuel rod performance calculations is being considered in Germany^{277–279} and the USA²⁸⁰ for two reasons. First of all, it is argued²⁷⁷ that probabilistic calculations can replace a deterministic calculation with the worst case dataset, i.e., a superimposed unfavorable tolerance limit on some fabrication parameters. While the deterministic worst-case calculation would be very conservative, with a degree of conservatism that would be difficult to quantify, probabilistic calculations based on distributions would lead to results with a known, defined conservatism. Secondly, it has been observed that in some cases probabilistic calculations predicted a worse fuel performance compared to the deterministic approach. This, of course, depends on the proper definition of the worst case and on the ranges of parameters variation applied in the probabilistic calculations.

For these reasons, a semi-statistical design approach has been proposed in Germany.^{278,279} The method consists of computing Spearman's rank coefficients following a limited number of Monte Carlo simulations. In order to obtain a set of parameter combinations that provides a response covering, with a given probability, the whole output range that corresponds to all possible parameter combinations, the rank coefficients are converted into quantiles of the statistical distributions. This set of parameters is then applied to deterministic fuel rod computations.

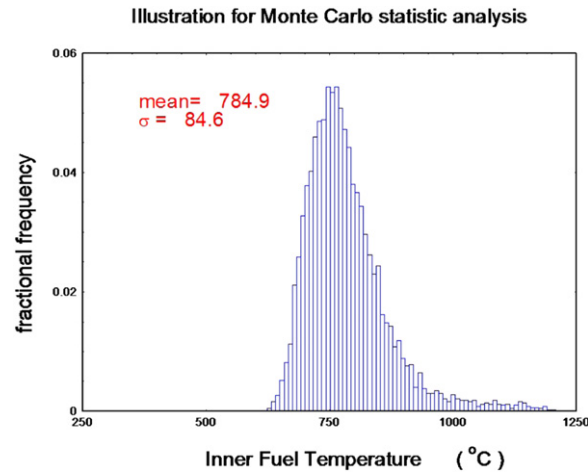


Fig. 22 Fractional frequency of the center line temperature predictions, when varying only three input parameters (q' , h_{gap} , λ) within given distribution and uncertainty ranges (q' : Gaussian distribution with $\sigma = 5\%$ and cut-off at 10%, h_{gap} with uniform distribution with a factor ranging from 0.1 to 10, and λ : Gaussian distribution with $\sigma = 10\%$ and cut-off at 20%).

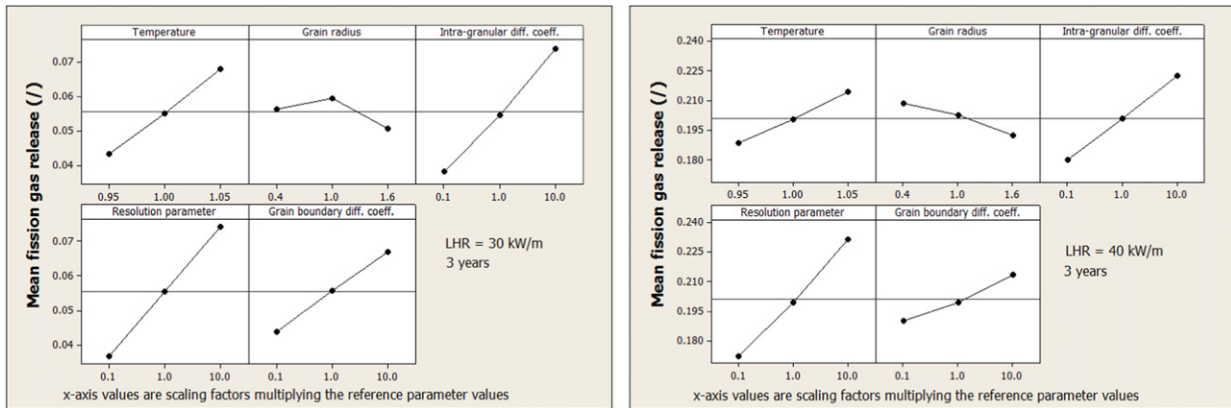


Fig. 23 Relative influence of the variation of five parameters on calculated fission gas release for a 3-year steady-state irradiation at 30 kW/m (left) and 40 kW/m (right). Reproduced from Pastore, G., Swiler, L.P., Hales, J.D., *et al.*, 2015. Uncertainty and sensitivity analysis of fission gas behavior in engineering-scale fuel modeling. J. Nucl. Mater. 456, 398.

In a similar manner, a non-parametric order statistics method has been applied in the USA,²⁸⁰ and more recently also in Finland with the FRAPTRAN-GENFLO code.²⁸¹ The method provides a more realistic estimation of the operational margin. This is obtained through the statistical evaluation of the number of fuel rods for which a design limit is approached to evaluate the probability for the actual occurrence of extreme cases.

An uncertainty and sensitivity analysis of nuclear fuel behavior was performed in Ref. 282 using Monte Carlo sampling and both the Spearman correlation coefficient method and Sobol' variance decomposition analysis to allow the study of interactions between input variables. The Sobol' variance decomposition included evaluation of the first order, second order and total effect sensitivity indices, and was shown to perform significantly better in cases where non-additive interactions between input variables were present. The results suggested that first order SA methods are in general insufficient for application to nuclear fuel modeling because of the importance of input interactions, and significant improvements can be achieved by using higher order methods.

In order to identify the input parameters that have the most significant influence on the output, a SA technique called main effects analysis and based on orthogonal array sampling (OAS) has been used. This technique assesses the effect of an independent variable (input parameter) on a dependent variable (output quantity), averaging across the levels of the other independent variables (main effect).^{283,284} For instance, main effects analysis has been applied to a SA of the fission gas behavior model in the BISON fuel performance code.¹⁵⁶ In this case, BISON was integrated with the DAKOTA software²⁸⁵ to perform a SA of fission gas release and swelling calculations to selected model parameters. Fig. 23 from Ref. 156 shows the relative

importance of each of the five considered uncertain parameters in the calculation of FGR, obtained through main effects analysis.

In order to determine the uncertainty in the input parameters, expert judgement is often used, however, inverse UQ methods have also been applied. Inverse UQ seeks statistical descriptions of the uncertain input parameters based on the available measured data for the output quantities. For instance, an inverse UQ study using the Bayesian inference theory was applied to determine distribution functions of the uncertain parameters in the BISON code's fission gas behavior model, based on time-dependent experimental data for FGR.²⁸⁶ Markov Chain Monte Carlo sampling of the input parameters was applied along with a Kriging metamodel (a generalized linear regression model to approximate a deterministic computer model, also known as Gaussian Process emulator²⁸⁷) for the BISON code to reduce the computational cost.

To execute SA and/or UQ of nuclear fuel calculations, three different ways have been considered. A first, most straightforward approach is to couple the fuel rod performance code with a statistical package that enables a great deal of flexibility and sophistication. This has been performed for the FRAPCON,²⁸⁸ PAD5⁶⁶ and BISON¹⁵⁶ fuel codes using the DAKOTA statistical software,²⁸⁵ and for the METEOR and ALCYONE fuel codes using URANIE.^{289,290} While such an approach demands the development of an interface between the fuel simulation tool and the statistical package, it enables the application of different statistical tools such as first and second order reliability methods, surrogate models, Monte Carlo sampling, etc. A second approach consists of writing a statistical wrapper around a fuel performance code with a graphical user interface. Examples include applications to the TRANSURANUS²⁹¹ and ENIGMA²⁹² fuel performance codes. Relative to the first one, this approach is usually more tailored to the specific needs or scope of the user. The third way consists of implementing statistical abilities in the fuel performance package itself. Such an integrated statistical package is available in the TRANSURANUS code.²⁹³ Despite the many recent attempts to take into consideration the uncertainties (e.g., Refs. 282,286,294), as of today no consensus has been reached yet about which method should be applied in licensing.

2.13.4.2 High Burnup

The resonance absorption of epi-thermal neutrons by ²³⁸U leads to the build-up of ²³⁹Pu in the pellet periphery, after two successive β -decays. The high local burnup in combination with the low temperature leads to the formation of the high burnup structure (HBS), sometimes referred to as the "rim-effect" because of its appearance in the pellet rim (several 100 μ m at a pellet burnup of 55 MWd/kgHM). The HBS is characterized by micron-sized pores with a swelling contribution up to 15%, surrounded by small grains on the order of 100–300 nm with a very low concentration of Xe between 0.1 and 0.2 wt%.^{295,296} HBS formation starts at the pellet periphery when the local burnup exceeds a value of about 60 MWd/kgHM, and the local temperature remains below approximately 1000°C. Evidence for recrystallization was found throughout the pellet cross sections of fuel samples irradiation at low power to 100 MWd/t_{HM}²⁹⁷ and the HBS was studied in very high burnup fuel discs.^{298,299} It has also been observed in MOX fuel.^{300–302} Nevertheless, a different type of grain subdivision into sub-domains or sub-grains has been recently observed in the central part of high burn-up fuels.^{303,304} This phenomenon requires more observations to understand the mechanisms and the conditions involved. For instance, a recent analysis based on electron microscopy in intermediate zones enabled to point out the role played by polygonization in the HBS formation process.³⁰³

The mechanisms responsible for the development of the HBS, as well as a description of its consequences on fuel behavior have been reviewed recently.^{1,152,303} In the present article, we limit ourselves to an outline of how it is accounted for in fuel performance codes.

First of all, the effect of the HBS on the heat transfer is generally included in a correlation describing the thermal conductivity degradation

$$\lambda = \frac{1}{A_0 + A_1 \cdot bu + B \cdot T}$$

and the porosity build up in the HBS as well as in an improved gap conductance in order to account for the chemical bonding layer between the ceramic pellets and the metallic cladding. To this end, for example, the cladding and pellet roughness is empirically reduced above a certain burnup to account for the filling up by mainly zirconium oxide, which has a higher thermal conductivity than that of the mixture of He and Xe in the residual gap.

Thermal conductivity degradation of the fuel is sometimes considered to saturate

$$\lambda = \frac{\sqrt{\lambda_0}}{D\sqrt{bu}} \arctan\left(D\sqrt{bu}\sqrt{\lambda_0}\right) + \lambda_{el}$$

with $\lambda_0 = 1/(A + B \times T)$ and D is a constant.³⁰⁵ It can be shown that in the low burnup limit this expression tends to the classical form of λ_0 . Occasionally partial thermal conductivity restoration is even considered when the HBS is created. In this way account is made for the "cleaning" of the matrix from point defects and fission products, which relies on an empirical formulation of the lattice parameter variation.³⁰⁶ The latter approach is supported by detailed experimental data.³⁰⁷

The effect of the long irradiation time in the mechanical analysis is mostly accounted for in the cladding properties. The process of outer cladding corrosion liberates hydrogen from the water, and reduces the thickness of the cladding metallic wall. A fraction of that hydrogen, called the hydrogen pickup fraction is absorbed by the Zircaloy. This fraction depends on the composition and heat

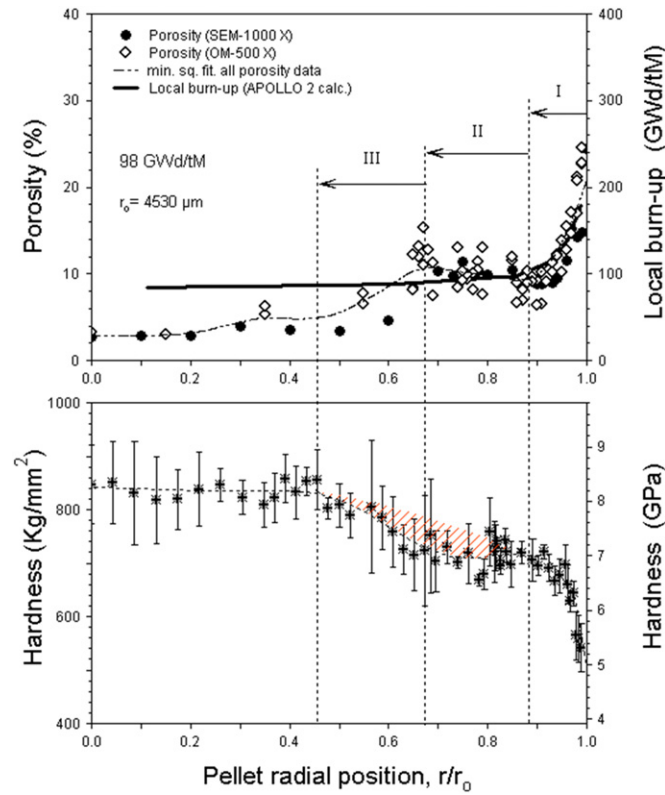


Fig. 24 Experimental values for micro-hardness of irradiated UO_2 fuel with a burnup of 98 GWd/tHM. Reproduced from Spino, J., Stalios, A.D., Santa Cruz, H., Baron, D., 2006. Stereological evolution of the rim structure in PWR-fuels at prolonged irradiation: Dependencies with burn-up and temperature. J. Nucl. Mater. 354, 66.

treatment of the cladding, as implemented for example as follows³⁰⁸:

$$F(s) = a_1 + \frac{a_2}{sa_3} (1 - e^{-sa_3})$$

$$c_H = c_{H0} \frac{s}{(r_o - r_i)} \frac{2r_o}{(r_o + r_i)}$$

where

$F(s)$ = hydrogen pickup fraction in the cladding (/)

s = corrosion layer thickness

$r_{o,i}$ = reference cladding outer/inner radius

c_H = integrated hydrogen uptake (ppm)

and the parameters were obtained by Limbäck *et al.*³⁰⁹ from a fit to data of the total hydrogen pickup fraction in oxidized Zy-2 and Zy-4: $c_{H0} = 28,940$ ppm, $a_1 = 0.0584$, $a_2 = 0.329$, $a_3 = 0.114 \mu\text{m}^{-1}$.

The hydrogen concentrates in the cold part of the cladding. As soon as the solubility limit is exceeded, it precipitates as brittle hydrides. When these hydrides are oriented normal to the cladding surface, the cladding strength is further reduced, which may have a strong impact during power variations.

Also in the fuel pellets, the effects of high burnup have been characterized. The reduction of the micro-hardness (Fig. 24) and Young's modulus (cf. Fig. 25) observed in high burnup fuel pellets was only recently included in the codes (see for example Refs. 312,313). Nevertheless, the chemical bonding between pellet and cladding is not included. On the one hand, the bonding layer improves the pellet-cladding interaction resistance since it is much softer than UO_2 . On the other hand, it would make the cladding subjected to a bi-axial stress state due to pellet stack elongation. This bi-axial stress state is a mechanically more tough condition for cladding.³⁸

The HBS is also associated with the radial power profile in the pellets, and has been reviewed recently.¹ The resonance capture of epithermal neutrons in the peripheral regions of the pellets renders the application of neutron diffusion theory obsolete. In order to reproduce the stronger gradient in the pellet rim, fuel performance codes rely on empirically fitted functions reflecting the resonance capture, for instance in RAPID³¹⁴ or TUBRNP.³¹⁵ The latter solves the local differential

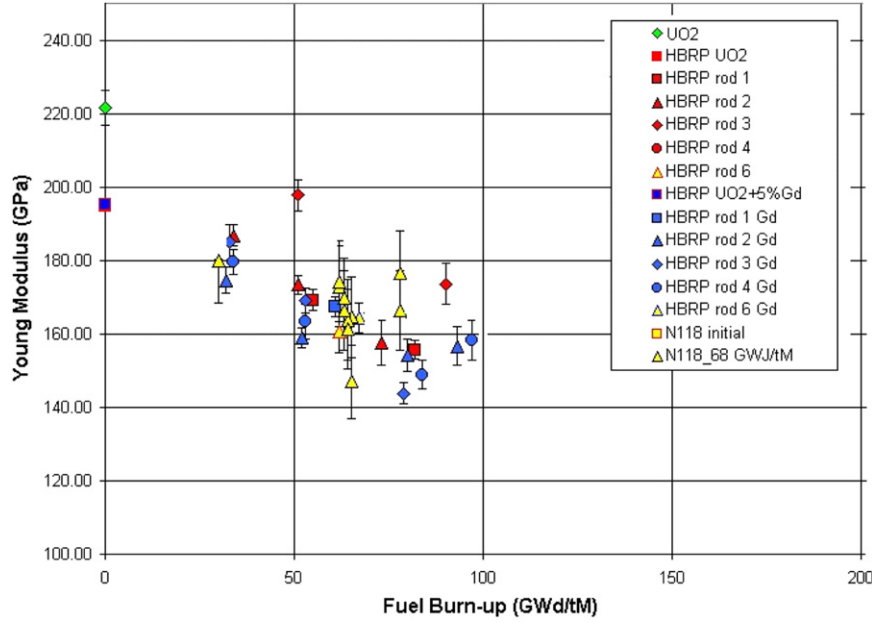


Fig. 25 Experimental Young's modulus of irradiated LWR fuels as a function of burnup. Reproduced from Baron, D., Masson, R., Gatt, J., Spino, J., Laux, D., 2005. Evolution of the nuclear fuel mechanical properties with burn-up. An extensive european experimental program. In: Proceedings of the International Topical Meeting on Light Water Reactor Fuel Performance, October 2–6, 2005, p. 957 Kyoto, Japan: American Nuclear Society.

equations for the uranium and plutonium isotopes:

$$\begin{aligned}\frac{dN_{235}(r)}{dbu} &= -\sigma_{a,235}N_{235}(r)A, \\ \frac{dN_{238}(r)}{dbu} &= -\sigma_{a,238}\bar{N}_{238}f(r)A, \\ \frac{dN_{239}(r)}{dbu} &= -\sigma_{a,239}N_{239}(r)A + \sigma_{c,238}\bar{N}_{238}f(r)A, \\ \frac{dN_j(r)}{dbu} &= -\sigma_{a,j}N_j(r)A + \sigma_{c,j-1}N_{j-1}(r)A.\end{aligned}$$

The local concentration of ^{238}U , $N_{238}(r)$, is rather uniform and thus written as \bar{N}_{238} whereas $f(r)$ is the radial shape function to account for the resonance reactions and is normalized by $\frac{2 \int_{r_{in}}^{r_{out}} f(r) r dr}{r_{out} - r_{in}} = 1$, where r_{in} and r_{out} are the inner and outer fuel radii. The function $f(r)$, called the radial shape function, is $f(r) = 1 + p_1 \exp(-p_2(r_{out} - r)^{p_3})$. The constants p_1 , p_2 and p_3 are fitted to EPMA data for each type of reactor.

Finally, the impact of the HBS on fission gas release is incorporated in various ways in fuel performance codes, reflecting the lack of consensus for a satisfactory explanation.¹⁵² The simplest way is based on an empirical threshold for the onset of release depending on the local burnup, and/or temperature and/or initial grain size. Others include the burnup as a parameter in the diffusion coefficient or the S/V value (for the Booth sphere radius), in the grain boundary saturation value, or the resolution efficiency as function of the bubble radius. Quantitative details of most models are not available in the open literature. In the START3 code³¹⁶ the grain size reduction observed is modeled in an empirical manner as a function of temperature and burnup. As the average distance for intra-granular diffusion thereby reduces, an increased release fraction is predicted. Nevertheless, there is evidence that direct release from the HBS is small under normal operating conditions.^{152,310} Apart from this general statement that the release is small, there is no consensus about the quantitative contribution from the HBS to the overall release under normal operating conditions. This is very well reflected in the large spread of fission gas release predictions at very high burnup for the codes involved in the FUMEX-II benchmark exercise organized by the IAEA (Fig. 26), and was confirmed in FUMEX-III.³¹⁸

Under design basis accident conditions, the release models disregard the kinetics. Release is assumed to be instantaneous (provided that the gap is open) and comes from grain boundary cracking. The precise modeling of this relies on the modeling of the local conditions of temperature and stress, which is very difficult but hardly discussed in publications. Only recently some attempts were made to investigate the transient fragmentation by means of a micro-mechanical analysis³¹⁹ or to reproduce burst release at two different temperature levels on the basis fragmentation caused by gas-filled pores in mechanistic manner.³²⁰

Finally, the swelling in the HBS is mostly modeled separately with a very simple linear or quadratic function of burnup (Fig. 27). Also the width of the HBS structure is sometimes modeled empirically as a function of the burnup.

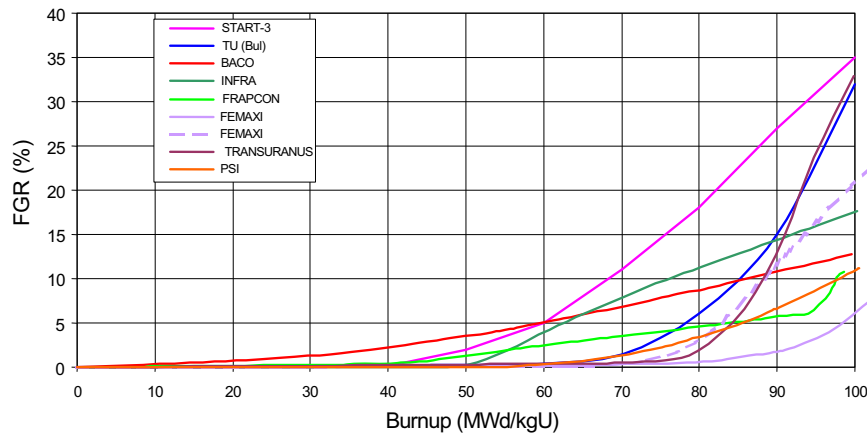


Fig. 26 Cumulative fractional fission gas release predicted for a constant linear heat rate of 15 kW/m by various fuel performance codes involved in the FUMEX-II round robin exercise of the IAEA. Reproduced from Killeen, J., Turnbull, J.A., Sartori, E., 2007. Fuel modeling at extended burnup: IAEA coordinated research project FUMEX-II. In: Proceedings of the International LWR Fuel Performance Meeting, September 30–October 3, 2007, p. 261. San Francisco, California, USA: ANS.

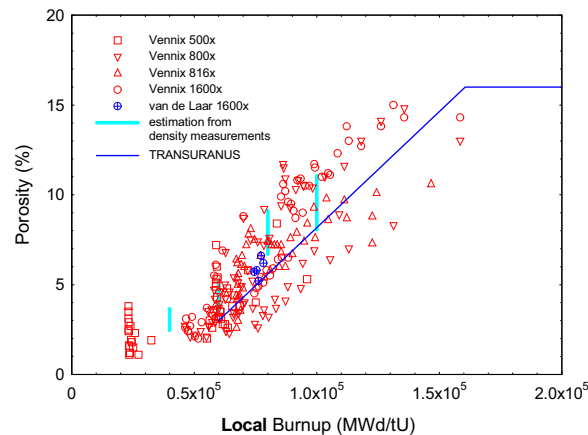


Fig. 27 Porosity as a function of the local burnup for highly irradiated fuel, and the corresponding correlation adopted in the TRANSURANUS code. Reproduced from Lassmann, K., Schubert, A., van de Laar, J., Vennix, C.W.H.M., 2000. Recent developments of the TRANSURANUS code with emphasis on high burnup phenomena. In: Proceedings of the Technical Committee Meeting on Nuclear Fuel Behavior Modeling at High Burnup, IAEA-TECDOC-1233, p. 387, Lake Windermere, UK: IAEA.

2.13.4.3 Mixed Oxide Fuels

Because the plutonium concentration of MOX fuel in LWRs is low, its behavior in a reactor is not very different from that of UO_2 fuel (more so because at end-of-life roughly 80% of the heat produced in UO_2 fuel comes from plutonium fissions). Consequently, the fuel rod behavior codes do not require fundamental modifications. The thermal properties such as melting temperature, thermal conductivity and heat capacity must be modified.^{321–323} Also mechanical properties such as thermal creep and theoretical density require appropriate modifications.

In addition to material properties, a limited number of models must be adapted as well. The first obvious modification pertains to the neutronic model for computing the radial power profile and isotope production. In particular, the resonance capture in ^{240}Pu must be dealt with in a similar way as for ^{238}U , for instance with an empirical radial dependence, and dedicated effective cross-sections for MOX configurations in PWRs and BWRs must be used.³²⁴ As such, one will be able to reproduce the larger flux depression in MOX at beginning of life (BOL), whereas at EOL the higher residual plutonium content at the centre will lead to higher local powers compared to those in UO_2 fuel.

Higher fission gas release at end of life is the only apparent problem mentioned for MOX fuel. It is mainly attributed to the higher linear powers at EOL, in combination with a lower thermal conductivity, rather than differences in microstructure. This is corroborated by the similar threshold for thermal release measured in the Halden Boiling Water reactor. According to these experiments, the Vitanza threshold (cf. Section 2.13.2.3.1) would apply to UO_2 and MOX fuel alike, despite the differences in microstructure. Some experiments, however, indicate that the microstructure of some MOX fuel like MIMAS-MOX could also contribute to the higher release fractions. This has been ascribed to the heterogeneity at the microscopic scale, in particular to

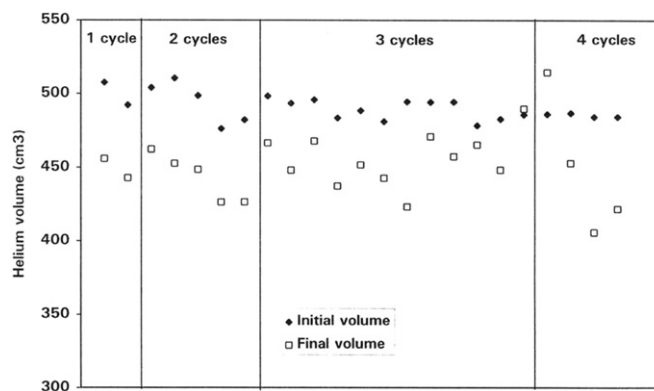


Fig. 28 Helium balance in MOX PWR fuel rods. Reproduced from Blanpain, P., Thibault, X., Pages, J., 1997. Recent results from the in reactor MOX fuel performance in France and improvement program. In: Proceedings of the International Topical Meeting on Light Water Reactor Fuel Performance, March 2–6, 1997, p. 39. Portland, Oregon, USA.

the Pu-enriched agglomerates characterized by a Pu-content around 25% and a size in the order of 50 μm or larger. The burnup and fission product concentrations are therefore roughly three times higher in these agglomerates. Nevertheless, plutonium breeding in the UO_2 matrix surrounding the agglomerates together with fission product recoil tends to reduce the heterogeneity, in particular for agglomerates smaller than 30 μm , which can even “dissolve” in the UO_2 matrix with progress of burnup.^{325–327}

In view of the particularities of fission gas release in MOX summarized above, three different modeling approaches are adopted: some codes do not modify anything since the use of existing UO_2 fuel FGR models for MOX fuel applications have been reported to give satisfactory results.³²⁸ Some codes multiply the fission rate with a “heterogeneity factor” to account for the higher local athermal diffusion coefficient, or simply multiply the diffusion coefficient by a constant factor (~ 1.75). Some others have multiplied the FGR fraction based on the model for UO_2 with a so-called “heterogeneity factor” (~ 1.3). Finally there are stand-alone mechanistic models for FGR in MOX fuel wherein the evolution of the Pu-distribution in agglomerates and U-matrix is computed, the recoil from agglomerates is accounted for and/or the size-distribution of Pu-agglomerates is taken into account.^{329–331} Some of those are used in a fuel performance code such in the COSMOS code.³³² In the ALCYONE code, the heterogeneity of fission gas behavior in MOX is taken into consideration by applying the CARACAS model for UO_2 fuel with modified source local source terms.³³³

Another issue closely related to the FGR in MOX is the He production and release. Helium is generated in fuel matrices by alpha decay of transuranium nuclides, ternary fission and the (n, α) reaction on ^{16}O . The He production is approximately 4–10 times higher in MOX in comparison with UO_2 fuel. Studies on He behavior showed that its diffusion coefficient in UO_2 is several orders of magnitude larger than that of noble gases.³³⁴ Nevertheless, its release from the fuel only occurs if its content is above the solubility limit. The latter strongly depends on temperature and He fill gas pressure,³³⁵ but is still being analysed.³³⁶ The solubility in fresh MOX fuel along with He absorption by pellets could explain why less release is observed in PWR rods (He fill gas pressure > 20 bar) as shown in Fig. 28, whereas significant release is observed in low pre-pressurised BWR MOX rods. This is the reason why some codes do not consider the He release at all (in PWRs), while other codes use a simple (linear) correlation between the He release and fission gas release observed in BWR MOX fuel (Fig. 29).

2.13.4.4 Multi-Scale Modeling

In the previous sections, the main models included in engineering fuel performance codes have been outlined. Every code contains empirical and semi-empirical correlations, which are effective for engineering applications. However, empirical models are only valid within the range of design parameters and reactor conditions covered in the database used for their derivation (or potentially only within more restrictive boundaries as identified by the validation process). Accurately modeling nuclear fuel behavior outside the range of calibration of empirical models (i.e., typically, under abnormal conditions) requires more physically-based models. However, as model validation remains essential, the development of physically-based model does not completely overcome the need for experimental data covering the conditions of interest.

With the preparation of the next generation of nuclear reactors, which relies largely on developments made for fast breeder reactors in the past, so-called advanced fuel types are being considered such as mixed nitrides and carbide fuels. Moreover, following the Fukushima Daiichi nuclear power plant accident in March 2011 there has been an increased research effort into so-called accident-tolerant fuel (ATF) and cladding materials as alternatives to the traditional oxide fuel/ zirconium alloy cladding system. Modeling and simulation of these novel fuel designs requires new experiments to derive data for model development and validation. Also, multi-scale modeling^{337–339} is being used for new fuels in order to partly fill the experimental data gap using calculations for the fundamental physical mechanisms at the atomic and meso-scale (that is, the scale of microstructural features)

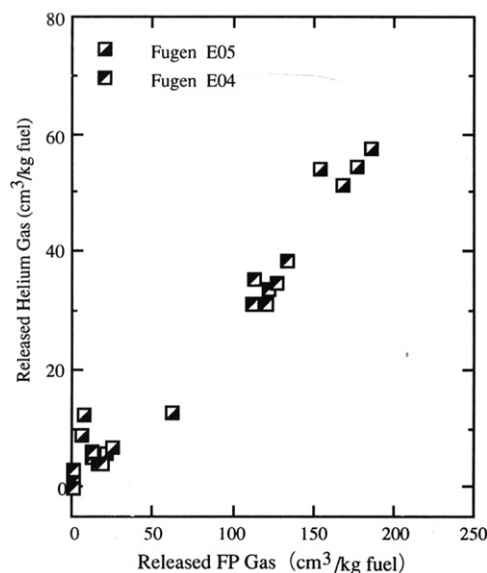


Fig. 29 Comparison between He gas and fission gas release in BWR MOX fuel. Reproduced from Mitsugi, T., Kushida, N., Kikuchi, K., 1997. Behavior of MOX fuel irradiated in a thermal reactor. In: Proceedings of the International Topical Meeting on Light Water Reactor Fuel Performance, March 2–6, 1997, p. 54. Portland, Oregon, USA.

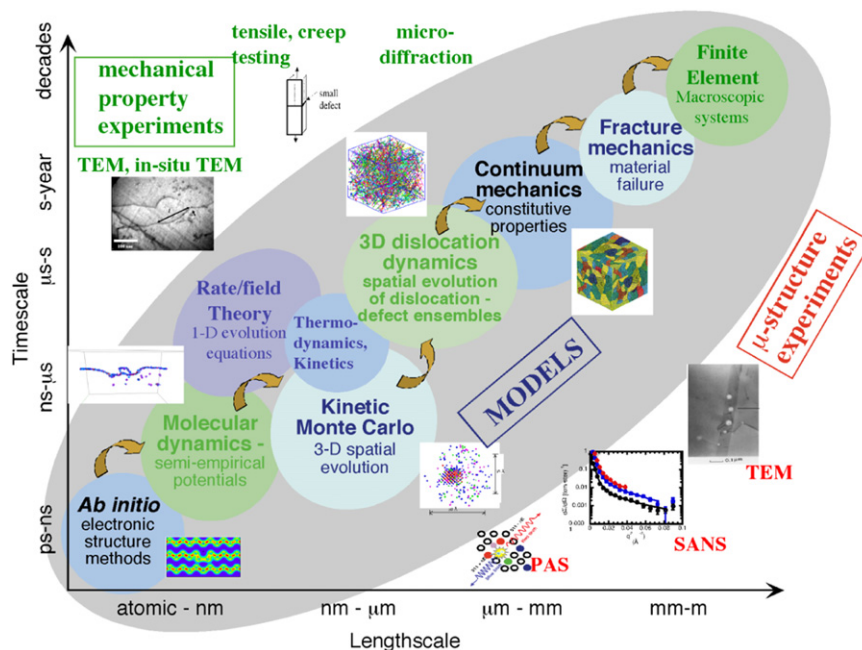


Fig. 30 Illustration of an integrated experimental and computational approach to the multi-time-scale investigation of materials behavior. A number of microstructural characterization techniques important for validating model predictions are also represented: Positron Annihilation Spectroscopy (PAS), Small Angle Neutron Scattering (SANS), Transmission Electron Microscopy (TEM). Reproduced from Wirth, B.D., Odette, G.R., Marian, J., *et al.*, 2004. Multiscale modeling of radiation damage in Fe-based alloys in the fusion environment. *J. Nucl. Mater.* 329–333, 103.

to inform engineering models. In addition to the technological driving force, the approach also offers clear advantages from an academic point of view, as more knowledge is gained about the underlying basic mechanisms. Therefore, the multi-scale approach is also being developed for the existing oxide fuels.^{340,341} The application to standard fuels will also help optimizing the procedure for coupling the various techniques (cf. below), as substantial experimental data are available for validation. Originally, the method has first been developed for metals (e.g., Refs. 342–344). As Illustrated in Fig. 30, the method is hierarchical in principle and based on passing information or parameters, starting from the electronic/atomic up to the larger length and time scales. More in detail, at the electronic scale, density functional theory (DFT) is being used to predict basic properties of materials (for example,

lattice structure, diffusivity of defects) and to provide potential functions (potential energy as a function of separation of two atoms) for use in engineering-scale models.^{67,157} At the molecular scale, molecular dynamics (MD) techniques are being used to predict thermophysical properties and to simulate the effects of irradiation-induced damage on the microstructure.^{67,170} At the meso-scale, dislocation dynamics, cluster dynamics, kinetic Monte Carlo methods, the phase field approach, the representative elementary volume approach, micromechanical (smeared cracking) modeling and new spatially resolved methods are being used to simulate the evolution of the microstructure with time and to determine material properties based on microstructure/property relationships.^{67,197,319,345–348}

The NEA published a state-of-the-art report about multi-scale modeling in nuclear fuels.⁶⁷ It appeared that generally, multi-scale modeling approaches developed to date do not involve integration of calculations at different length scales in the same solve, due to the technical and computational difficulties associated with such a fully coupled scheme. A notable exception is the coupling of the meso-scale code MARMOT³⁴⁹ to the fuel performance code BISON.⁶⁵ This has been demonstrated, e.g., for modeling of UO₂ thermal conductivity.³⁵⁰

2.13.5 Summary and Conclusions

The modeling of nuclear fuel behavior involves many phenomena and disciplines ranging from chemistry, nuclear and solid state physics, metallurgy, ceramics, and applied mechanics. The strong interrelationship between these disciplines, as well as the non-linearity of many of the processes involved, calls for the development of computer codes to describe the global thermo-mechanical behavior of the fuel elements.

After years of development, the fuel performance codes have become standard tools for safety authorities, fuel designers and nuclear fuel researchers. The various benchmarks for fuel rod performance codes organized by the IAEA^{273,317,318,351} revealed that in general and under normal operating conditions

- Temperatures can be predicted with a relative error of the order to 10%;
- The clad elongation as well as the cladding diametrical deformation are predicted with a relative error of about 30% (although based on less data);
- The ratio of predicted to measured values for fission gas release is generally within a factor of 2.

Most difficulties stem from

- Uncertainties in input values (fabrication and irradiation parameters);
- The stochastic nature of pellet cracking, and its consequences on the thermal (uncertainty on the gap size, especially at beginning-of-life) as well as on the mechanical analysis (validity of compatibility and constitutive equations). In addition, crack-healing is difficult to model properly;
- A lack of direct measurements (e.g., parameters such as fission gas diffusion coefficients and resolution rate coefficients) or large scatter in the experimental data;
- A limited set of experimental data available in the open literature for new materials that are being introduced for reaching higher discharge burnups (e.g., new cladding material properties), and even less for enhanced accident tolerant materials that are under investigation in the wake of the accident at Fukushima.

It should be underlined that some specific fuel performance codes (typically developed by fuel vendors) have been fine-tuned with a larger data base but for a particular type of fuel and therefore provide more accurate predictions for that type of fuel.

Multi-dimensional (2D, 3D) fuel performance codes are complementary to the standard (1.5D) codes and offer an improved description of specific phenomena such as pellet-cladding interaction (bamboo effect), or cladding ballooning in presence of azimuthal variations, or fabrication defects such as missing pellet surfaces. However, multi-dimensional fuel calculations involve a higher computation time and despite superior computational resources available nowadays, to the best of the authors' knowledge, 3D analyses of full-length fuel rods for realistic irradiation histories are still very challenging. Arguably, however, the added value of multi-dimensional representations is limited to the analysis of specific multi-dimensional effects such as clad ridging, and 1.5D codes are adequate for situations where the corresponding symmetry assumptions are valid or when full-core simulations are required in the frame of licensing. They thus complement each other very well. Nevertheless, difficulties listed above are not associated with the geometrical representation and hold for both traditional and multi-dimensional codes.

In view of the tendency to increase the discharge burnup of fuel rods, modifications of the fuel performance codes to allow for high-burnup effects are needed and have been made, or in some cases still need to be implemented. For instance, regarding the radial heat transfer in the fuel rod, the chemical bonding layer between the fuel and the cladding at high burnup levels eliminates progressively the effect of surface roughness on the heat transfer in the gap, decreasing the temperature jump induced by gap gas.

With respect to the mechanical properties, various experimental techniques indicate a softening of the fuel when the high burnup structure is established.^{310,311}

As far as the fission gas behavior is concerned, there is a consensus that most fission gas remains in the HBS,¹⁵² whereas earlier it was believed to be responsible for the observed increase in fission gas release beyond average burnup levels of 50 MWd/kgHM.

Despite the relatively benign effects of the HBS on the thermo-mechanical behavior of the fuel rod under normal operating conditions, the HBS still requires attention for modeling the transient behavior of nuclear fuel.^{241,352} In the event of a Reactivity Initiated Accident, for example, it is important to know how much gas resides in porosity in terms of a potential FGR and fuel fragmentation.²⁵⁷ Recent experimental studies with advanced methods (e.g., Focused Ion Beam examination) in high burnup fuel contribute to the quantitative and qualitative description of the gas distribution in the HBS across the pellets.^{303,304}

Modeling the behavior of MOX fuel for LWRs has also become a routine task in some countries as it became a mature industrial product. Generally, the fission gas release fraction at end-of-life is higher in comparison with that of UO₂ fuel. The difference in power history and the lower thermal conductivity of MOX have been identified as the main causes, although research is still ongoing to assess the role of the heterogeneous microstructure in (Micronized MASTer blend, or MIMAS-type) MOX.

Most mechanistic models for FGR for MOX available in the open literature do not account for the evolved microstructure, which apart from the Pu-rich agglomerates and U-rich matrix may also contain a Pu-rich coating layer at grain boundaries. A first attempt was made in the COSMOS code,³³² and more recently in the CARACAS model in the ALCYONE code.³³³ Both take into consideration the initial heterogeneous microstructure via the local variations of fission density and fission product source term in the model developed for UO₂ fuel.

As regards helium behavior, the fractional release observed in MOX fuel rods loaded in BWRs is generally behavior taken to be proportional to the FGR fraction. In contrast, the absence of He release observed in PWR MOX has been ascribed to the higher He solubility due to the elevated fill gas pressure. With the long storage times of spent fuel, the issue of He release will gain importance in the codes. Nevertheless, more experimental data are needed in the open literature for MOX fuel as pointed out in the ongoing INSPYRE project.^{334,336}

In order to complement the time-consuming and costly experiments for developing and optimizing advanced fuels for the next generation of reactors, multi-scale modeling is being launched across the globe. Yet, despite promising initial results,^{67,197,345} and a better understanding obtained for the basic phenomena, it is still too ambitious to conceive a fuel performance code based solely on fundamental computations. There are limitations to each individual technique in terms of temperature range, space –and time-scale, in addition to the stochastic nature of several phenomena (e.g., fuel cracking) or the strong relationship between various phenomena entailing high non-linearities.

Until recently, fuel performance codes were either developed for simulating the fuel rod behavior under normal operating conditions and mild transients, or for simulating accident behavior. At present there is a tendency to widen the scope of both types of codes so as to simulate the fuel rod behavior under all conditions with a single code in a more consistent manner, and a few codes have already successfully demonstrated the applicability for this extended range of conditions.¹

Finally, it remains important that all fuel performance codes will be further benchmarked with peer-reviewed experimental data, such as those proposed in the framework of international benchmarks organized by the OECD/NEA and the IAEA, especially for design basis accidents and enhanced accident tolerant fuels.

See also: 2.10 Behavior of LWR Fuel During Loss-of-Coolant Accidents. 2.12 Behavior of Fast Reactor Fuel During Transient and Accident Conditions. 2.14 Modeling of Pellet Cladding Interaction. 6.09 Ceramic Coatings for Fusion Reactors

References

1. Van Uffelen, P., Hales, J., Li, W., Rossiter, G., Williamson, R., 2019. A review of fuel performance modeling. *J. Nucl. Mater.* 516, 373.
2. Harriague, S., Savino, E.J., Coroli, G., Basombrio, F.G., Sarmiento, G.S., 1980. Theoretical fuel element modeling at CNEA. *Nucl. Eng. Des.* 56, 83.
3. Harriague, S., Coroli, G., Savino, E.J., 1980. BACO (Barra Combustible), a computer code for simulating a reactor fuel rod performance. *Nucl. Eng. Des.* 56, 91.
4. Denis, A., Soba, A., 2003. Simulation of pellet-cladding thermomechanical interaction and fission gas release. *Nucl. Eng. Des.* 223, 211.
5. Soba, A., Denis, A., 2008. Model of fracture for the Zry cladding of nuclear fuel rods included in the code DIONISIO 1.0. *Nucl. Eng. Des.* 238, 3292.
6. Soba, A., Denis, A., 2015. DIONISIO 2.0: New version of the code for simulating a whole nuclear fuel rod under extended irradiation. *Nucl. Eng. Des.* 292, 213.
7. Godesar, R., Guyette, M., Hoppe, N., 1969. COMETHE II, Computer code for the mechanical and thermal analysis of a fuel pin. In: *Proceedings of the Reaktortagung des Deutschen Atomforums*, Frankfurt, Germany: Deutsches Atomforum.
8. Dewandeleer, J., Godesar, R., Hoppe, N., Mayer, H., Müller, E.M., 1970. Oxide fuel pin behaviour: Comparison of experimental results with predictions by the COMETHEII C code. In: *Proceedings of the International Meeting Fast Reactor Fuel and Fuel Elements*, p. 29. Kerntechnische gesellschaft im Deutsches Atomforum: Karlsruhe, Germany.
9. Godesar, R., Guyette, M., Hoppe, N., 1970. Comethe II-A computer code for predicting the mechanical and thermal behavior of a fuel pin. *Nucl. Appl. Technol.* 9, 205.
10. Lemehov, S.E., Govers, K., Verwerf, M., 2003. Modeling non-standard mixed oxide fuels with the mechanistic code MACROS: Neutronic and heterogeneity effects. In: *Proceedings of the IAEA Technical Committee Meeting on Advanced Fuel Pellet Materials and Designs for Water Cooled Reactors*, IAEA-TECDOC-1416, p. 235. Brussels, Belgium: IAEA.
11. Yu, H., Tian, W., Yang, Z., Su, G.H., Qiu, S., 2012. Development of fuel ROD behavior analysis code (FROBA) and its application to AP1000. *Ann. Nucl. Energy* 50, 8.
12. Han, Z., Ji, S., Zhang, Y., 2014. Validation and application of fuel transient performance analysis code FTPAC. *At. Energy Sci. Technol* 48, 389.
13. Zhou, Y., Chen, P., Zhang, L., *et al.*, 2014. Modeling of PWR fuel rod irradiation behaviour. *Nucl. Power Eng.* 35, 200.
14. Jin, X., Wei, X., Liu, X., Deng, Y., 2016. JASMINE: A fuel rod thermal-mechanical performance code. In: *Proceedings of the Top Fuel 2016*, September 11–16, 2016, p. 601 Boise, ID, USA: ANS.
15. Wei, X., Jin, X., Deng, Y., Zhang, G., Fu, X., 2017. Modeling of fuel rod behavior and recent advances of the JASMINE code. In: *Proceedings of the 25th International Conference on Nuclear Engineering (ICONE25)*, p. 67144. Shanghai, P.R. China.
16. Pazdera, F., Valach, M., 1982. User's Guide for PIN: A Computer Program for the Calculation of the Thermal Behaviour of an Oxide Fuel Rod, UJV-6124T. Czech Republic: UJV.

17. Strijov, P.N., Pazdera, F., Yakovlev, V.V., Dubrovin, K., 1988. The improved version of the PIN code and its verification. In: Proceedings of the IAEA Technical Committee Meeting on Water Reactor Fuel Element Computer Modeling in Steady-State, Transient and Accident Conditions, September 19–22, 1988. Preston, England.
18. Struzik, C., Moyne, M., Piron, J.-P., 1997. High burn-up modeling of UO_2 and MOX fuel with METEOR/TRANSURANUS Version 1.5. In: Proceedings of the ANS Conference, p. 126. Portland, Oregon, USA.
19. Marelle, V., Goldbronn, P., Bernaud, S., *et al.*, 2016. New developments in ALCYONE 2.0 fuel performance code. In: Proceedings of the Top Fuel 2016, September 11–15, 2016, p. 643. Boise, ID, USA: ANS.
20. Michel, B., Nonon, C., Sercombe, J., Michel, F., Marelle, V., 2013. Simulation of pellet-cladding interaction with the PLEIADES fuel performance software environment. Nucl. Technol. 182, 124.
21. Bentejac, F., Hourdequin, N., 2004. Toutatis: An application of the CAST3M finite element code for PCI three-dimensional modeling. In: Proceedings of the International Seminar on Pellet-Clad Interaction in Water Reactor Fuels, March 9–11, 2004. Aix-en-Provence, France.
22. Garnier, C., Sontheimer, F., Mailhé, P., *et al.*, 2009. Validation of advanced fuel performance COPENIC3 code on AREVA global database up to 100 GWd/tHM. In: Proceedings of the Top Fuel 2009, p. 742. Paris, France.
23. Viouard, N., Bessiron, V., Garnier, C., *et al.*, 2012. GALILEO AREVA's advanced fuel rod performance code and associated realistic methodology. In: Proceedings of the Top Fuel 2012, September 2–6, 2012, p. 87. Manchester, United Kingdom.
24. Thevenin, P., Masson, R., Baron, D., Petitprez, B., Plancq, D., 2006. CYRANO3: The industrial PLEIADES fuel performance code for EDF PWR studies. In: Proceedings of the International Meeting on LWR Fuel Performance, Top Fuel, October 22–27, 2006, p. 550. Salamanca, Spain: ENS.
25. Moal, A., Georgenthum, V., Marchand, O., 2014. SCANAIR: A transient fuel performance code, Part one: General modeling description. Nucl. Eng. Des. 280, 150.
26. Gross, H., Urban, P., Fenzlein, C., Technological and licensing challenges for high burnup fuel. In: Proceedings of the Technical Committee Meeting: Technical and Economic Limits to Fuel Burnup Extension, TECDOC-1299, November 15–19, 1999, p. 101. San Carlos de Bariloche, Argentina: IAEA.
27. OECD-NEA, 2010. State-of-the-Art Report: Nuclear Fuel Behaviour Under Reactivity-Initiated Accident (RIA) Conditions, NEA/CSNI/R(2010)1, Paris, France: OECD-NEA.
28. Van Uffelen, P., Schubert, A., van de Laar, J., *et al.*, 2015. Developments for TRANSURANUS in the frame of FUMAC In: Proceedings of the 11th International Conference on WWER Fuel Performance, Modeling and Experimental Support, vol. 1, September 26–October 3, 2015, p. 267. Varna, Bulgaria: NRNE.
29. Lassmann, K., 1992. TRANSURANUS: A fuel rod analysis code ready for use. J. Nucl. Mater. 188, 295.
30. Schubert, A., Van Uffelen, P., van de Laar, J., Walker, C.T., Haack, W., 2008. Extension of the TRANSURANUS burn-up model. J. Nucl. Mater. 376, 1.
31. Marcello, V.D., Schubert, A., van de Laar, J., Uffelen, P.V., 2014. The TRANSURANUS mechanical model for large strain analysis. Nucl. Eng. Des. 276, 19.
32. Gádó, J., Grigera, Á., Kulacsy, K., 2018. The fuel behaviour code FUROM and its high burn-up simulation capabilities. Nucl. Eng. Des. 327, 274.
33. IAEA, 1998. Report of the Co-Ordinated Research Project on Fuel Modeling at Extended Burnup – FUMEX, TECDOC-998. Vienna, Austria: IAEA.
34. Sah, D.N., Venkatesh, D., 1984. A brief description of PROFESS and its submodels. In: Proceedings of the IAEA Specialists Meeting on Water Reactor Fuel Element Computer Modeling, IWGFPT/19, April 9–13, 1984, p. 237. Bowness-on-Windermere, UK: IAEA.
35. Killeen, J., 2012. Fuel modeling at extended burnup (FUMEX-II). Report of a Coordinated Research Project, TECDOC-1687. Vienna, Austria: IAEA.
36. Kinoshita, M., 1993. Development of LWR fuel performance analysis codes. J. Nucl. Sci. Technol. 30, 1.
37. Suzuki, M., 2013. Light Water Reactor Fuel Analysis Code FEMAXI-7. Model and Structure. Nihon Genshiryoku Kenkyu Kaihatsu Kiko.
38. Suzuki, M., Fuketa, T., 2006. Analysis of pellet-clad mechanical interaction process of high-burnup PWR fuel rods by RANNS code in reactivity-initiated accident conditions. Nucl. Technol. 155, 282.
39. Udagawa, Y., Suzuki, M., Amaya, M., 2014. Model Development of Light Water Reactor Fuel Analysis Code RANNS for Reactivity-Initiated Accident Conditions, JAEA-Data/Code 2014-025.
40. Wu, H., Udagawa, Y., Narukawa, T., Amaya, M., 2016. Validation of updated RANNS with effect of oxygen-dissolved metallic zircaloy-4 under LOCA quench condition. Nucl. Eng. Des. 300, 249.
41. Koo, Y.H., Lee, B.H., Sohn, D.S., 1998. COSMOS: A computer code for the analysis of LWR UO_2 and MOX fuel rods. J. Korean Nucl. Soc. 30, 541.
42. Koo, Y.H., Lee, B.H., Sohn, D.S., 1999. COSMOS: A computer code to analyze LWR UO_2 and MOX fuel to high burn-up. Ann. Nucl. Energy 26, 47.
43. Lee, C.B., Yang, Y.S., Kim, Y.M., *et al.*, 2004. High burnup UO_2 fuel rod performance code INFRA. In: Proceedings of the International Meeting on LWR Fuel Performance, September, 19–22, 2004. Orlando, Florida, USA: ANS.
44. Yang, Y., Lee, C., Kim, D., Kim, Y., Jung, Y., 2003. Verification of INFRA code by using re-instrumented fuel test results. In: Proceedings of the International Conference on WWER Fuel Performance, Modeling and Experimental Support, September 29–October 3, 2003, p. 442. Varna, Bulgaria: INRNE.
45. Medvedev, A.V., Bogatyr, S., Kouznetsov, V., *et al.*, 1999. Modeling of VVER fuel rod temperature condition at high burnups in START-3 code. In: Proceedings of the Third International Seminar on WWER Fuel Performance, Modeling and Experimental Support, October 4–8, 1999. Pamporovo, Bulgaria: INRNE.
46. Bibilashvili, Y.K., Medvedev, A.V., Khostov, G.A., Bogatyr, S.M., Korystine, L.V., 2000. Development of the fission gas behaviour model in the START-3 code and its experimental support. In: Proceedings of the International Seminar on Fission Gas Behaviour in Water Reactor Fuels, September 26–29, 2000, p. 407. Cadarache, France: OECD-NEA.
47. Khvostov, G., Novikov, V., Medvedev, A., Bogatyr, S., 2004. High burn-up structure in LWR fuels: Experience of modeling by the START-3 code. In: Proceedings of the International Workshop on the High Burn-up Structure in Nuclear Fuels, June 28–30, 2004, Karlsruhe, Germany: EC-JRC.
48. Bibilashvili, Y.K., Sokolov, N.B., Salatov, A., *et al.*, 1995. RAPTA-5 code: Modeling behaviour of VVER-type fuel rods in design basis accident conditions verification calculations. In: Proceedings of the Technical Committee Meeting on Behaviour of LWR Core Materials Under Accident Conditions, IAEA-TECDOC-921, October 9–13, 1995, p. 139. Dimitrovgrad, Russian Federation.
49. Kurchatov, S.Y., Likhanskii, V.V., Sorokin, A.A., Khoruzhii, O.V., 2002. RTOP-code simulation of the radial distribution of heat release and plutonium isotope accumulation in high burn-up oxide fuel. At. Energy 92, 349.
50. Likhanskii, V.V., Evdokimov, I.A., Zborovskii, V., Sorokin, A., Tokarev, S. Simulation of the power profile in gadolinium-doped fuel rods with the fuel performance code RTOP. In: Proceedings of the WWER Fuel Performance, Modeling and Experimental Support, p. 556. Golden Sands Resort, Bulgaria: Bulgarian Academy of Sciences.
51. Veshchunov, M., Boldyrev, A., Ozrin, V., *et al.*, Development of the mechanistic fuel performance and safety code SFPR using the multi-scale approach. In: Proceedings of the Materials Modeling and Simulation for Nuclear Fuels (MMSNF) Workshop, October 14–16, 2013. Chicago, Illinois, USA: ANL.
52. Veshchunov, M.S., Boldyrev, A.V., Ozrin, V.D., Shestak, V.E., Tarasov, V.I., 2011. A new mechanistic code SFPR for modeling of single fuel rod performance under various regimes of LWR operation. Nucl. Eng. Des. 241, 2822.
53. Zhou, G., 2007. STAV7 Model Description, BU 97-091, Rev 3, p. 217. Westinghouse Electric Sweden AB.
54. Jernkvist, L.O., Limbäck, M., 1995. Analysis of fuel rod behaviour under LOCA using the STAV-T fuel performance code. In: Proceedings of the 13th International Conference on Structural Mechanics in Reactor Technology (SMiRT 13), August 13–18, 1995, p. 45. Porto Alegre, Brazil: IASMiRT.
55. Jackson, P.A., Turnbull, J.A., White, R.J., 1990. ENIGMA fuel performance code. Nucl. Energy 29, 107.
56. White, R., 1991. Capabilities and validation of the ENIGMA fuel performance code. In: Proceedings of the International Topical Meeting on LWR Fuel Performance, p. 919. Avignon, France.
57. Rossiter, G., 2011. Development of the ENIGMA fuel performance code for whole core analysis and dry storage assessments. Nucl. Eng. Technol. 43, 489.
58. Geelhood, K.J., Luscher, W.G., Raynaud, P.A., Porter, I.E., 2015. FRAPCON-4.0: A Computer Code for the Calculation of Steady-State, Thermal-Mechanical Behavior of Oxide Fuel Rods for High Burnup, PNNL-19400, vol.1, Rev 2. Pacific Northwest National Laboratory.
59. Geelhood, K.J., Luscher, W.G., Cuta, J.M., Porter, I.A., 2016. FRAPTRAN-2.0: A Computer Code for the Transient Analysis of Oxide Fuel Rods, PNNL-19400, vol.1, Rev 2. Pacific Northwest National Laboratory.

60. Porter, I.E., 2017. FAST: The merger of NRC's fuel performance codes FRAPCON and FRAPTRAN for scoping and regulatory decision making. In: Proceedings of the 2017 Water Reactor Fuel Performance Meeting, September, 10–14, 2017. Jeju Island, Korea: KNS.
61. Merckx, K.R., 1977. RODEX: Fuel Rod Thermal Mechanical Response Evaluation Code. XN-76-8-(NP), TRN: 78-008352. Richland, Wash: Exxon Nuclear Co., Inc.
62. Rashid, Y., Dunham, R., Montgomery, R., 2004. Fuel analysis and licensing code: FALCON MOD01. In: Yagnik, S. (Ed.), *Theoretical and Numerical Bases 1*. Palo Alto, CA: Electric Power Research Institute. (1011307).
63. Rashid, J., Montgomery, R., Yagnik, S., Yang, R., 2003. Behavioral modeling of LWR fuel as represented in the FALCON code. In: Proceedings of the Workshop on Materials Modeling and Simulations for Nuclear Fuel (MMSNF). New Orleans, USA.
64. Yagnik, S.K., 1998. Overview of EPRI fuel performance code FALCON. In: Proceedings of the International Seminar on Thermal Performance of High Burn-Up LWR Fuel, March 3–6, 1998, p. 267. Cadarache, France: OECD-NEA.
65. Williamson, R.L., Hales, J.D., Novascone, S.R., *et al.*, 2012. Multidimensional multiphysics simulation of nuclear fuel behavior. *J. Nucl. Mater.* 423, 149.
66. Long, Y., Kersting, P.J., Linsuain, O., Rumschlag, D.T., Oelrich Jr., R.L., 2016. Advances in Westinghouse fuel rod design technology (PAD5). In: Proceedings of the Top Fuel 2016, September 11–15, 2016, p. 921. Boise, ID, USA: ANS.
67. OECD-NEA, 2015. State-of-the-Art Report on Multi-Scale Modeling of Nuclear Fuels, NEA/NSC/R/(2015)5. Paris: OECD-NEA, p. 380.
68. Lassmann, K., Schubert, A., van de Laar, J., Van Uffelen, P., 2015. The 'Fuel Rod Analysis ToolBox': A general program for preparing the input of a fuel rod performance code. *Ann. Nucl. Energy* 81, 332.
69. Baurens, B., Sercombe, J., Riglet-Martial, C., *et al.*, 2014. 3D thermo-chemical-mechanical simulation of power ramps with ALCYONE fuel code. *J. Nucl. Mater.* 452, 578.
70. Williamson, R.L., Gamble, K.A., Perez, D.M., *et al.*, 2016. Validating the BISON fuel performance code to integral LWR experiments. *Nucl. Eng. Des.* 301, 232.
71. Olander, D.R., 1976. Fundamental aspects of nuclear reactor fuel elements. In Technical Information Center – Energy Research and Development Administration, TID-26711-P1. Berkeley: University of California.
72. Bailly, H., Ménéssier, D., Prunier, C., 1999. *The Nuclear Fuel of Pressurized Water Reactors and Fast Reactors: Design and Behaviour*. Paris: Lavoisier Publishing.
73. Lassmann, K., Van Uffelen, P., 2004. *The Structure of Fuel Rod Codes*. JRC Publications, European Commission. (EUR 21400 EN).
74. Lassmann, K., Hohlefeld, F., 1986. Überarbeitung des URGAP Modells zur Berechnung des Wärmeübergangs zwischen Brennstoff und Hülle. European Commission. (EUR 10756 DE).
75. Lassmann, K., Hohlefeld, F., 1987. The Revised URGAP-Model to Describe the GAP Conductance Between Fuel and Cladding. *Nucl. Eng. Des.* 103, 215.
76. Centikale, T.N., Fishenden, M., 1951. Thermal conductance of metal surfaces in contact. In: Proceedings of the International Conference on Heat Transfer, p. 271. London, UK.
77. Ross, A.M., Stoute, R.L., 1962. Heat Transfer Coefficient Between UO_2 and Zircaloy-2. Chalk River, Ontario: AECL, p. 73. (AECL-1552).
78. Herranz, L.E., Tigras, A., 2010. Solid-solid conductance in nuclear fuel: An assessment of it in-code models performance. *Prog. Nucl. Energy* 52, 435.
79. Charles, M., Bruet, M., 1984. Gap conductance in a fuel rod: Modeling of the FURET and CONTACT results. In: Proceedings of the IAEA Specialists Meeting on Water Reactor Fuel Element Performance Modeling, IWGFPT/19, April, 9–13, 1984, p. 388. Bowness-on-Windermere, UK: IAEA.
80. Mac Donald, P.E., Weisman, J., 1976. Effect of pellet cracking on light water reactor fuel temperatures. *Nucl. Technol.* 31, 357.
81. White, R.J., 2007. Gap-Conductance Analysis of the Halden Thermal Performance Database, HWR-886. Halden: OECD Halden Reactor Project.
82. Kjaerheim, G., Rolstad, E., 1967. In-pile determination of UO_2 thermal conductivity, density effects and gap conductance. Halden Project Report, HPR-80. OECD.
83. Palmer, I.D., Hesketh, K.W., Jackson, P.A., 1982. A model for predicting the radial power profile in a fuel pin. In: Proceedings of the IAEA Specialists' Meeting on Water Reactor Fuel Element Performance Computer Modeling, p. 347. Preston, UK: IAEA.
84. Botazzoli, P., Luzzi, L., Brémier, S., *et al.*, 2011. Extension and validation of the TRANSURANUS burn-up model for helium production in high burn-up LWR fuels. *J. Nucl. Mater.* 419, 329.
85. Lee, C.B., Kim, B.G., Song, J.S., Bang, J.G., Jung, Y.H., 2000. RAPID model to predict radial burnup distribution in LWR UO_2 fuel. *J. Nucl. Mater.* 282, 196.
86. Lemehov, S., Nakamura, J., Suzuki, M., 2001. Pluton: A three-group model for the radial distribution of plutonium, burnup, and power profiles in highly irradiated LWR fuel rods. *Nucl. Technol.* 133, 153.
87. Staicu, D., 2012. Thermal properties of irradiated UO_2 and MOX. In: Konings, R.J.M. (Ed.), *Comprehensive Nuclear Materials*, vol. 2. Elsevier Ltd, pp. 149–172.
88. MacEwan, J.R., Stoute, R.L., Notley, M.J.F., 1967. Effect of porosity on the thermal conductivity of UO_2 . *J. Nucl. Mater.* 24, 109.
89. Lassmann, K., 1980. The structure of fuel element codes. *Nucl. Eng. Des.* 57, 17.
90. Lassmann, K., 1987. A fast and simple iteration scheme for the temperature calculation in a fuel rod. *Nucl. Eng. Des.* 103, 211.
91. Suzuki, M., Saitou, H., 2006. Light Water Reactor Fuel Analysis Code FEMAXI-6 (Ver.1). JAEA-Data/Code 2005-003. JAEA.
92. Geelhood, K.J., Luscher, W.G., 2014. FRAPCON-3: A Computer Code for the Calculation of Steady-State, Thermal-Mechanical Behavior of Oxide Fuel Rods for High Burnup, NUREG/CR-7022. Office of Nuclear Regulatory Research.
93. Lanning, D.D., Beyer, C.E., Painter, C.L., 1996. New high burnup fuel models for NRC's Licensing Audit code, FRAPCON, NUREG/CP-0149. p. 141.
94. Lanning, D.D., Beyer, C.E., Painter, C.L., 1997. FRAPCON-3: Modifications to Fuel Rod Material Properties and Performance Models for High-Burnup Application, NUREG/CR-6534, PNNL-11513. Pacific Northwest National Laboratory.
95. Sercombe, J., Michel, B., Thouvenin, G., *et al.*, 2009. Multi-dimensional modeling of PCMI during base irradiation and ramp testing with ALCYONE V1.1 (Paper 2096). In: Proceedings of the Top Fuel 2009, September 6–10, 2009, Paris, France: ENS.
96. Struzik, C., Marelle, V., 2012. Validation of the fuel performance CEA code ALCYONE, scheme 1D, on extensive data base. In: Proceedings of the Top Fuel 2012, September 2–6, 2012. Manchester, United Kingdom: ENS.
97. Hales, J.D., Williamson, R.L., Novascone, S.R., *et al.*, 2016. BISON Theory Manual: The Equations behind Nuclear Fuel Analysis, INL/EXT-13-29930. Idaho Falls, ID: Idaho National Laboratory, p. 156. (Rev. 3).
98. Spino, J., Rest, J., Goll, W., Walker, C.T., 2005. Matrix swelling rate and cavity volume balance of UO_2 fuels at high burn-up. *J. Nucl. Mater.* 131.
99. Middleburgh, S.C., Grimes, R.W., Desai, K.H., *et al.*, 2012. Swelling due to fission products and additives dissolved within the uranium dioxide lattice. *J. Nucl. Mater.* 427, 359.
100. Marchetti, M., Laux, D., Fongaro, L., *et al.*, 2017. Physical and mechanical characterization of irradiated uranium dioxide with a broad burnup range and different dopants using acoustic microscopy. *J. Nucl. Mater.* 494, 322.
101. Assmann, H., Stehle, H., 1978. Thermal and in-reactor densification of UO_2 mechanisms and experiments. *Nucl. Eng. Des.* 48, 49.
102. Suk, H.C., Wang, W., Kim, B.G., Kim, K.S., Heo, Y.H., 1992. Improvement of ELESIM-CANDU fuel performance analysis code. In: Proceedings of the Technical Committee Meeting on Fission Gas Release and Fuel Chemistry Related to Extended Burnup, TECDOC-697, p. 193. Pembroke, Ontario, Canada: IAEA.
103. Jackson, P.A., Turnbull, J.A., White, R.J., 1988. A description of the ENIGMA fuel performance code. In: Proceedings of the Technical Committee Meeting on Water Reactor Fuel Element Computer Modeling in Steady State, Transient and Accident Conditions, IWGFPT/32. p. 28. Preston, UK: IAEA.
104. White, R.J., 2001. Measurements of Pellet and Clad Dimensional Changes in the Halden Reactor, HWR-678. Halden: OECD Halden Reactor Project.
105. Cunningham, M.E., Beyer, C.E., Medvedev, P.G., Berna, G.A., Scott, H., 2001. FRAPTRAN: A computer code for the transient analysis of oxide fuel rods. NUREG/CR-6739, PNNL-13576.
106. Garcia, P., Struzik, C., Agard, M., Louche, V., 2002. Mono-dimensional mechanical modeling of fuel rods under normal and off-normal operating conditions. *Nucl. Eng. Des.* 216, 183.
107. Massih, A.R., Jerknvist, L.O. Mechanics and PCMI. In: Proceedings of the Chapter 6 in Lecture Notes of the OECD – HRP Summer School on Fuel Behaviour Modeling, August 31–September 3. Halden, Norway.
108. Owen, D.R.J., Hinton, E., 1980. *Finite Elements in Plasticity: Theory and Practise*. Swansea: Pineridge Press Limited.

109. Oguma, M., 1983. Cracking and relocation behavior of nuclear fuel pellets during rise to power. Nucl. Eng. Des. 76, 35.
110. Barani, T., Pizzocri, D., Pastore, G., Luzzi, L., Hales, J., 2019. Isotropic softening model for fuel cracking in BISON. Nucl. Eng. Des. 342, 257.
111. Berna, G.A., Beyer, C.E., Davis, K.L., Lanning, D.D., 1997. FRAPCON-3: A Computer Code for the Calculation of Steady-State. Thermal-Mechanical Behaviour of Oxide Fuel Rods for High Burnup, NUREG/CR-6534, PNNL-11513.
112. Lassmann, K., Schubert, A., Van Uffelen, P., van de Laar, J., 2005. TRANSURANUS Handbook.
113. Van Uffelen, P., Sheindlin, M., Rondinella, V., Ronchi, C., 1997. On the relations between the fission gas behaviour and the pellet-cladding mechanical interaction in LWR fuel rods. In: Proceedings of the Pellet-Clad Interaction in Water Reactor Fuels (PCI-2004), March 9–11, 2004. Aix en Provence, France: CEA Cadarache/DEN/DEC.
114. Jankus, V.Z., Weeks, R.W., 1972. LIFE-II – A computer analysis of fast-reactor-fuel-element behaviour as a function of reactor operating history. Nucl. Eng. Des. 18, 83.
115. Hoppe, N., 1980. Improvements to COMETHE III-J fuel rod modeling code. Nucl. Eng. Des. 56, 123.
116. Newman, C., Hansen, G., Gaston, D., 2009. Three dimensional coupled simulation of thermomechanics, heat, and oxygen diffusion in UO_2 nuclear fuel rods. J. Nucl. Mater. 293, 6.
117. Spencer, B.W., Williamson, R.L., Stafford, D.S., *et al.*, 2016. 3D modeling of missing pellet surface defects in BWR fuel. Nucl. Eng. Des. 307, 155.
118. Sorokin, A.A., Likhanskii, V.V., Zborovskii, V.G., *et al.*, 2011. 3D simulation model of pellet-cladding mechanical interaction in RTOP code. In: Proceedings of the WWER Fuel Performance, Modeling and Experimental Support, September 17–24, 2011, p. 495. Albená, Bulgaria: INRNE.
119. Demarco, G.L., Marino, A.C., 2011. 3D finite elements modeling for design and performance analysis of UO_2 pellets. Sci. Technol. Nucl. Install 2011.
120. Michel, B., Sercombe, J., Thouvenin, G., Chatelet, R., 2008. 3D fuel cracking modeling in pellet cladding mechanical interaction. Eng. Fract. Mech. 75, 3581.
121. Cox, B., 1990. Pellet cladding interaction (PCI) failures of zirconium alloy cladding – A review. J. Nucl. Mater. 172, 249.
122. Piro, M., Sunderland, D., Livingstone, S., *et al.*, 2017. A review of pellet-clad interaction behavior in zirconium alloy fuel cladding. In: Hashmi, S. (Ed.), Reference Module in Materials Science and Materials Engineering. Oxford: Elsevier, p. 1.
123. Schire, D., Grapengiesser, B., Hallstadius, L., *et al.*, Secondary defect behaviour in ABB BWR fuel. In: Proceedings of the Topical Meeting on LWR Fuel Performance, April 17–21, p. 398. American Nuclear Society: West Palm Beach, Florida, USA.
124. Harbottle, J.E., Kennard, M.W., Sunderland, D.J., Strasser, A.A. The behaviour of defective BWR barrier and non-barrier fuel. In: Proceedings of the Topical Meeting on LWR Fuel Performance, April 17–21, p. 391. American Nuclear Society: West Palm Beach, Florida, USA.
125. Van Swam, L.F., Strasser, A.A., Cook, J.D., Burger, J.M., 1997. Behaviour of zircaloy-4 and zirconium liner zircaloy-4 cladding at high burnup. In: Proceedings of the International Topical Meeting on LWR Fuel Performance, March 2–5, 1997, p. 421. Portland, Oregon, USA: ANS.
126. Karlsson, J., Lysell, G., Pettersson, H., Rönnerberg, G., 2004. In-pile testing of liner cladding an pellet performance in failed fuel rods. In: Proceedings of International Meeting on LWR Fuel Performance, September 19–22, 2004, Paper 1046. Orlando, Florida, USA.
127. Garner, N.L., Rentmeister, T., Lippert, H.-J., Mollard, P., 2007. Upgraded fuel assemblies for BWRs. In: Proceedings of the International LWR Fuel Performance Meeting, September 30–October 3, 2007, Paper 1091, San Francisco, California, USA.
128. Hoffmann, P.B., Dewes, P. Post-irradiation examination and ramp testing of fuel rods with Fe-enhanced Zr liner cladding at high burnup. In: Proceedings of the International Meeting on LWR Fuel Performance, September 19–22, Paper 1059. Orlando, Florida, USA.
129. Sihver, L., Hallstadius, L., Wikmark, G. Recent ABB BWR failure experience. In: Proceedings of the International Topical Meeting on LWR Fuel Performance, March 2–5, p. 356. Portland, Oregon, USA.
130. Delafoy, C., Dewes, P., Miles, T., 2007. AREVA NP Cr_2O_3 -doped fuel development for BWRs (Paper 1071). In: Proceedings of the International LWR Fuel Performance Meeting, September 30–October 3, 2007. San Francisco, California, USA: ANS.
131. Nonon, C., Menard, J., Lansiart, S., *et al.*, 2004. PCI behaviour of chromium oxide doped fuel. In: Proceedings of the International Seminar on Pellet-Clad Interaction in Water Reactor Fuels, March 9–11, 2004, p. 305. Aix-en Provence, France: OECD-NEA.
132. Marchal, N., Campos, C., Garnier, C., 2009. Finite element simulation of pellet-cladding interaction (PCI) in nuclear fuel rods. Comput. Mater. Sci. 45, 821.
133. Misfeldt, I., 1980. A stress corrosion failure model. In: Proceedings of the IAEA Specialists' Meeting on Fuel Element Performance Computer Modeling, SRE-14-77, March 17–21, 1980. Blackpool, UK, March.
134. Zhou, G., Lindbäck, J.E., Schutte, H.C., Jernkvist, L.O., Massih, A.R., 2004. Modeling pellet-clad interaction during power ramps. In: Proceedings of the Pellet-clad Interactions in Water Reactor Fuels, March 9–11, 2004. Aix-en Provence, France.
135. Miller, A.K., Ocken, H., Tasooji, A., 1981. Iodine stress corrosion cracking of zircaloy: Laboratory data, a phenomenological mode, and predictions of in-reactor behavior. J. Nucl. Mater. 99, 254.
136. Park, S.Y., Kim, J.H., Lee, M.H., Jeon, Y.H., 2008. Stress-corrosion crack initiation and propagation behavior of Zircaloy-4 cladding under iodine environment. J. Nucl. Mater. 372, 293.
137. Kreyns, P.H., Spahr, G.L., McCauley, J.E., 1976. An analysis of iodine stress corrosion cracking of zircaloy-4 tubing. J. Nucl. Mater. 61, 203.
138. Wood, J.C., 1972. Factors affecting stress corrosion cracking of zircaloy in iodine vapour. J. Nucl. Mater. 45, 105.
139. Anderson, T.L., 1995. Fracture Mechanics – Fundamentals and Applications.
140. Michel, B., Sercombe, J., Thouvenin, G., 2008. A new phenomenological criterion for pellet-cladding interaction rupture. Nucl. Eng. Des. 238, 1612.
141. Mattas, R.F., Yaggee, F.L., Neimark, L.A., 1979. Iodine stress-corrosion cracking in irradiated zircaloy cladding. In: Proceedings of the Topical Meeting on LWR Fuel, April 30–May 2, 1979. Portland, Oregon, USA.
142. Rousselier, G., Leclercq, S., Diard, O., 2003. Scenario for the damage of PWR fuel cladding in situations of pellet-cladding interaction. In: Proceedings of the 17th International Conference on Structural Mechanics in Reactor Technology (SMIRT17), August 17–22, 2003, Paper C03 Prague, Czech Republic.
143. Schuster, I., Lemaignan, C., 1992. Influence of texture on iodine-induced stress corrosion cracking of Zircaloy-4 cladding tubes. J. Nucl. Mater. 189, 157.
144. Xin, X.K., Lai, W.S., Liu, B.X., 2009. Point defect properties in hcp and bcc Zr with trace solute Nb revealed by ab initio calculations. J. Nucl. Mater. 393, 197.
145. Kaji, Y., Tsuru, T. Investigation of model for stress corrosion cracking of cladding materials. In: Proceedings of the 7th International Workshop Materials Modeling and Simulations of Nuclear Fuel (MMSNF), September 29–30. Karlsruhe, Germany.
146. Musienko, A., Cailletaud, G., 2009. Simulation of inter- and intragranular crack propagation in polycrystalline aggregates due to stress corrosion cracking. Acta Mater. 57, 3840.
147. Sercombe, J., Aubrun, I., Nonon, C., 2012. Power ramped cladding stresses and strains in 3D simulations with burnup-dependent pellet-clad friction. Nucl. Eng. Des. 242, 164.
148. Suzuki, M., Uetsuka, H., Saitou, H., 2004. Analysis of mechanical load on cladding induced by fuel swelling during power ramp in high burn-up rod by fuel performance code FEMAXI-6. Nucl. Eng. Des. 229, 1.
149. Shimada, S., Etoh, E., Hayashi, H., Tukuta, Y., 2004. A metallographic and fractographic study of outside-in cracking caused by power ramp tests. J. Nucl. Mater. 327, 97.
150. Van Uffelen, P., 2002. Contribution to the Modeling of Fission Gas Release in Light Water Reactor Fuel. Nuclear Engineering (PhD Thesis). University of Liege.
151. Tonks, M., Andersson, D., Devanathan, R., *et al.*, 2018. Unit mechanisms of fission gas release: Current understanding and future needs. J. Nucl. Mater. 504, 300.
152. Rest, J., Cooper, M.W.D., Spino, J., *et al.*, 2019. Fission gas release from UO_2 nuclear fuel: A review. J. Nucl. Mater. 513, 310.
153. Wise, C., 1985. Recoil release of fission products from nuclear fuel. J. Nucl. Mater. 136, 30.
154. Lewis, B.J., 1987. Fission product release from nuclear fuel by recoil and knock-out. J. Nucl. Med. 148, 28.
155. Grimes, R.W., 1991. Simulating the behaviour of inert gases in UO_2 . In: Fundamental Aspects of Inert Gases in Solids, 279. Plenum Press. p. 415.
156. Pastore, G., Swiler, L.P., Hales, J.D., *et al.*, 2015. Uncertainty and sensitivity analysis of fission gas behavior in engineering-scale fuel modeling. J. Nucl. Mater. 456, 398.
157. Andersson, D.A., García, P., Liu, X.-Y., *et al.*, 2014. Atomistic modeling of intrinsic and radiation-enhanced fission gas (Xe) diffusion in UO_{2+x} . Implications for nuclear fuel performance modeling. J. Nucl. Mater. 451, 225.

158. Vathonne, E., Andersson, D.A., Freyss, M., *et al.*, 2017. Determination of krypton diffusion coefficients in uranium dioxide using atomic scale calculations. *Inorg. Chem.* 56, 125.
159. Turnbull, J.A., Friskney, C.A., Findlay, J.R., Johnson, F.A., Walter, A.J., 1982. The diffusion coefficients of gaseous and volatile species during the irradiation of uranium oxide. *J. Nucl. Mater.* 107, 168.
160. Turnbull, J.A., White, R.J., Wise, C.A., 1988. The diffusion coefficient for fission gas atoms in uranium dioxide. In: *Proceedings of the Technical Committee Meeting on Water Reactor Fuel Element Computer Modeling in Steady State, Transient and Accidental Conditions*, T1-TC-659, September 18–22, 1988, Paper 3.5, p. 174. Preston, England: International Atomic Energy Agency.
161. Turnbull, J.A., 1971. The distribution of intragranular fission gas bubbles in UO_2 during irradiation. *J. Nucl. Mater.* 38, 203.
162. Cornell, R.M., 1971. An electron microscope examination of matrix fission-gas bubbles in irradiated uranium dioxide. *J. Nucl. Mater.* 38, 319.
163. Baker, C., 1977. The fission gas bubble distribution in uranium dioxide from high temperature irradiated SGHWR fuel pins. *J. Nucl. Mater.* 66, 283.
164. Kashibe, S., Une, K., Nogita, K., 1993. Formation and growth of intragranular fission gas bubbles in UO_2 fuels with burnup of 6–83 GWd/t. *J. Nucl. Mater.* 206, 22.
165. Olander, D.R., Wongsawaeng, D., 2006. Re-solution of fission gas – A review: Part I. Intragranular bubbles. *J. Nucl. Mater.* 354, 94.
166. Veshchunov, M.S., 2000. On the theory of fission gas bubble evolution in irradiated UO_2 . *J. Nucl. Mater.* 277, 67.
167. Rest, J., Zawadski, S.A., 1992. FASTGRASS: A Mechanistic Model for the Prediction of Xe, I, Cs, Te, Ba and Sr Release From Nuclear Fuel Under Normal and Sever-accident Conditions, NUREG/CR-5840, ANL-92/3.
168. Martin, G., Garcia, P., Sabathier, C., *et al.*, 2010. Irradiation-induced heterogeneous nucleation in uranium dioxide. *Phys. Lett. A* 374, 3038.
169. Govers, K., Bishop, C.L., Parfitt, D.C., *et al.*, 2012. Molecular dynamics study of Xe bubble re-solution in UO_2 . *J. Nucl. Mater.* 420, 282.
170. Setyawan, W., Cooper, M.W.D., Roche, K.J., *et al.*, 2018. Atomistic model of xenon gas bubble re-solution rate due to thermal spike in uranium oxide. *J. Appl. Phys.* 124, 075107.
171. White, R.J., Corcoran, R.C., Barnes, J.P., 2006. A Summary of Swelling Data Obtained from the AGR/Halden Ramp Test Programme, R&T/NG/EXT/REP/0206/02.
172. Turnbull, J.A., 1976. The mobility of intragranular bubbles in uranium dioxide during irradiation. *J. Nucl. Mater.* 62, 325.
173. Baker, C., 1977. The migration of intragranular fission gas bubbles in irradiated uranium dioxide. *J. Nucl. Mater.* 71, 117.
174. Matzke, H., 1980. Gas release mechanisms in UO_2 – A critical overview. *Radiat. Eff.* 53, 219.
175. Olander, D.R., Van Uffelen, P., 2001. On the role of grain boundary diffusion in fission gas release. *J. Nucl. Mater.* 288, 137.
176. White, R.J., 2004. The development of grain-face porosity in irradiated oxide fuel. *J. Nucl. Mater.* 325, 61.
177. Noirot, J., Gonnier, C., Desgranges, L., Pontillon, Y., Lamontagne, J., 2006. LWR fuel gas characterization at CEA Cadarache LECA-STAR hot laboratory. In: *Proceedings of the Technical Committee Meeting on Post-Irradiation Examination and In-Pile Measurement Techniques for Water Reactor Fuels*, TECDOC-1635, Part I, p. 129. Buenos Aires, Argentina: IAEA.
178. Turnbull, J.A., 1974. The effect of grain size on the swelling and gas release properties of UO_2 during irradiation. *J. Nucl. Mater.* 50, 62.
179. Clemm, P.J., Fisher, J.C., 1955. The influence of grain boundaries on the nucleation of secondary phases. *Acta Metall.* 3, 70.
180. Vitanza, C., Graziani, U., Fordestrommen, N.T., Vilpponen, K.O., 1978. Fission gas release from in-pile measurements. In: *Proceedings of the Enlarged Halden Programme Group Meeting*, HPR-221.10, November, 1978, Paper 38. Loen, Norway: OECD Halden Reactor Project.
181. Vitanza, C., Kolstad, E., Graziani, C. Fission gas release from UO_2 pellet at high burnup. In: *Proceedings of the Topical Meeting on Light Water Reactor Fuel Performance*, May. Portland, OR: American Nuclear Society.
182. Nakamura, T., Sasajima, H., Fuketa, T., Ishijima, K., 1996. Fission gas induced cladding deformation of LWR fuel rods under reactivity initiated accident conditions. *J. Sci. Technol.* 33, 924.
183. Lemoine, F., Cazalis, B., Rigat, H. The role of fission gases on the high burn-up fuel behaviour in reactivity initiated accident conditions. In: *Proceedings of the 10th International Symposium on Thermodynamics of Nuclear Materials*, vol. 248, August 6–11. Halifax, Canada.
184. Pastore, G., Pizzocri, D., Hales, J.D., *et al.*, 2014. Modeling of transient fission gas behaviour in oxide fuel and application to the BISON code. In: *Proceedings of the Enlarged Halden Programme Group Meeting*, September 7–12, 2014, Paper F7.4. Rorås, Norway: OECD Halden Reactor Project.
185. Barani, T., Bruschi, E., Pizzocri, D., *et al.*, 2017. Analysis of transient fission gas behaviour in oxide fuel using BISON and TRANSURANUS. *J. Nucl. Mater.* 486, 96.
186. Noirot, L. MARGARET: An advanced mechanistic model for fission gas behaviour in nuclear fuel. In: *Proceedings of the International Topical Meeting on Light Water Reactor Fuel Performance*, October 2–5. Kyoto, Japan: ANS.
187. Noirot, L., 2011. MARGARET: A comprehensive code for the description of fission gas behavior. *Nucl. Eng. Des.* 241, 2099.
188. Booth, A.H., 1957. A Method of Calculating Fission Gas Diffusion From UO_2 Fuel and its Application to the x-2-f Loop Test, CRDC-721. Chalk River, Ontario: AECL.
189. Booth, A.H., 1957. A Suggested Method for Calculating the Diffusion of Radioactive Rare Gas Fission Products From UO_2 Elements and a Discussion of Proposed In-Reactor Experiments That May be Used to Test its Validity, DCI-27. Chalk River, Ontario: AECL.
190. Lassmann, K., Benk, H., 2000. Numerical algorithms for intragranular fission gas release. *J. Nucl. Mater.* 280, 127.
191. Pizzocri, D., Rabiti, C., Luzzi, L., *et al.*, 2016. PolyPole-1: An accurate numerical algorithm for intra-granular fission gas release. *J. Nucl. Mater.* 478, 333.
192. Speight, M.V., 1969. A calculation on the migration of fission gas in material exhibiting precipitation and re-solution of gas atoms under irradiation. *Nucl. Sci. Eng.* 37, 180.
193. Pastore, G., Pizzocri, D., Rabiti, C., *et al.*, 2018. An effective numerical algorithm for intra-granular fission gas release during non-equilibrium trapping and resolution. *J. Nucl. Mater.* 509, 687.
194. Turnbull, J.A., 1980. A review of irradiation induced re-solution in oxide fuels. *Radiat. Eff.* 53, 243.
195. Löföten, P., 2000. On the behaviour of intragranular fission gas in UO_2 fuel. *J. Nucl. Mater.* 280, 56.
196. White, R.J., Tucker, M.O., 1983. A new fission gas release model. *J. Nucl. Mater.* 118, 1.
197. Wirth, B.D., Andersson, A.D., Blondel, S., *et al.*, 2018. Multiscale modeling of fission gas bubble evolution in UO_2 under nominal operating conditions. *Trans. Am. Nucl. Soc.* 118, 1325.
198. Pastore, G., Luzzi, L., Di Marcello, V., Van Uffelen, P., 2013. Physics-based modeling of fission gas swelling and release in UO_2 applied to integral fuel rod analysis. *Nucl. Eng. Des.* 256, 75.
199. Pizzocri, D., Pastore, G., Barani, T., *et al.*, 2018. A model describing intra-granular fission gas behaviour in oxide fuel for advanced engineering tools. *J. Nucl. Mater.* 502, 323.
200. Forsberg, K., Massih, A.R., 2001. Theory of fission gas release during grain growth. In: *Proceedings of the Structural Mechanics in Reactor Technology (SMIRT16)*, August 12–17, Paper 1931. Washington DC.
201. Ainscough, J.B., Oldfield, B.W., Ware, J.O., 1973. Isothermal grain growth kinetics in sintered UO_2 pellets. *J. Nucl. Mater.* 49, 117.
202. Forsberg, K., Massih, A.R., 1985. Diffusion theory of fission gas migration in irradiated nuclear fuel. *J. Nucl. Mater.* 135, 140.
203. Une, K., Kashibe, S., 1990. Fission gas release during post irradiation annealing of BWR fuels. *J. Nucl. Sci. Technol.* 27, 1002.
204. Ronchi, C., 1981. Extrapolated equation of state for rare gases at high temperatures and densities. *J. Nucl. Mater.* 96, 314.
205. MATPRO, 2003. MATPRO a Library of Materials Properties for Light-Water-Reactor Accident Analysis, SCDAP/RELAP5-3D Code Manual. Idaho National Engineering and Environmental Laboratory.
206. Billiaux, M.R., 2005. Fuels performance, limits, operational and safety issues. In: *Proceedings of the Lecture Notes at Frederic Joliot-Otto Hahn Summer School*, August 24–September 2. Karlsruhe, Germany.
207. Koo, Y.H., Sohn, D.S., Yoon, Y.K., 1994. An analysis method for the fuel rod gap inventory of unstable fission products during steady-state operation. *J. Nucl. Mater.* 209, 62.

208. Kogai, T., 1997. Modeling of fission gas release and gaseous swelling of light water reactor fuels. *J. Nucl. Mater.* 244, 131.
209. Pastore, G., 2012. Modeling of Fission Gas Swelling and Release in Oxide Nuclear Fuel and Application to the TRANSURANUS Code, Department of Energy. Politecnico di Milano.
210. Speight, M.V., Beere, W., 1975. Vacancy potential and void growth on grain boundaries. *Met. Sci.* 9, 190.
211. White, R.J., Tucker, M.O., 1983. A new fission-gas release model. *J. Nucl. Mater.* 118, 1.
212. Koo, Y.H., Lee, B.H., Sohn, D.S., 2000. Analysis of fission gas release and gaseous swelling in UO_2 fuel under the effect of external restraint. *J. Nucl. Mater.* 280, 86.
213. Olander, D.R., Mubayi, V., 1999. Review of the materials-chemistry models in the VICTORIA code. *J. Nucl. Mater.* 270, 1.
214. Khvostov, G., Mikityuk, K., Zimmermann, M.A., 2011. A model for fission gas release and gaseous swelling of the uranium dioxide fuel coupled with the FALCON code. *Nucl. Eng. Des.* 241, 2983.
215. Van Uffelen, P., Györi, C.S., Schubert, A., *et al.*, 2008. Extending the application range of a fuel performance code from normal operating to design basis accident conditions. *J. Nucl. Mater.* 383, 137.
216. Meyer, R.O., 2006. The U.S. Nuclear Regulatory Commission's research on fuel behaviour under accident conditions. In: *Proceedings of the International Meetings on LWR Fuel Performance, Top Fuel 2006*, October 22–27, p. 284. Salamanca, Spain.
217. Geelhood, K.J., Luscher, W.G., Beyer, C.E., *et al.*, 2009. Predictive Bias and Sensitivity in NRC Fuel Performance Codes. NRC, U. (Ed.), Richland, WA: PNNL.
218. Van Uffelen, P., van de Laar, J., Schubert, A., *et al.*, 2013. Modeling of nuclear fuel under accident conditions by means of TRANSURANUS. In: *Proceedings of the IAEA Technical Meeting on Modeling of Water-Cooled Fuel Including Design-Basis and Severe Accidents*, October 28–November 4, 2013, Chengdu, P.R. China.
219. Geelhood, K.J., Beyer, C.E., Cunningham, M.E., 2004. Modifications to FRAPTRAN to predict fuel rod failures due to PCMI during RIA-type accidents. In: *Proceedings of the International Meeting on LWR Fuel Performance*, September, p. 585. Orlando, Florida, USA.
220. Sonnenburg, H.G. Study of fuel rod criteria for LOCA condition in the light of recent experimental data. In: *Proceedings of the International Meeting on LWR Fuel Performance, Nuclear fuel: Addressing the future*, Top Fuel, October 22–27, p. 467. Salamanca, Spain.
221. Veshchunov, M.S., Ozrin, V.D., Shestak, V.E., *et al.*, 2006. Development of the mechanistic code MFPR for modeling fission-product release from irradiated UO_2 fuel. *N. Eng. Des.* 236, 179.
222. Berna, G.A., Scott, H., 2001. FRAPTRAN: A Computer Code for the Transient Analysis of Oxide Fuel Rods, NUREG/CR-6739. U.S. Nuclear Regulatory Commission.
223. Federici, E., Lamare, F., Besson, V., Papin, J., 2001. The SCANAIR code version 3.2: Main features and status of qualification. In: *Proceedings of the IAEA Technical Committee Meeting on Fuel Behaviour Under Transient and LOCA Conditions*, p. 88. Halden, Norway: IAEA.
224. Pettersson, K., Chung, H., Billone, M., *et al.*, 2009. Nuclear Fuel Behaviour in Loss-of-Coolant Accident (LOCA) Conditions. State-of-the-Art-Report. Paris: OECD-NEA, p. 369.
225. Massih, A.R., 2009. Transformation kinetics of zirconium alloys under non-isothermal conditions. *J. Nucl. Mater.* 384, 330.
226. Györi, C., Van Uffelen, P., Schubert, A., van de Laar, J., Hózer, Z. Implementing experimental data on the accidental behaviour of the WWER cladding obtained at the AEKI in the TRANSURANUS fuel performance code. In: *Proceedings of the 6th International Conference on WWER Fuel Performance, Modeling and Experimental Support*, September 19–23. Albena, Bulgaria.
227. Forgeron, T., Brachet, J.C., Barcelo, F., *et al.* Experiment and modeling of advanced fuel rod cladding behaviour under LOCA conditions: Alpha-Beta phase transformation kinetics and EDGAR methodology. In: *Proceedings of the 12th International Symposium: Zirconium in the Nuclear Industry*, ASTM STP 1354, West Conshohocken.
228. Baker, L., Just, L.C., 1962. Studies of Metal Water Reactions at High Temperature: III. Experimental and Theoretical Studies of Zirconium-Water Reaction, ANL-6548. Chicago: Argonne National Laboratory.
229. Cathcart, J.V., Pawel, R.E., McKee, R.E., *et al.*, 1977. Zirconium Metal-Water Oxidation Kinetics, IV. Reaction Rate Studies, ORNL/NUREG-17. ORNL.
230. Solyan, V.I., Bibilashvili, Y.K., Tonkov, V.Y., 1983. High temperature oxidation and deformation of Zr1\%Nb alloy of WWER fuels. In: *Proceedings of the OECD-NEA-CSNI/IAEA Specialists Meeting on Water Reactor Fuel Safety and Fission Product Release in Off-Normal and Accident Conditions*, May 16–20, 1983, p. 163. Risø, Denmark.
231. Györi, C.S., Hózer, Z., Lassmann, K., *et al.* Extension of TRANSURANUS code applicability with niobium containing cladding models (EXTRA). In: *Proceedings of the EU Research in Reactor Safety, Conclusion Symposium on Shared-Cost and Concerted Actions (FISA-2003)*, Proceedings – EUR 21026, November 10–13, p. 584. Luxembourg.
232. Urbanic, V.F., Heidrick, T.R., 1978. High-temperature oxidation of zircaloy-2 and zircaloy-4 in steam. *J. Nucl. Mater.* 75, 251.
233. Pawel, R., Cathcart, J., McKee, R., 1979. The Kinetics of Oxidation of Zircaloy-4 in Steam at High Temperatures. *J. Electrochem. Soc.* 126, 1105.
234. Uchida, M., Otsubo, N., 1984. Models of Multi-Rod Code FRETA-B for Transient Fuel Behavior Analysis (Final Version), JAERI-1293. JAERI.
235. Erbacher, F.J., Neitzel, H.J., Rosinger, H., Schmidt, H., Wiehr, K. Burst criterion of zircaloy fuel claddings in a loss-of-coolant accident. In: *Proceedings of the Zirconium in the Nuclear Industry, Fifth Conference*, ASTM STP 754, p. 271.
236. OECD-NEA, 2016. CSNI Report on Fuel Fragmentation, Relocation, Dispersal. Paris: OECD-NEA, p. 219.
237. Raynaud, P., 2012. Fuel Fragmentation, Relocation, and Dispersal During the Loss-of-Coolant Accident, NUREG-2121. USNRC.
238. Jernkvist, L.O., Massih, A., 2015. Models for Axial Relocation of Fragmented and Pulverized Fuel Pellets in Distending Fuel Rods and its Effects on Fuel Rod Heat Load. Stockholm: Swedish Radiation Safety Authority, p. 94. (2015:37, ISSN: 2000-0456).
239. Govers, K., Verwerf, M., 2015. An insight on fuel fragmentation, relocation and dispersal during loss-of-coolant accidents from computer simulations. In: *Proceedings of the Top Fuel*, September. Zurich, Switzerland.
240. IAEA, 2018. Fuel Modeling in Accident Conditions (FUMAC), Report of a Coordinated Research Project, IAEA CRP T12028 (2014-2018). Vienna: IAEA, (TECDOC in preparation).
241. Veshchunov, M., Stuckert, J., Van Uffelen, P., Wiesenack, W., Zhang, J., 2018. FUMAC. IAEA's coordinated research project on fuel modeling in accident conditions. In: *Proceedings of the Top Fuel 2018*, September 28–October 4, 2018. Prague, Czech Republic.
242. Uchida, M., Nakamura, J., Otsubo, N., 1983. Application of transient fuel bundle analysis code FRETA-B to LOCA simulation experiments. In: Gittus, J. (Ed.), *Water Reactor Fuel Element Performance Computer Modeling*. Applied Science Publishers Ltd., p. 631.
243. Uchida, M., Nakamura, J., 1981. Matrix calculation of radiant heat transfer in LWR fuel bundles under accident conditions. *Nucl. Eng. Des.* 65, 63.
244. Uchida, M., 1984. Application of a two-dimensional ballooning model to out-pile and in-pile simulation experiments. *Nucl. Eng. Des.* 77, 37.
245. Georges, R., François, J., François, B., François, L., Jean-Marc, R., 2009. DRACCAR, a new 3D-thermal mechanical computer code to simulate LOCA transient on Nuclear Power Plants – Status of the development and the validation. In: *Proceedings of the ICAPP '09*, May 10–14, 2009. Tokyo, Japan.
246. Pastore, G., Novascone, S.R., Williamson, R.L., *et al.*, 2015. Modeling of fuel behaviour during loss-of-coolant accidents using the BISON code. In: *Proceedings of the Top Fuel 2015*, September 13–17, 2015, p. 552. Zurich, Switzerland: ENS/ANS.
247. Udagawa, Y., Fuketa, T., 2019. Transient response of LWR fuels (RIA). In: Konings, R.J.M. (Ed.), *Comprehensive Nuclear Materials*, vol. 2. Elsevier Ltd, pp. 322–338.
248. Meyer, R., McCardell, R., Chung, H., Diamond, H., Scott, H., 1996. A regulatory assessment of test data for reactivity initiated accidents. *Nucl. Saf.* 37, 271.
249. Fuketa, T., Sasajima, H., Mori, Y., Ishijima, K., 1997. Fuel failure and fission gas release in high burnup PWR fuels under RIA conditions. *J. Nucl. Mater.* 248, 249.
250. Fuketa, T., Sasajima, H., Sugiyama, T., 2001. Behavior of high-burnup PWR fuels with low-tin zircaloy-4 cladding under reactivity-initiated-accident conditions. *Nucl. Technol.* 133, 50.
251. Nakamura, T., Kusagaya, K., Fuketa, T., Uetsuka, H., 2002. High-burnup BWR fuel behavior under simulated reactivity-initiated accident conditions. *Nucl. Technol.* 138, 246.
252. Papin, J., Balourd, M., Lemoine, F., *et al.*, 1996. French studies on high-burnup fuel transient behavior under RIA conditions. *Nucl. Saf.* 37, 289.

253. Suzuki, M., Sugiyama, T., Fuketa, T., 2008. Thermal stress analysis of high burnup LWR fuel pellet pulse-irradiated in reactivity-initiated accident conditions. *J. Nucl. Sci. Technol.* 45, 1155.
254. Suzuki, M., Fuketa, T., 2006. Analysis of pellet-clad mechanical interaction process of high-burnup PWR fuel rods by RANNS code in reactivity-initiated accident conditions. *Nucl. Technol.* 155, 282.
255. Bessiron, V., Sugiyama, T., Fuketa, T., 2007. Clad-to-coolant heat transfer in NSRR experiments. *J. Nucl. Sci. Technol.* 44, 723.
256. Lemoine, F., 1997. High burnup fuel behaviour related to fission gas effects under reactivity initiated accidents (RIA) conditions. *J. Nucl. Mater.* 248, 238.
257. Jernkvist, L.O., Massih, A.R., Fuketa, T., *et al.*, 2010. Nuclear Fuel Behaviour Under Reactivity-Initiated Accident (RIA) Conditions, State-of-the-Art Report, NEA/CSNI/R (2010)1. OECD-NEA.
258. Sasajima, H., Sugiyama, T., Chuto, T., *et al.*, 2010. Identification of radial position of fission gas release in high-burnup fuel pellets under RIA conditions. *J. Nucl. Sci. Technol.* 47, 202.
259. Khvostov, G., Zimmermann, M.A., Ledergerber, G., 2009. Parametric study of fuel rod behaviour during the RIA using the modified FALCON code. In: *Proceedings of the Workshop on Nuclear Fuel Behaviour During Reactivity Initiated Accidents*, September 9–11, 2009, p. 247. Paris, France: OECD-NEA.
260. Clifford, P.M., 2015. Technical and Regulatory Basis for the Reactivity-initiated Accident Acceptance Criteria and Guidance, Revision 1. Personal Communication.
261. OECD-NEA, 2012. Nuclear fuel safety criteria technical review, second ed. OECD-NEA. (ISBN 978-92-64-99178-1).
262. Jernkvist, L.O., 2006. Computational Assessment of Burnup-Dependent Fuel Failure Thresholds for Reactivity Initiated Accidents. *J. Nucl. Sci. Technol.* 43, 546.
263. Desquines, J., Cazalis, B., Bernaudat, C., Poussard, C., Averty, X., Yvon, P. Mechanical properties of Zircaloy-4 PWR fuel cladding with burnup 54-64 MWd/kgU and implications for RIA behavior, In: *Proceedings of the 14th International symposium on zirconium in the nuclear industry*, vol. 2, Stockholm, Sweden: ASTM, June 13–17, p. 851.
264. Kuroda, M., Yamanaka, S., Nagase, F., Uetsuka, H., 2001. Analysis of the fracture behavior of hydrided fuel cladding by fracture mechanics. *Nucl. Eng. Des.* 203, 185.
265. Le Saux, M., 2008. Comportement et rupture de gaines en Zircaloy-4 détendu vierges, hydrurées ou irradiées en situation accidentelle de type RIA Ecole Nationale Supérieure des Mines (MINES ParisTech).
266. Rashid, J.Y.R., Montgomery, R.O., Lyon, W.F., Yang, R., 2000. A cladding failure model for fuel rods subjected to operational transients and accident transients. In: *Proceedings of the Technical Committee Meeting on Nuclear Fuel Behaviour Modeling at High Burnup and its Experimental Support*, June 19–23, 2000, p. 187. Windermere, UK: IAEA.
267. Bernaudat, C., Pupier, P. A new analytical approach to study the rod ejection accident in PWRs. In: *Proceedings of the International Topical Meeting on Light Water Reactor Fuel Performance*, p. 602. Kyoto, Japan.
268. Leclercq, S., Parrot, A., Leroy, M., 2008. Failure characteristics of cladding tubes under RIA conditions. *Nucl. Eng. Des.* 238, 2206.
269. Tomiyasu, K., Sugiyama, T., Fuketa, T., 2007. Influence of cladding-peripheral hydride on mechanical fuel failure under reactivity-initiated accident conditions. *J. Nucl. Sci. Technol.* 43, 733.
270. Suzuki, M., Sugiyama, T., Udagawa, Y., Nagase, F., Fuketa, T., 2009. Comparative analysis on behavior of high burnup PWR fuels pulse-irradiated in reactivity-initiated accident conditions. In: *Proceedings of the Water Reactor Fuel Performance Meeting*, September 6–10, 2009. Paris, France.
271. Sartoris, C., Taisne, A., Petit, M., Barré, F., Marchand, O., 2009. Example of application of the IRSN approach to assess safety criteria for reactivity initiated accidents. In: *Proceedings of the Workshop on Nuclear Fuel Behaviour during Reactivity Initiated Accidents*, September 9–11, 2009. Paris, France: OECD-NEA.
272. Arifman, A., Cherubini, M., Dostál, M., *et al.*, 2013. RIA Fuel Codes Benchmark. Volume 1. OECD-NEA-CSNI.
273. OECD-NEA, 2016. Reactivity Initiated Accident (RIA) Fuel Codes Benchmark Phase-II, NEA/CSNI/R(2016)6. Paris: OECD-NEA.
274. Lassmann, K., 1983. Numerical noise analysis: A new probabilistic technique. *Comput. Methods Applied Mech. Eng.* 40, 111.
275. Peck, S.O., 1980. Automated uncertainty analysis methods in the FRAP computer codes. In: *Proceedings of the Specialists Meeting on Fuel Element Performance Computer Modeling*, IWGFPT/7, March 17–21, 1980, p. 260. Blackpool, U.K.: IAEA.
276. Forsberg, K., Ning, H., Massih, A.R., 1996. Probabilistic analysis of nuclear fuel rod behaviour using quasi monte carlo method. *Nucl. Sci. Eng.* 122, 142.
277. Heins, L., Groß, H., Nissen, K., Wunderlich, F., 1991. Statistical analysis of QC data and estimation of fuel rod behaviour. *J. Nucl. Mater.* 178, 287.
278. Sauer, G., 2005. Semi-statistical mechanical fuel rod design. *Kerntechnik* 70, 153.
279. Sauer, G., Besenböck, W., 2008. Reliable statistical fuel rod analysis (Paper 8031). In: *Proceedings of the Water Reactor Fuel Performance Meeting*, October 19–23, 2008. Seoul, Korea: KNS.
280. Arimescu, V.I., 2008. Best-estimate BWR fuel thermal-mechanical analysis based on non-parametric order statistics (Paper 8094). In: *Proceedings of the Water Reactor Fuel Performance Meeting*, October 19–23, 2008. Seoul, Korea: KNS.
281. Arkoma, A., Hänninen, M., Rantamäki, K., Kurki, J., Hämäläinen, A., 2015. Statistical analysis of fuel failures in large break loss-of-coolant accident (LBLOCA) in EPR type nuclear power plant. *Nucl. Eng. Des.* 285, 1.
282. Ikonen, T., Tulkki, V., 2014. The importance of input interactions in the uncertainty and sensitivity analysis of nuclear fuel behavior. *Nucl. Eng. Des.* 275, 229.
283. Hedayat, A.S., Sloane, N.J.A., Stufken, J., 1999. *Orthogonal Arrays: Theory and Applications*. New York, NY: Springer-Verlag, p. 417.
284. Montgomery, D.C., Runger, G.C., 2011. *Applied Statistics and Probability for Engineers*. John Wiley & Sons Inc.
285. Adams, B.M., Dalbey, K.R., Eldred, M.S., *et al.*, 2011. DAKOTA: A Multilevel Parallel Object-oriented Framework for Design Optimization, Parameter Estimation, Uncertainty Quantification, and Sensitivity Analysis. Version 5.2 User's Manual. Sandia National Laboratories.
286. Wu, X., Kozłowski, T., Meidani, H., 2018. Kriging-based inverse uncertainty quantification of nuclear fuel performance code BISON fission gas release model using time series measurement data. *Reliab. Eng. Syst. Saf.* 169, 422.
287. Kleijnen, J.P.C., 2009. Kriging metamodeling in simulation: A review. *Eur. J. Oper. Res.* 192, 707.
288. Shih, C., Yang, J.-H., Wang, J.-R., *et al.*, 2016. Fuel rod behavior and uncertainty analysis by FRAPTRAN/TRACE/DAKOTA code in Maanshan LBLOCA. In: Tien, K. (Ed.), *International Agreement Report. Institute of Nuclear Engineering and Science, National Tsing Hua University*.
289. Bouloré, A., Struzik, C., Gaudier, F., 2012. Uncertainty and sensitivity analysis of the nuclear fuel thermal behavior. *Nucl. Eng. Des.* 253, 200.
290. Struzik, C., Bouloré, A., Arnaud, G., 2017. Determination of the fuel melting probability in MTR using reliability methods. In: *Water Reactor Fuel Performance Meeting*, Jeju Island, Korea.
291. Cherubini, M., Lampunio, L., 2018. TRANSURANUS analysis on the effect of the isotopic composition on fuel response to ramp test. In: *Proceedings of the Best Estimate Plus Uncertainty International Conference. Multi-Physics Multi-Scale Simulations With Uncertainty (BEPU)*, May 13–19, Lucca, Italy.
292. Syrjälähti, E., 2011. Characterization of a representative VVER-440 fuel rod with the statistical ENIGMA, VTT-R-08464-11. Espoo: VTT, p. 18.
293. Lassmann, K., 1980. The statistical version of the URANUS-programme. *Nucl. Eng. Des.* 56, 35.
294. Marchand, O., Zhang, J., Cherubini, M., 2018. Uncertainty and sensitivity analysis in reactivity-initiated accident fuel modeling: Synthesis of organisation for economic co-operation and development (OECD)/nuclear energy agency (NEA) benchmark on reactivity-initiated accident codes phase-II. *Nucl. Eng. Technol.* 50, 280.
295. Lassmann, K., Walker, C.T., van de Laar, J., Lindström, F., 1995. Modeling the high burnup UO_2 structure in LWR fuel fuels. *J. Nucl. Mater.* 226, 1.
296. Noirot, J., Pontillon, Y., Yagnik, S., Turnbull, J.A., Tverberg, T., 2014. Fission gas release behaviour of a 103 GWd/tHM fuel disc during a 1200°C annealing test. *J. Nucl. Mater.* 446, 163.
297. Manzel, R., Walker, C.T., 2002. EPMA and SEM of fuel samples from PWR rods with an average burn-up of around 100 MWd/kgHM. *J. Nucl. Mater.* 301, 170.
298. Sonoda, T., Matzke, H., Kinoshita, M. High burnup rim project (IV) threshold burnup of rim structure formation. In: *Proceedings of the EHPG*, Leon, Norway.
299. Sonoda, T., Kinoshita, M., Ray, I.L.F., *et al.*, 2002. Transmission electron microscopy observation on irradiation-induced microstructural evolution in high burn-up UO_2 disk fuel. *Nucl. Instrum. Methods Phys. Res. B* 191, 622.

300. Walker, C.T., Coquerelle, M., 1991. Correlation between microstructure and fission gas release in high burn-up UO_2 and MOX fuel. In: Proceedings of the International Topical Meeting in LWR Fuel Performance, vol. II, April 21–24, 1991, p. 506. Avignon, France: ANS/ENS, p. 506.
301. Walker, C.T., Goll, W., Matsumura, T., 1997. Further observations on OCOM MOX fuel: Microstructure in the vicinity of the pellet rim and fuel-cladding interaction. *J. Nucl. Mater.* 245, 169.
302. Bouloré, A., Auforea, L., Federici, E., Blanpain, P., Blachier, R., 2015. Advanced characterization of MIMAS MOX fuel microstructure to quantify the HBS formation. *Nucl. Eng. Des.* 281, 79.
303. Gerczak, T.J., Parish, C.M., Edmondson, P.D., Baldwin, C.A., Terrani, K.A., 2018. Restructuring in high burnup UO_2 studied using modern electron microscopy. *J. Nucl. Mater.* 509, 245.
304. Noirot, J., Zacharie-Aubrun, I., Blay, T., 2018. Focused ion beam-scanning electron microscope examination of high burn-up UO_2 in the center of a pellet. *Nucl. Eng. Technol.* 50, 259.
305. Sontheimer, F., Landskron, H., Billaux, M.R., 1998. A fuel thermal conductivity correlation based on the latest experimental results. In: Proceedings of the Seminar on Thermal Performance of High Burn-Up LWR Fuel, March 3–6, 1998, p. 119. Cadarache, France: OECD-NEA.
306. Baron, D., 1998. About the Modeling of fuel thermal conductivity degradation at high-burnup accounting for recovering process with temperature. In: Proceedings of the Seminar on Thermal Performance of High Burn-Up LWR fuel, March 3–6, 1998, p. 129. Cadarache, France: OECD-NEA.
307. Walker, C.T., Staicu, D., Sheindlin, M., *et al.*, 2006. On the thermal conductivity of UO_2 nuclear fuel at a high burn-up of around 100 MWd/kgHM. *J. Nucl. Mater.* 350, 19.
308. Györi, C., Jonson, M., Robertson, G., *et al.*, 2017. Extension and validation of the TRANSURANUS code in the course of the ESSANUF project (Paper 3.10). In: Proceedings of the 12th International Conference on WWER Fuel Performance, Modeling and Experimental Support, September 16–23, 2017. Nessebar, Bulgaria: INRNE.
309. Limbäck, M., Krammen, M.A., Rudling, P., Pati, S.R., Garde, A.M., 1994. Corrosion and Hydriding performance of Zircalloy-2 and Zircalloy-4 cladding materials in PWR's. In: Proceedings of the Topical Meeting on LWR fuel performance, April 17–21, 1994, p. 286. West Palm Beach, Florida, USA: ANS.
310. Spino, J., Stalios, A.D., Santa Cruz, H., Baron, D., 2006. Stereological evolution of the rim structure in PWR-fuels at prolonged irradiation: Dependencies with burn-up and temperature. *J. Nucl. Mater.* 354, 66.
311. Baron, D., Masson, R., Gatt, J., Spino, J., Laux, D., 2005. Evolution of the nuclear fuel mechanical properties with burn-up. An extensive european experimental program. In: Proceedings of the International Topical Meeting on Light Water Reactor Fuel Performance, October 2–6, 2005, p. 957. Kyoto, Japan: American Nuclear Society.
312. Cappia, F., Pizzocri, D., Marchetti, M., *et al.*, 2016. Microhardness and Young's modulus of high burn-up UO_2 fuel. *J. Nucl. Mater.* 479, 447.
313. Marchetti, M., Laux, D., Cappia, F., *et al.*, 2016. High frequency acoustic microscopy for the determination of porosity and Young's modulus in high burnup uranium dioxide nuclear fuel. *IEEE Trans. Nucl. Sci.* 63, 1520.
314. Lee, C.-B., Kim, D.-H., Song, J.-S., Bang, J.-G., Jung, Y.-H., 2000. RAPID model to predict radial burnup distribution in LWR UO_2 fuel. *J. Nucl. Mater.* 282, 196.
315. O'Carroll, C., Walker, C.T., van de Laar, J., 1994. Validation of the TUBRNP model with the radial distribution of Plutonium in MOX fuel evaluated by SIMS and EMPA. In: Proceedings of the Technical Committee Meeting on Water Reactor Fuel Element Modeling at High Burnup and Experimental Support, September 30–October 3, 2007, p. 261. Windermere, UK: IAEA.
316. Bibilashvili, Y.K., Medvedev, A.V., Khostov, G.A., Bogatyr, S.M., Korystine, L.V., 2000. Development of the fission gas behaviour model in the START-3 code and its experimental support. In: Proceedings of the International Seminar on Fission Gas Behaviour on Fission Gas Behaviour in Water Reactor Fuels, September. Cadarache, France.
317. Killeen, J., Turnbull, J.A., Sartori, E., 2007. Fuel modeling at extended burnup: IAEA coordinated research project FUMEX-II. In: Proceedings of the International LWR Fuel Performance Meeting, September 30–October 3, 2007, p. 261. San Francisco, California, USA: ANS.
318. IAEA, 2013. Improvement of computer codes used for fuel behaviour simulation (FUMEX-III). Report of a Coordinated Research Project, IAEA-TECDOC-1697. Vienna.
319. Esnoul, C., Largenton, R., Petry, C., *et al.*, 2015. Use of micromechanical approach to investigate transient fuel fragmentation mechanisms. In: Proceedings of the TOP Fuel, vol. II, September 13–17, 2015, p. 476. Zürich, Switzerland.
320. Kulacsy, K., 2015. Mechanistic model for the fragmentation of the high-burnup structure during LOCA. *J. Nucl. Mater.* 466, 409.
321. Beauvy, M., 2006. Uranium and plutonium oxides. In: Proceedings of the Frederic Joliot – Otto Hahn Summer School on Nuclear Reactors Physics, Fuels and Systems, August 23–September 1, 2006. France: Cadarache.
322. Carbajo, J.J., Yoder, G.L., Popov, S.G., Ivanov, V.K., 2001. A review of the thermophysical properties of MOX and UO_2 Fuels. *J. Nucl. Mater.* 299, 181.
323. Massih, A.R., 2006. Models for MOX fuel behaviour – A selective review, SKI Report 2006:10.
324. Schubert, A., Van Uffelen, P., van de Laar, J., Sheindlin, M., Ott, L., 2004. Present status of the MOX version of the TRANSURANUS code (Paper F2.5). In: Proceedings of the Enlarged Halden Programme Group Meeting on High Burn-up Fuel Performance, Safety and Reliability, May 9–14, 2004. Sandefjord, Norway: OECD Halden Reactor Project.
325. Lippens, M., Van Loon, C., Ketels, J., 1986. Ceramographic techniques and electron probe micro-analysis applied to uranium-plutonium oxides. In: Proceedings of the Technical Committee Meeting on Properties of Materials for Water Reactor Fuel Elements and Methods of Measurement, IWGP7/26, October 13–16, 1986, p. 69. Vienna, Austria: IAEA.
326. Marin, J.M., 1988. Phenomenology of Uranium-Plutonium Homogenization in Nuclear fuels. Université de Provence. Aix-Marseille I.
327. Van Uffelen, P., 1994. Modèle d'évolution de l'homogénéité du plutonium dans le combustible MOX. Université Libre de Bruxelles.
328. IAEA, 2003. Status and advances in MOX fuel technology, Technical report series no. 415, IAEA STI/DOC/010/415.
329. Billaux, M., van Vliet, J., 1986. Impact of fuel heterogeneities on fission gas release for LWR U-Pu mixed oxide fuels. *Res. Mech.* 17, 41.
330. Ishida, M., Korei, Y., 1994. Modeling and parametric studies of the effect of Pu-mixing heterogeneity on fission gas release from mixed oxide fuels of LWRs and FBRs. *J. Nucl. Mater.* 210, 203.
331. Koo, Y.H., Lee, B.H., Cheon, J.S., Sohn, D.S., 2002. Modeling and parametric studies of the effect of inhomogeneity on fission gas release in LWR MOX fuel. *Ann. Nucl. Energy* 29, 271.
332. Koo, Y.H., Lee, B.H., Sohn, D.S., 1999. COSMOS: A computer code to analyze LWR UO_2 and MOX fuel to high burnup. *Ann. Nucl. Energy* 26, 47.
333. Bouloré, A., Struzik, C., Masson, R., Mailhé, P., Largenton, R., 2017. Approach to better assess fission gas behaviors, applicable to fuels with complex microstructures. In: Proceedings of the Water Reactor Fuel Performance Meeting. Jeju Island, Korea.
334. Luzzi, L., Cognini, L., Pizzocri, D., *et al.*, 2018. Helium diffusivity in oxide nuclear fuel: Critical data analysis and new correlations. *Nucl. Eng. Des.* 330, 265.
335. Blanpain, P., Lippens, M., Schut, H., Federov, A.V., Bakker, K. Helium solubility in UO_2 : The HARLEM project. In: Proceedings of the Workshop Materials Models and Simulations for Nuclear Fuels, June 1–2. Nice, France.
336. Cognini, L., Pizzocri, D., Barani, T., *et al.*, 2018. Helium solubility in oxide nuclear fuel: Derivation of new correlations for Henry's constant. *Nucl. Eng. Des.* 340, 240.
337. Valot, C., Bertolus, M., Malerba, L., *et al.*, 2015. Integrated multi-scale modeling and simulation of nuclear fuels. In: Bessmann, T.M. (Ed.), State-of-the-Art Report on Multi-Scale Modeling of Nuclear Fuels, p. 282. Paris, France: OECD-NEA.
338. Samaras, M., Victoria, M., Hoffelner, W., 2009. Nuclear energy materials prediction: Application of the multi-scale modeling paradigm. *Nucl. Eng. Technol.* 41, 1.
339. Stan, M., 2009. Multi-scale models and simulations of nuclear fuels. *Nucl. Eng. Technol.* 41, 39.
340. Crocombette, J., 2002. Ab initio energetics of some fission products (Kr, I, Cs, Sr, He) in uranium dioxide. *J. Nucl. Mater.* 305, 29.
341. Crocombette, J., Jollet, F., Nga, L., Petit, T., 2001. Plane-wave pseudopotential study of point defects in uranium dioxide. *Phys. Rev. B* 64, 104.
342. Wirth, B.D., Odette, G.R., Marian, J., *et al.*, 2004. Multiscale modeling of radiation damage in Fe-based alloys in the fusion environment. *J. Nucl. Mater.* 329–333, 103.
343. Malerba, L., 2006. Molecular dynamics study of displacement cascades in alpha-Fe: A critical review. *J. Nucl. Mater.* 351, 28.

- 344. Domain, C., Becquart, C., Malerba, L., 2004. Simulation of radiation damage in Fe alloys: An object kinetic Monte Carlo approach. *J. Nucl. Mater.* 335, 121.
- 345. Tonks, M.R., Liu, X.Y., Andersson, D.A., *et al.*, 2016. Development of a multiscale thermal conductivity model for fission gas in UO_2 . *J. Nucl. Mater.* 469, 89.
- 346. Verma, L., Noirot, L., Maugis, P., 2018. A new spatially resolved model for defects and fission gas bubbles interaction at the mesoscale. *Nucl. Instrum. Methods B.*
- 347. Michel, B., Helfer, T., Ramière, I., Esnoul, C., 2016. 3D continuum damage approach for simulation of crack initiation and growth in ceramic materials. *Key Eng. Mater.* 713, 155.
- 348. Portelette, L., 2018. Crystal viscoplastic modeling of UO_2 single crystal. *J. Nucl. Mater.* 510, 635.
- 349. Tonks, M.R., Gaston, D., Millett, P.C., Andrs, D., Talbot, P., 2012. An object-oriented finite element framework for multiphysics phase field simulations. *Comput. Mater. Sci.* 51, 20.
- 350. Tonks, M.R., Andersson, D.A., Phillpot, S.R., *et al.*, 2017. Mechanistic materials modeling for nuclear fuel performance. *Ann. Nucl. Energy* 105, 11.
- 351. IAEA, 2011. Fuel Modeling at extended burnup (FUMEX-II). Report of a Coordinated Research Project, IAEA-TECDOC-1687. Vienna.
- 352. Pizzocri, D., Bouloré, A., Stuckert, J., *et al.*, 2018. IAEA FUMAC benchmark on the Halden, Studsvik and QUENCH-L1 LOCA tests. In: *Proceedings of the Top Fuel 2018*, September 30-October 4, 2018. Prague, Czech Republic: ENS.